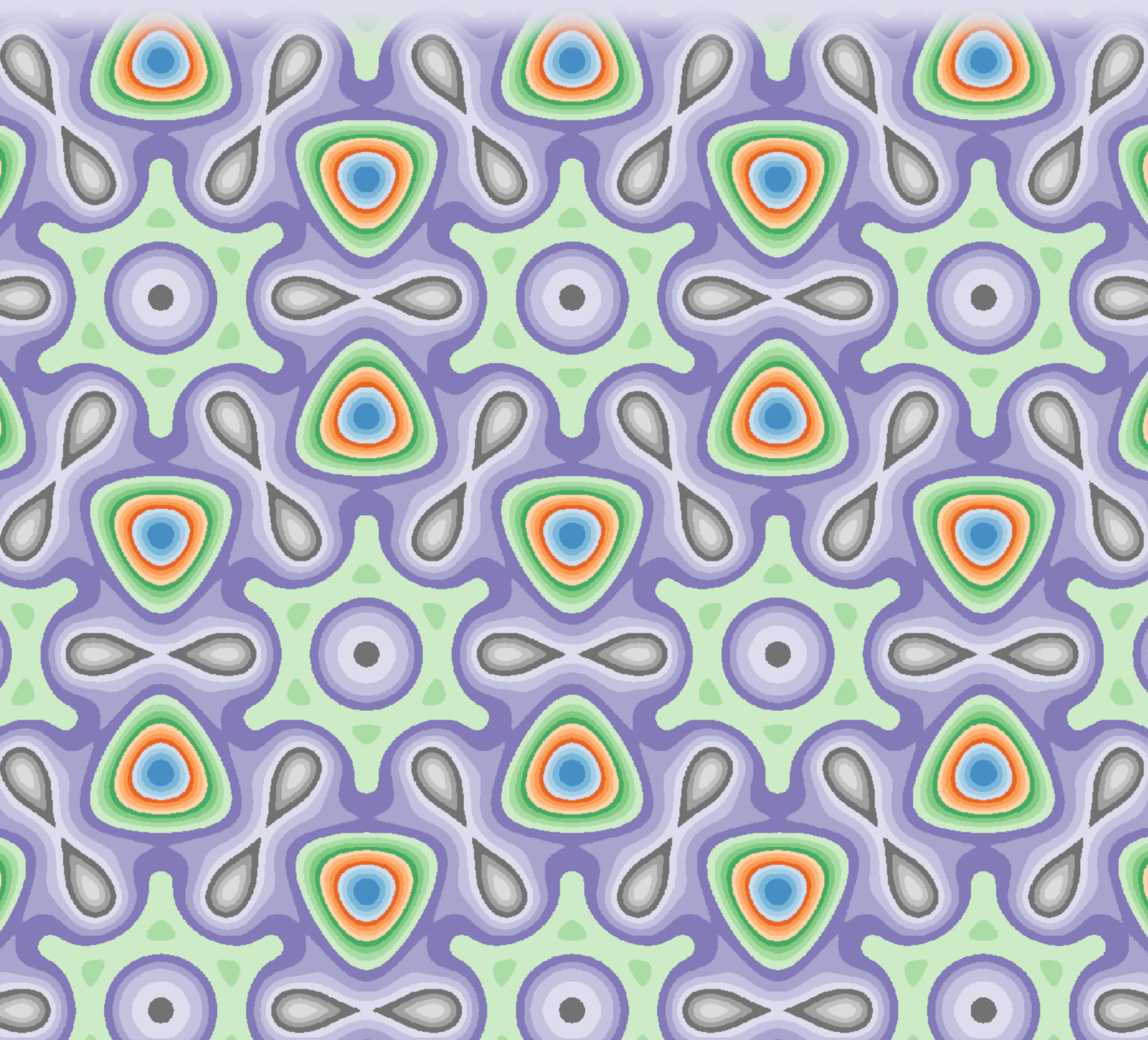


Modeling the electrically tunable optical properties of monolayer MoS₂

Mads-Peter Verner Christiansen
Jannick Kjær Jørgensen





AALBORG UNIVERSITY
Master's Thesis

**Master's Thesis at School of
Engineering and Science**
The Faculty of Engineering and Science
Department of Materials and Production
Skjernvej 4A
9220 Aalborg East

Title:

Modeling the electrically tunable
optical properties of monolayer MoS₂

Participants:

Jannick Kjær Jørgensen
Mads-Peter Verner Christiansen

Project period:

September 2017 - May 2018

Supervisor:

Thomas Garm Pedersen

Abstract:

The motivation of this thesis is the experimental realization of highly tunable optical properties of transition metal dichalcogenides as reported in recent literature. In order to understand the root cause of this phenomenon a quantum mechanical description is required. The tunability of the optical properties is controlled by excitons which require including the electron-hole interaction responsible for their existence. A framework based on ab-initio DFT wave functions and an analytical expression for the dielectric screening has been developed which predicts intrinsic properties in fair agreement with experiments. The inclusion of doping by electrostatic gating requires including the effect in the DFT calculation and two models of doping have been proposed and compared. G0W0 calculations have been performed to study the effect of doping on bandgap renormalization and it has been found that doping also significantly reduces the effective electron mass in the case of n-doping. Importantly the effect of doping must also be included in the dielectric screening which is done through an analytical model. The fully developed model qualitatively reproduces the tunability of the optical properties. Reflection spectroscopy measurements have been carried out on intrinsic MoS₂ showing the excitonic transitions. Gates have been deposited on the MoS₂ sample in order to electrically dope during reflectance measurements, however more work is required to obtain definitive results.

Pages: 78

Appendices: 4

Finalized: 01-06-2018

Preface

This master's thesis is written by Jannick Kjær Jørgensen and Mads-Peter Verner Christiansen as their final project for the nanomaterials and nanophysics program at Aalborg University in the period September 4th 2017 to June 1st 2018. Professor Thomas Garm Pedersen has been the supervisor for the project. The thesis is a continuation of a semester project the authors participated in on the electronic properties of MoS₂, and concerns itself with the optical properties. The inspiration for this choice stems from findings that the optical properties in MoS₂ can be dramatically altered by electrical gating.

Throughout the report, each chapter and section will have numbered titles and all figures, tables, and equations will be numbered. Vectors and matrices will be denoted in bold. Citations are given as [”number”], with ”number” being the position in the bibliography. If the citation is placed before the period it refers only to that sentence, whereas citations placed after the period refer to the entire paragraph. Figures with citations are adopted or adapted from literature, while figures with no citation are created by the authors.

We would like to thank Professor Thomas Garm Pedersen for his invaluable guidance throughout the project. The experimental work could not have been done without the help of research technician Peter Kjær Kristensen, laboratory technician Kim Houtved Jensen and workman Hans Nilsson. We would also like to thank assistant professor Thomas Olsen for his assistance with the GPAW code and IT administrator Mads Boye for his help with installing GPAW on the ABACUS supercomputer.

Jannick Kjær Jørgensen

Mads-Peter Verner Christiansen

Contents

1	Introduction	1
2	Independent Particle Optical Properties	5
2.1	Linear perturbation theory	6
2.2	Optical properties of 2D semiconductors	9
2.3	Numerical implementation	10
2.4	Basis set considerations	11
2.5	Optical properties of Graphene	11
2.6	Optical properties of MoS ₂	14
3	Doping Models	15
3.1	Electrostatic doping models	16
3.2	Doping in graphene	20
3.3	Doping in MoS ₂	23
4	Excitons	25
4.1	The Bethe-Salpeter equation	25
4.2	Quasi-particle energy	27
4.3	Screening in 2D	28
4.4	Slow-rapid approximation	30
4.5	Wannier approximation	31
4.6	Two-band approximation	31
4.7	Optical properties of excitons	33
4.8	Numerical implementation	35
4.9	Substrate effects	37
4.10	Spin-orbit interaction	39
4.11	Coulomb and exchange integrals	40
5	Doping and Excitons	43
5.1	Screening by additional charge carriers	43
5.2	Quasiparticle energies with doping	45
5.3	Doped MoS ₂	49
5.4	Doped hBN encapsulated MoS ₂	50
5.5	Dynamic screening	52
6	Experimental Results	55
6.1	Characterization of MoS ₂	55
6.2	Fabrication of capacitor	57

6.3 Reflection experiment	59
7 Conclusion	63
Appendix A Computational Details for Ab-initio Calculations	65
Appendix B Projector Augmented Wave method	67
Appendix C Transfer Matrix Method & Constrained Kramers Kronig Analysis	69
Appendix D Implementation	73
Bibliography	75

Chapter 1

Introduction

Two dimensional materials have received significant attention since the experimental realization of a single-sheet of carbon atoms in a hexagonal lattice, known as graphene in 2004 [1, 2]. Graphene has since then been the subject of many papers, both studying its unique properties theoretically and attempting to take advantages of these experimentally and this extraordinary arrangement of carbon atoms is still being exploited in novel ways today. The Dirac-cone electronic structure of graphene leads to many fascinating properties, such as extreme electrical conductivity. Unfortunately, this electronic structure leaves no room for an electronic or optical bandgap, and puts pristine graphene in the 'semi-metal' category of materials. The lack of a bandgap limits the usefulness of graphene in the electronics industry, especially in semiconductor and optoelectronic devices. [3–5]

However, with graphene as inspiration another group of materials have recently hit the scientific spotlight, namely the transition metal dichalcogenides (TMDs). The TMDs, as the name suggests, consist of a transition metal atom and two chalcogen atoms per unit cell, considering the many transition metals the amount of combinations enables the formation of many TMDs. Fig. 1.1 highlights the elements involved in layered TMD materials.

Figure 1.1: Periodic table with transition metals and chalcogens highlighted. The fully colored transition metal create layered structures with all the chalcogen atoms that are fully colored, while the framed ones only do so with some of the chalcogens.

One of the most popular TMDs is MoS_2 , which has a similar lattice to that of graphene with half the carbon atoms replaced by molybdenum and the other half by two sulfur atoms, one stacked on the other, as shown in Fig. 1.2(a). The side view reveals that MoS_2 is three atoms thick, with a layer of molybdenum

sandwiched between layers of sulfur. Throughout this thesis the name MoS_2 will only be used to describe the monolayer structure. As is typical for calculations in solid state physics, most calculations are most easily performed in reciprocal space, thus the Brillouin zone (BZ) is an important quantity that will be utilized extensively throughout this thesis. The Brillouin zone of MoS_2 with the lattice vector definitions from Fig. 1.2(a) is shown in Fig. 1.2(b) where the irreducible BZ (IBZ) is marked in red. The IBZ contains all necessary information of BZ due to symmetry and BZ integrals can be performed over only the IBZ [6].

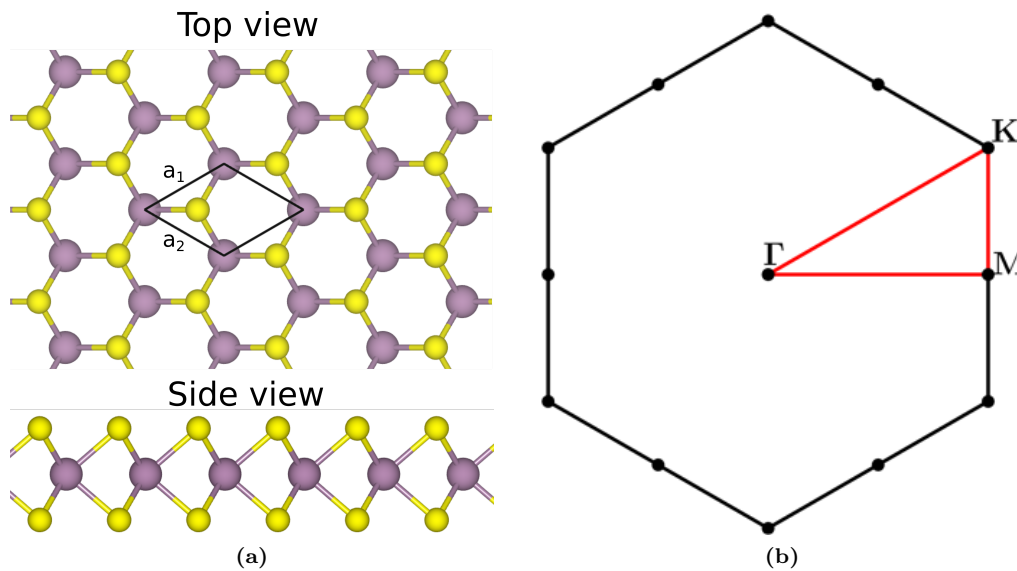


Figure 1.2: Crystal structure of MoS_2 , (a) top view and side view of MoS_2 . (b) First Brillouin zone, indicating the the irreducible Brillouin zone in red and the relevant special points.

MoS_2 among with many of the other TMDs is a direct band gap semiconductor with a significant optical band gap of 1.88 eV, allowing the fabrication of many traditional semiconductor devices such as field-effect transistors as well as untraditional devices such as re-configurable devices [7–9]. Recently it was found experimentally that the optical properties, i.e. the complex refractive index, of monolayer TMDs can be tuned electrically by an applied voltage [10]. This discovery has already been utilized to create high reflectance tunable mirrors for optoelectronic devices [11, 12].

An optical process in a semiconductor revolves around an electron absorbing a photon and jumping to an excited state with a higher energy. In an independent-particle image this transition can for example be from a valence state to a conduction state and can be calculated from an appropriate set of orbitals, e.g. from Kohn-Sham orbitals obtained from DFT calculations. For some materials this can lead to results that are in decent agreement with experiments [13]. However, such a view is generally not sufficient as such a process fundamentally moves the system from the ground state to an excited state, making the ground state properties insufficient. A common problem for DFT calculations is that wrong fundamental band gaps are obtained related to the way exchange and correlation are treated [14]. Another approach for calculating the fundamental band gap is a many-body treatment such as the GW-approximation, which has shown to correctly predict the fundamental band gap SOURCE. However, for optical processes the interaction between the excited electron and hole left behind must also be included. Because of this interaction the photon energy required for absorption can be significantly lower than the fundamental band gap, thus correctly predicting the optical band gap observed in spectroscopic measurements. An illustration of the three levels of theory is shown in Fig. 1.3. [15]

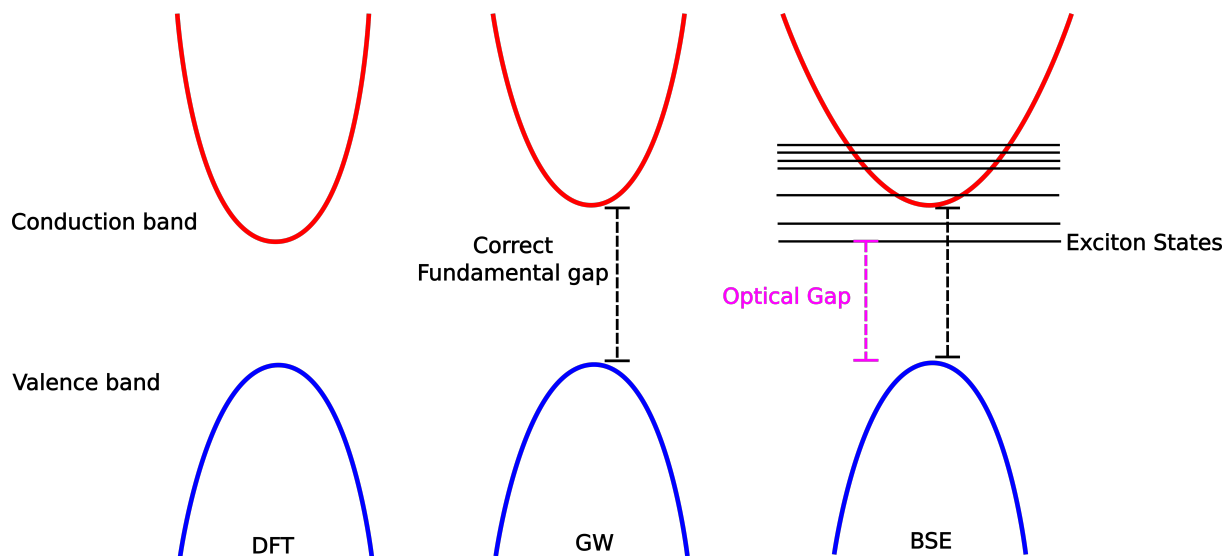


Figure 1.3: Illustration of the levels of theory relevant for the absorption of a photon. The leftmost pair of bands represent a DFT calculation, where the fundamental band gap is wrong. The middle pair of bands represent the GW approximation, which corrects the fundamental band gap, but does not include electron-hole interactions. The electron-hole interaction creates states below the fundamental band gap as shown in the rightmost illustration, which are called excitons that can be calculated using the Bethe-Salpeter equation.

This bound combination of an electron and a hole is what is called an exciton, and the exciton binding energy refers to the difference compared to the fundamental band gap. For two-dimensional materials, such as MoS_2 , this effect is very important as the reduced dimensionality does not allow large separations between the electron and hole, which leads to much higher binding energies in these materials compared to bulk semiconductors. Furthermore, the interaction between the electron and the hole is not the usual Coulomb interaction, but rather a screened interaction taking into account the presence of other charge carriers, but this screening is also reduced in lower dimensions. As an example, the exciton binding energy of silicon has been measured to be 15 meV compared to reports of binding energies of several hundred meV for two dimensional materials [16, 17]. As mentioned earlier the optical properties of monolayer TMDs can be tuned by electrical gating, effectively changing the carrier density inside the TMD monolayer, which in turn influences the optical properties. This tunability is possible because the optical properties at the relevant frequencies are completely decided by the excitons, which are very sensitive to changes in the dielectric environment as caused by adding additional charge carriers by doping.

The goals of this thesis are to:

- Develop tools to calculate the independent particle optical properties of monolayers.
- Develop tools to calculate many-body optical properties of monolayers.
- Compare methods of introducing doping in DFT calculations.
- Study the effect of doping on the optical properties in both theoretical frameworks.
- Experimentally measure the optical properties of MoS_2 with and without doping.

In Chap. 2 a theory is derived that enables the calculation of independent particle optical properties and results of calculations for MoS_2 and graphene are presented. As graphene has received so much attention in the scientific community the optical properties of graphene are well-known, making graphene a useful

benchmark of the methodology. In Chap. 3 the problems of including doping in ab-initio calculations are discussed and two possible models are compared and afterwards optical properties of doped MoS₂ and graphene are presented. Inclusion of the interaction between an excited electron and the hole it leaves behind requires a more complicated theory, which is presented in Chap. 4, where both theory and numerical problems are discussed, along with the results of the theory applied to MoS₂. Chap. 5 introduces the final ingredients required to extend the theory to include doping and the result of these calculations are presented. The experimental methodology and results are presented and discussed in Chap. 6. Finally Chap. 7 concludes this thesis.

The majority of the theoretical results are based on DFT calculations done in the GPAW code [18, 19]. The computational details for all calculations and the figures they are relevant for are given in Appendix A.

Chapter 2

Independent Particle Optical Properties

Optical properties are used to describe the interaction between electromagnetic waves and matter. Starting from Maxwell's equations, assuming a non-magnetic source-free isotropic material they become

$$\begin{aligned}\nabla \times \mathbf{E}(\mathbf{r}, t) &= -\mu_0 \frac{d\mathbf{H}(\mathbf{r}, t)}{dt} \\ \nabla \times \mathbf{H}(\mathbf{r}, t) &= \frac{d\mathbf{D}(\mathbf{r}, t)}{dt} + \mathbf{j}(\mathbf{r}, t) \\ \nabla \cdot \mathbf{D}(\mathbf{r}, t) &= 0 \\ \nabla \cdot \mathbf{B}(\mathbf{r}, t) &= 0,\end{aligned}\tag{2.1}$$

with \mathbf{D} being the electric displacement, \mathbf{j} being only the induced current density as no source current is present, \mathbf{B} being the magnetic induction, and μ_0 being the vacuum permeability. The electric displacement is defined in terms of the electric field and the polarization $\mathbf{P}(\mathbf{r}, t)$ as

$$\mathbf{D}(\mathbf{r}, t) = \varepsilon_0 \mathbf{E}(\mathbf{r}, t) + \mathbf{P}(\mathbf{r}, t),\tag{2.2}$$

with ε_0 being the vacuum permittivity. In a dispersive media the polarization can be written as a convolution between the electric field and the time-dependent susceptibility $\chi(\mathbf{r}, t)$ as

$$\mathbf{P}(\mathbf{r}, t) = \varepsilon_0 \int_{-\infty}^t \chi(\mathbf{r}, t - t') \mathbf{E}(\mathbf{r}, t') dt',\tag{2.3}$$

where causality dictates the upper limit of the integral. This convolution makes the time-domain both-ersome, but luckily Maxwell's equations can be written in the frequency domain through the Fourier transform. The Fourier transform of the polarization means the convolution becomes a product as

$$\mathbf{P}(\mathbf{r}, \omega) = \varepsilon_0 \chi(\mathbf{r}, \omega) \mathbf{E}(\mathbf{r}, \omega).\tag{2.4}$$

The electric displacement in the frequency domain then becomes

$$\mathbf{D}(\mathbf{r}, \omega) = \varepsilon_0 \mathbf{E}(\mathbf{r}, \omega) + \varepsilon_0 \chi(\mathbf{r}, \omega) \mathbf{E}(\mathbf{r}, \omega) = \varepsilon_0 (1 + \chi(\mathbf{r}, \omega)) \mathbf{E}(\mathbf{r}, \omega) = \varepsilon_0 \varepsilon_r(\mathbf{r}, \omega) \mathbf{E}(\mathbf{r}, \omega),\tag{2.5}$$

with ε_r being the relative dielectric permittivity. The induced current density in frequency domain can be written as

$$\mathbf{j}(\mathbf{r}, \omega) = \sigma(\mathbf{r}, \omega) \mathbf{E}(\mathbf{r}, \omega),\tag{2.6}$$

with $\sigma(\mathbf{r}, \omega)$ being the conductivity. Maxwell's equations for the curl of the electric field and the curl of the magnetic field in the frequency domain become

$$\begin{aligned}\nabla \times \mathbf{E}(\mathbf{r}, \omega) &= i\omega\mu_0 \mathbf{H}(\mathbf{r}, \omega) \\ \nabla \times \mathbf{H}(\mathbf{r}, \omega) &= \sigma(\mathbf{r}, \omega) \mathbf{E}(\mathbf{r}, \omega) - i\omega\varepsilon_0 \varepsilon_r(\mathbf{r}, \omega) \mathbf{E}(\mathbf{r}, \omega).\end{aligned}\tag{2.7}$$

Taking the curl of the curl of the electric field and remembering that the divergence of the electric displacement is 0 yields

$$\nabla^2 \mathbf{E}(\mathbf{r}, \omega) = i\omega\mu_0\sigma(\mathbf{r}, \omega)\mathbf{E}(\mathbf{r}, \omega) + \omega^2\mu_0\varepsilon_0\varepsilon_r(\mathbf{r}, \omega)\mathbf{E}(\mathbf{r}, \omega). \quad (2.8)$$

As $\mu_0\varepsilon_0 = \frac{1}{c^2}$ The equation can be compacted to

$$\left[\nabla^2 - k_0^2 \left(\varepsilon_r(\mathbf{r}, \omega) + \frac{i\sigma(\mathbf{r}, \omega)}{\varepsilon_0\omega} \right) \right] \mathbf{E}(\mathbf{r}, \omega) = 0, \quad (2.9)$$

with $k_0^2 = \frac{\omega^2}{c^2}$ being the wave vector in free-space. Eq. (2.9) is known as the wave equation in matter, which makes it clear that the interaction between the electromagnetic wave and matter, is described by the relative dielectric permittivity $\varepsilon_r(\mathbf{r}, \omega)$ and the conductivity $\sigma(\mathbf{r}, \omega)$. Instead of dealing with both of these quantities it is convenient to define a complex dielectric permittivity $\tilde{\varepsilon}$

$$\tilde{\varepsilon}(\omega) = \varepsilon_1 + i\varepsilon_2 = \varepsilon_r(\mathbf{r}, \omega) + \frac{i\sigma(\mathbf{r}, \omega)}{\varepsilon_0\omega}. \quad (2.10)$$

Had the material been anisotropic, the complex dielectric permittivity would have had to be replaced with a tensor. This complex permittivity can also be related to other meaningful complex optical properties through the following equations

$$\begin{aligned} \tilde{\varepsilon}(\omega) &= \tilde{n}^2(\omega) = [n(\omega) + i\kappa(\omega)]^2 \\ \tilde{\varepsilon}(\omega) &= 1 + \tilde{\chi}(\omega) \\ \tilde{\varepsilon}(\omega) &= 1 + \frac{i\tilde{\sigma}(\omega)}{\varepsilon_0\omega}, \end{aligned} \quad (2.11)$$

where $\tilde{n}(\omega)$ is the complex refractive index. Thus, by knowing one of these properties all of the other properties can be found, and the interaction can be understood. It is seen that the imaginary part of the complex dielectric permittivity governs absorption, which corresponds to the real part of the optical conductivity. Throughout the remaining chapters the complex optical properties will be denoted without tilde. [20, 21]

2.1 Linear perturbation theory

The optical properties of a system describes the response of a system to external electromagnetic perturbation, such as light. If the perturbation is considered to be small, the response of the system can be approximated to be only linear and a suitable framework can be derived, which is done in this section following the formalism of [22]. The ground state wave function can be constructed as a Slater determinant, where the orbitals are given by the time-independent Schrödinger equation

$$\hat{H}_0\varphi_n^0 = E_n^0\varphi_n^0, \quad (2.12)$$

with \hat{H}_0 denoting the unperturbed Hamiltonian, E_n^0 as the n 'th eigenvalue, and φ_n^0 as the n 'th eigenfunction of the ground state, where only eigenfunctions with eigenvalues below the Fermi level are used to construct the ground state Slater determinant. Perturbing this system creates an excited state, but instead of creating a completely new Hamiltonian, perturbation theory works by approximating the solutions of the excited system by using a Hamiltonian which is the sum of the ground state Hamiltonian and the interaction Hamiltonian \hat{H}' , describing the effects of the perturbation

$$\hat{H} = \hat{H}_0 + \hat{H}'. \quad (2.13)$$

However, the perturbation of the system is not independent of time. Assuming the response is characterized by a single frequency ω , and only including the first-order interaction Hamiltonian, the time-dependent Schrödinger equation becomes

$$i\hbar \frac{\partial \psi}{\partial t} = \left[\hat{H}_0 + \frac{1}{2} \hat{H}_1 e^{-i\omega t} + \frac{1}{2} \hat{H}_1^\dagger e^{i\omega t} \right] \psi. \quad (2.14)$$

The time-dependent wave function is given by $\phi_n e^{-iE_n t/\hbar}$, meaning the perturbed wave function ψ can be written as

$$\psi = \sum_n a_n \varphi_n e^{-iE_n t/\hbar}, \quad (2.15)$$

with a_n being a time-dependent coefficient. Inserting into the time-dependent Schrödinger equation

$$i\hbar \frac{\partial}{\partial t} \sum_n a_n \varphi_n e^{-iE_n t/\hbar} = \left[\hat{H}_0 + \frac{1}{2} \hat{H}_1 e^{-i\omega t} + \frac{1}{2} \hat{H}_1^\dagger e^{i\omega t} \right] \sum_n a_n \varphi_n e^{-iE_n t/\hbar}, \quad (2.16)$$

which can be rearranged to

$$\sum_n \left(a_n E_n \varphi_n + i\hbar \frac{\partial a_n}{\partial t} \varphi_n \right) e^{-iE_n t/\hbar} = \sum_n a_n \left[\hat{H}_0 \varphi_n + \frac{1}{2} \hat{H}_1 \varphi_n e^{-i\omega t} + \frac{1}{2} \hat{H}_1^\dagger \varphi_n e^{i\omega t} \right] e^{-iE_n t/\hbar}. \quad (2.17)$$

and utilizing Eq. (2.12) it is seen that the first term on the left-hand side cancels out the first term on the right-hand side of the equation, thus

$$\sum_n i\hbar \frac{\partial a_n}{\partial t} \varphi_n e^{-iE_n t/\hbar} = \sum_n \frac{a_n}{2} \left[\hat{H}_1 \varphi_n e^{-i\omega t} + \hat{H}_1^\dagger \varphi_n e^{i\omega t} \right] e^{-iE_n t/\hbar}. \quad (2.18)$$

Multiplying from the right with $\langle \varphi_m |$ and integrating, while remembering that the eigenstates are orthonormal so that $\langle \varphi_n | \varphi_m \rangle = \delta_{nm}$

$$\sum_n i\hbar \frac{\partial a_n}{\partial t} \delta_{nm} e^{-iE_n t/\hbar} = \frac{1}{2} \sum_n a_n \left[\langle \varphi_m | \hat{H}_1 | \varphi_n \rangle e^{-i\omega t} + \langle \varphi_m | \hat{H}_1^\dagger | \varphi_n \rangle e^{i\omega t} \right] e^{-iE_n t/\hbar}. \quad (2.19)$$

As the sum on the left-hand side only has a non-zero term when $n = m$ it can be removed, leaving

$$\frac{\partial a_m}{\partial t} = -\frac{i}{2\hbar} \sum_n a_n \left[\langle \varphi_m | \hat{H}_1 | \varphi_n \rangle e^{-i\omega t} + \langle \varphi_m | \hat{H}_1^\dagger | \varphi_n \rangle e^{i\omega t} \right] e^{iE_{mn} t/\hbar}. \quad (2.20)$$

with $E_{mn} = E_m - E_n$. Assuming the interaction Hamiltonian is linearly proportional to the field strength, the coefficients a_n will also depend on field strength. A Taylor expansion can be made with regard to the field strength as

$$a_n = a_n^{(0)} + a_n^{(1)} + a_n^{(2)} + \dots, \quad (2.21)$$

with the superscript indicating the order of the perturbation. Inserting the Taylor expansion into Eq. (2.20) and utilizing the theorem on equality of polynomials

$$\text{If for all } x, \sum_p b_p x^p = \sum_p c_p x^p \text{ then } b_p = c_p, \quad (2.22)$$

one can write Eq. (2.20) as

$$\frac{\partial a_m^{(p)}}{\partial t} = -\frac{i}{2\hbar} \sum_n a_n^{(p-1)} \left[\langle \varphi_m | \hat{H}_1 | \varphi_n \rangle e^{-i\omega t} + \langle \varphi_m | \hat{H}_1^\dagger | \varphi_n \rangle e^{i\omega t} \right] e^{iE_{mn} t/\hbar}, \quad (2.23)$$

because the integrals $\langle \varphi_m | \hat{H}_1 | \varphi_n \rangle$ and $\langle \varphi_m | \hat{H}_1^\dagger | \varphi_n \rangle$ already contain one power of the perturbation field strength. It is thus clear that the coefficients of the total wave function can be found by an iterative process, starting with $p = 0$. The zero'th order coefficient should not be time-dependent and so $\frac{\partial a_n^{(0)}}{\partial t} = 0$,

meaning $a_m^{(0)}$ is just some constant. The next coefficient is found by setting $p = 1$, and so on. However, for linear response, only $p = 1$ is used. For $p = 1$ Eq. (2.23) becomes

$$\frac{\partial a_m^{(1)}}{\partial t} = -\frac{i}{2\hbar} \sum_n a_n^{(0)} \left[\langle \varphi_m | \hat{H}_1 | \varphi_n \rangle e^{-i\omega t} + \langle \varphi_m | \hat{H}_1^\dagger | \varphi_n \rangle e^{i\omega t} \right] e^{iE_{mn}t/\hbar}. \quad (2.24)$$

By integrating over time to the time t on both sides the equation becomes

$$a_m^{(1)} = -\frac{i}{2\hbar} \sum_n a_n^{(0)} \int \left[\langle \varphi_m | \hat{H}_1 | \varphi_n \rangle e^{-i\omega t} + \langle \varphi_m | \hat{H}_1^\dagger | \varphi_n \rangle e^{i\omega t} \right] e^{iE_{mn}t/\hbar} dt. \quad (2.25)$$

Assuming the perturbation was not present in the infinite past, the lower limit of the integral can be ignored, and $a_m^{(1)}$ is found to be

$$a_m^{(1)} = -\frac{1}{2} \sum_n a_n^{(0)} \left[\langle \varphi_m | \hat{H}_1 | \varphi_n \rangle \frac{e^{-i\omega t}}{E_{mn} - \hbar\omega} + \langle \varphi_m | \hat{H}_1^\dagger | \varphi_n \rangle \frac{e^{i\omega t}}{E_{mn} + \hbar\omega} \right] e^{iE_{mn}t/\hbar}. \quad (2.26)$$

It is clear that the coefficient is divergent at $E_{mn} = \hbar\omega$, however, by implementing losses via the damping $\hbar\Gamma$ in the system, the equation can be written as

$$a_m^{(1)} = -\frac{1}{2} \sum_n a_n^{(0)} \left[\langle \varphi_m | \hat{H}_1 | \varphi_n \rangle \frac{e^{-i\omega t}}{E_{mn} - \hbar\omega - i\hbar\Gamma} + \langle \varphi_m | \hat{H}_1^\dagger | \varphi_n \rangle \frac{e^{i\omega t}}{E_{mn} + \hbar\omega - i\hbar\Gamma} \right] e^{iE_{mn}t/\hbar}. \quad (2.27)$$

As the coefficients are now known any first order response can now be found. Let \hat{X} be the operator of some observable, such that $\langle X \rangle = \langle \psi | \hat{X} | \psi \rangle$. Then by equations (2.15) and (2.21), the first order response is simply

$$\langle \psi | \hat{X} | \psi \rangle \approx \sum_{m,n} \left[a_n^{*(0)} a_m^{(0)} + a_n^{*(0)} a_m^{(1)} + a_n^{*(1)} a_m^{(0)} \right] \langle \varphi_n | \hat{X} | \varphi_m \rangle e^{iE_{nm}t/\hbar}. \quad (2.28)$$

$a_n^{*(0)} a_n^{(0)} = |a_n^{(0)}|^2$ is interpreted as the probability of the unperturbed system to be in the state φ_n , thus if the system is further assumed to be in thermal equilibrium the probability is given by (for fermions) the Fermi-Dirac distribution $f(E_n)$. Further it is postulated that

$$a_n^{*(0)} a_m^{(0)} = f(E_n) \delta_{nm}. \quad (2.29)$$

Inserting this postulate into Eq. (2.28) and using Eq. (2.27)

$$\begin{aligned} \langle \psi | \hat{X} | \psi \rangle &\approx \sum_n f(E_n) \langle \varphi_n | \hat{X} | \varphi_n \rangle \\ &- \frac{1}{2} \sum_{m,n} f(E_n) \langle \varphi_n | \hat{X} | \varphi_m \rangle \left[\frac{\langle \varphi_m | \hat{H}_1 | \varphi_n \rangle e^{-i\omega t}}{E_{mn} - \hbar\omega - i\hbar\Gamma} + \frac{\langle \varphi_m | \hat{H}_1^\dagger | \varphi_n \rangle e^{i\omega t}}{E_{mn} + \hbar\omega - i\hbar\Gamma} \right] \\ &- \frac{1}{2} \sum_{m,n} f(E_m) \langle \varphi_n | \hat{X} | \varphi_m \rangle \left[\frac{\langle \varphi_m | \hat{H}_1^\dagger | \varphi_n \rangle e^{i\omega t}}{E_{nm} - \hbar\omega + i\hbar\Gamma} + \frac{\langle \varphi_m | \hat{H}_1 | \varphi_n \rangle e^{-i\omega t}}{E_{nm} + \hbar\omega + i\hbar\Gamma} \right], \end{aligned}$$

it is seen that the first term is not dependent on the frequency of the perturbation, and that the result can be rearranged/grouped by frequency dependency as

$$\langle \psi | \hat{X} | \psi \rangle = \sum_n f(E_n) \langle \varphi_n | \hat{X} | \varphi_n \rangle + \frac{1}{2} X(\omega) e^{-i\omega t} + \frac{1}{2} X^*(\omega) e^{i\omega t}, \quad (2.30)$$

with

$$X(\omega) = -\sum_{m,n} f_{nm} \frac{\langle \varphi_m | \hat{H}_1 | \varphi_n \rangle \langle \varphi_n | \hat{X} | \varphi_m \rangle}{E_{mn} - \hbar\omega - i\hbar\Gamma}, \quad (2.31)$$

where $f_{nm} \equiv f(E_n) - f(E_m)$. This term is thus the first order time-dependent induced response due to some perturbation. It shows that by knowing the interaction Hamiltonian and the induced response operator, one can find the induced response.

2.2 Optical properties of 2D semiconductors

To investigate the optical properties of a 2D semiconductor, it is assumed that the semiconductor is subjected to an electric field pointing in the plane of the semiconductor, e.g. along the x-axis such that $\mathbf{E} = E\hat{\mathbf{x}}$, with a frequency ω . This electric field will interact with the electric dipole moment $-\mathbf{er}$ such that the interaction Hamiltonian becomes $\hat{H}_1 = e\mathbf{E}\mathbf{r} = eEx$ [23]. The observable is the dipole moment density, also known as the polarization, $\hat{P}(\omega) = \frac{-e\mathbf{x}}{\Omega}$, with Ω being the volume of the material. Using the result from linear response theory it is seen that the polarization is given by

$$P(\omega) = -\frac{1}{\Omega} \sum_{m,n} f_{nm} \frac{\langle \varphi_m | eEx | \varphi_n \rangle \langle \varphi_n | -ex | \varphi_m \rangle}{E_{mn} - \hbar\omega - i\hbar\Gamma} = \frac{e^2 E}{\Omega} \sum_{m,n} f_{nm} \frac{|\langle \varphi_m | x | \varphi_n \rangle|^2}{E_{mn} - \hbar\omega - i\hbar\Gamma}, \quad (2.32)$$

with the last part being found by utilizing that $\langle \varphi_n | x | \varphi_m \rangle = \langle \varphi_m | x | \varphi_n \rangle^*$. The polarization can also be written as $P(\omega) = \varepsilon_0 \chi(\omega) E$, with $\chi(\omega)$ being the susceptibility. The susceptibility can thus be found by

$$\chi(\omega) = \frac{e^2}{\varepsilon_0 \Omega} \sum_{m,n} f_{nm} \frac{|\langle \varphi_m | x | \varphi_n \rangle|^2}{E_{mn} - \hbar\omega - i\hbar\Gamma}. \quad (2.33)$$

As the sum in m and n is over the same set of bands, the equation can be averaged and m and n can be interchanged. Further using $f_{mn} = -f_{nm}$ and $E_{nm} = -E_{mn}$ the equation becomes

$$\chi(\omega) = \frac{e^2}{\varepsilon_0 \Omega} \sum_{m,n} f_{nm} \frac{E_{mn} |\langle \varphi_m | x | \varphi_n \rangle|^2}{E_{mn}^2 - \hbar^2(\omega + i\Gamma)^2}. \quad (2.34)$$

Next the commutator trick $\langle \varphi_m | [\hat{H}_0, \hat{O}] | \varphi_n \rangle = E_{mn} \langle \varphi_m | \hat{O} | \varphi_n \rangle$, where \hat{O} is some operator, and that the commutator of \hat{H}_0 and x is $[\hat{H}_0, x] \varphi = \frac{-i\hbar}{m} \hat{p}_x \varphi$ is used as $\langle \varphi_m | x | \varphi_n \rangle = \frac{-i\hbar}{m E_{mn}} \langle \varphi_m | \hat{p}_x | \varphi_n \rangle$ assuming that $n \neq m$, which are known as momentum matrix elements. Thus

$$\chi(\omega) = \frac{e^2 \hbar^2}{m^2 \varepsilon_0 \Omega} \sum_{m,n} f_{nm} \frac{|\langle \varphi_m | \hat{p}_x | \varphi_n \rangle|^2}{E_{mn} [E_{mn}^2 - \hbar^2(\omega + i\Gamma)^2]}. \quad (2.35)$$

Eventually an expression that can be evaluated over the IBZ is wanted. In order to do so the matrix elements need to be symmetrized to account for the arbitrary choice of IBZ, so that

$$|\langle \varphi_m | \hat{p}_{xy} | \varphi_n \rangle|^2 = \frac{|\langle \varphi_m | \hat{p}_x | \varphi_n \rangle|^2 + |\langle \varphi_m | \hat{p}_y | \varphi_n \rangle|^2}{2}. \quad (2.36)$$

The n and m indices are composite over band, k-point, and spin, meaning $m \rightarrow m\mathbf{k}\sigma$. Assuming no spin-orbit coupling, spin degeneracy yields a factor of 2. Furthermore, the sum over \mathbf{k} can be turned into a \mathbf{k} -integral, which will be over the entire Brillouin zone as

$$\frac{1}{\Omega} \sum_{\mathbf{k}} = \frac{A}{\Omega(2\pi)^2} \int d^2k, \quad (2.37)$$

with A and Ω being the area and volume of the unit cell, respectively. The susceptibility is

$$\chi(\omega) = \frac{2e^2 \hbar^2}{\varepsilon_0 m^2 (2\pi)^2 d} \sum_{m,n} \int f_{nm} \frac{|\langle \varphi_{m\mathbf{k}} | \hat{p}_{xy} | \varphi_{n\mathbf{k}} \rangle|^2}{E_{mn} [E_{mn}^2 - \hbar^2(\omega + i\Gamma)^2]} d^2k, \quad (2.38)$$

with d being the thickness of the 2D structure. As the double sum runs over all bands there will be two types of terms, namely interband terms where $n \neq m$ and intraband terms where $n = m$. Thus the total susceptibility will be

$$\chi(\omega) = \chi_{inter}(\omega) + \chi_{intra}(\omega) = \chi_E(\omega) + \chi_I(\omega). \quad (2.39)$$

In the interband contribution the photon momentum \mathbf{q} can safely be neglected, however the same is not true for the intraband contribution. For the interband case there will be terms where $m > n$ and $n > m$, and as the sums run over all bands the second type of terms can be interchanged, giving

$$\chi_E(\omega) = \frac{4e^2\hbar^2}{\varepsilon_0 m^2 (2\pi)^2 d} \sum_{m>n} \int f_{nm} \frac{|\langle \varphi_{m\mathbf{k}} | \hat{p}_{xy} | \varphi_{n\mathbf{k}} \rangle|^2}{E_{mn} [E_{mn}^2 - \hbar^2(\omega + i\Gamma)^2]} d^2k. \quad (2.40)$$

For the intraband terms the photon momentum can not be ignored, meaning the 2D intraband susceptibility should be written as

$$\chi_I(\omega) = \frac{2e^2\hbar^2}{\varepsilon_0 m^2 (2\pi)^2 d} \sum_n \int [f(E_{n\mathbf{k}}) - f(E_{n\mathbf{k}+\mathbf{q}})] \frac{|\langle \varphi_{n\mathbf{k}+\mathbf{q}} | \hat{p}_{xy} | \varphi_{n\mathbf{k}} \rangle|^2}{\Delta E [\Delta E^2 - \hbar^2(\omega + i\Gamma)^2]} d^2k, \quad (2.41)$$

with $\Delta E = E_{n\mathbf{k}+\mathbf{q}} - E_{n\mathbf{k}}$. However, in the limit of $\mathbf{q} \rightarrow 0$, the first order Taylor expansion of the Fermi-distribution gives $f(E_{n\mathbf{k}+\mathbf{q}}) \approx f(E_{n\mathbf{k}}) + f'(E_{n\mathbf{k}})\Delta E$ and the 2D susceptibility is

$$\chi_I(\omega) = \frac{2e^2\hbar^2}{\varepsilon_0 m^2 (2\pi)^2 d} \sum_n \int f'(E_{n\mathbf{k}}) \frac{|\langle \varphi_{n\mathbf{k}} | \hat{p}_{xy} | \varphi_{n\mathbf{k}} \rangle|^2}{\hbar^2(\omega + i\Gamma)^2} d^2k, \quad (2.42)$$

or rewritten as

$$\chi_I(\omega) = -\frac{\omega_p^2}{\omega(\omega + i\Gamma)d}, \quad (2.43)$$

where ω_p is the plasma frequency and given by

$$\omega_p^2 = -\frac{2e^2}{\varepsilon_0 m^2 (2\pi)^2} \sum_n \int f'(E_{n\mathbf{k}}) |\langle \varphi_{n\mathbf{k}} | \hat{p}_{xy} | \varphi_{n\mathbf{k}} \rangle|^2 d^2k. \quad (2.44)$$

2.3 Numerical implementation

As the eigenfunctions and eigenvalues of a DFT calculation are discretized in reciprocal space the \mathbf{k} -integral is handled numerically. Utilizing symmetry of the Brillouin zone, the integral only needs to be performed over an irreducible Brillouin zone. The 2D interband $\chi_{E_{2D}}(\omega) = \chi(\omega) \cdot d$ susceptibility becomes

$$\chi_{E_{2D}}(\omega) = \frac{4e^2\hbar^2}{\varepsilon_0 m^2 (2\pi)^2} \sum_{m>n} \sum_{\mathbf{k}}^{IBZ} w_{\mathbf{k}} f_{nm} \frac{|\langle \varphi_{m\mathbf{k}} | \hat{p}_{xy} | \varphi_{n\mathbf{k}} \rangle|^2}{E_{mn} [E_{mn}^2 - \hbar^2(\omega + i\Gamma)^2]} \Delta k_x \Delta k_y. \quad (2.45)$$

With weights $w_{\mathbf{k}}$ according to symmetry and $\Delta k_x, \Delta k_y$, being the spacing in \mathbf{k} -space. However, point-sampling of the \mathbf{k} -integral may take a large number of \mathbf{k} -points to converge, with large computational costs. Another way to handle the \mathbf{k} -integral is through the improved triangle method, which evaluates an integral over the IBZ on the form

$$S(\omega) = \int F(\mathbf{k}) \delta(E_{mn} - \hbar\omega) d^2k, \quad (2.46)$$

where the \mathbf{k} -grid is triangulated and both E_{mn} and $F(\mathbf{k})$ are assumed to be linear within each triangle. This allows for the resonant integral to be evaluated analytically over a line in each triangle, greatly improving convergence in regards to the \mathbf{k} -point sampling. [24, 25]

In order to use this integration scheme the expressions for the interband and intraband contributions need to be modified. Starting from equation (2.40), it is seen that in the limit of vanishing dampening the imaginary part of the susceptibility becomes

$$\begin{aligned} \text{Im}\{\chi_{E_{2D}}(\omega)\} &= \frac{4e^2\hbar^2}{\varepsilon_0 m^2 (2\pi)^2} \sum_{m>n} \int \frac{f_{nm} |\langle \varphi_{m\mathbf{k}} | \hat{p}_{xy} | \varphi_{n\mathbf{k}} \rangle|^2}{E_{mn}} \text{Im} \left\{ \lim_{\Gamma \rightarrow 0} \frac{1}{[E_{mn}^2 - \hbar^2(\omega + i\Gamma)^2]} \right\} d^2k \\ &= \frac{4e^2\hbar^2}{\varepsilon_0 m^2 (2\pi)^2} \sum_{m>n} \int \frac{f_{nm} |\langle \varphi_{m\mathbf{k}} | \hat{p}_{xy} | \varphi_{n\mathbf{k}} \rangle|^2}{E_{mn}} \pi \delta(E_{mn}^2 - \hbar^2\omega^2) d^2k. \end{aligned}$$

The Dirac delta function can also be written as $\delta(E_{mn} - \hbar\omega)/2\hbar\omega$ for $\omega > 0$. Thus E_{mn} inside the integral is $\hbar\omega$ for all surviving terms of the integral. Rewriting the rest inside the integral as $F(\mathbf{k})$ the equation becomes

$$\text{Im} \{ \chi_{E_{2D}}(\omega) \} = \frac{12e^2}{2\varepsilon_0 m^2 \pi^2 \omega^2} \sum_{m>n} \int_{\text{IBZ}} F(\mathbf{k}) \delta(E_{mn} - \hbar\omega) d^2k, \quad (2.47)$$

with the 12 coming from only taking the integral of the irreducible Brillouin zone. In order to get the Dirac delta function, the dampening was set to vanish, however, the broadening can be reintroduced by convolution with a Gaussian line-shape function so that

$$\text{Im} \{ \chi_{E_{2D}}(\omega) \} = \frac{12e^2}{2\varepsilon_0 m^2 \pi^2 \omega^2} \sum_{m>n} \int_{\text{IBZ}} F(\mathbf{k}) \delta(E_{mn} - \hbar\omega) d^2k \frac{e^{-(\omega-\omega')^2/\Gamma^2}}{\Gamma\sqrt{\pi}} d\omega', \quad (2.48)$$

with Γ being the broadening added. The plasma frequency in Eq. (2.44) also needs to be modified to include a Dirac delta function. In the limit of 0 K the differentiated Fermi distribution becomes a Dirac delta function. Thus the integral can be evaluated at zero temperature and convoluted with the differentiated Fermi-distribution afterwards as

$$\omega_p^2 = -\frac{2e^2}{\varepsilon_0 m^2 (2\pi)^2} \sum_n \int \int \delta(E - E_0) |\langle \varphi_{n\mathbf{k}} | \hat{p}_{xy} | \varphi_{n\mathbf{k}} \rangle|^2 d^2k f'(E_0) dE_0. \quad (2.49)$$

2.4 Basis set considerations

The matrix elements $\langle \varphi_{m\mathbf{k}} | \hat{p}_{xy} | \varphi_{n\mathbf{k}} \rangle$ are calculated in a plane-wave basis. The Kohn-Sham orbitals in a plane wave basis are given as

$$\varphi_{n\mathbf{k}} = \frac{1}{\sqrt{\Omega}} \sum_{\mathbf{G}} C_n(\mathbf{G}) e^{i(\mathbf{k}+\mathbf{G})\cdot\mathbf{r}}, \quad (2.50)$$

with $C_n(\mathbf{G})$ being the expansion coefficients. The momentum operators used in \hat{p}_{xy} is given as $\hat{p}_x = -i\hbar \frac{d}{dx}$ and $\hat{p}_y = -i\hbar \frac{d}{dy}$. The matrix elements are then given by

$$\langle \varphi_{m\mathbf{k}} | \hat{p}_x | \varphi_{n\mathbf{k}} \rangle = \frac{-i\hbar}{\Omega} \sum_{\mathbf{G}} \sum_{\mathbf{G}'} C_m(\mathbf{G}')^* C_n(\mathbf{G}) \int e^{-i(\mathbf{k}+\mathbf{G}')\cdot\mathbf{r}} \frac{d}{dx} e^{i(\mathbf{k}+\mathbf{G})\cdot\mathbf{r}} d^3r = \hbar \sum_{\mathbf{G}} C_m(\mathbf{G}')^* C_n(\mathbf{G}) (G_x + k_x), \quad (2.51)$$

because of the orthogonality of the plane wave basis functions, where G_x and k_x are the x-components of the \mathbf{G} -vector and \mathbf{k} -vector respectively. A similar equation is used for $\langle \varphi_{m\mathbf{k}} | \hat{p}_y | \varphi_{n\mathbf{k}} \rangle$. Due to the projector augmented wave method used in GPAW, described in App. B, a correction to these matrix elements are required

$$\langle \Psi_{m\mathbf{k}} | \nabla | \Psi_{n\mathbf{k}} \rangle = \langle \tilde{\Psi}_{m\mathbf{k}} | \nabla | \tilde{\Psi}_{n\mathbf{k}} \rangle + \sum_{a,ij} \langle \tilde{\Psi}_{m\mathbf{k}} | \tilde{p}_i^a \rangle^* \langle \tilde{\Psi}_{n\mathbf{k}} | \tilde{p}_j^a \rangle \left[\langle \phi_i^a | \nabla_{\mathbf{r}} | \phi_j^a \rangle - \langle \tilde{\phi}_i^a | \nabla_{\mathbf{r}} | \tilde{\phi}_j^a \rangle \right], \quad (2.52)$$

with Ψ being the all-electron wave function, $\tilde{\Psi}$ being the pseudo wave function, \tilde{p}_j^a being the j 'th projector on the a 'th atom, and ϕ and $\tilde{\phi}$ are the partial waves. The first term is the matrix element of the pseudo wave function as given by (2.51) and all four brackets of the sum can be extracted from the result of a GPAW calculation.

2.5 Optical properties of Graphene

Eq. (2.48) and Eq. (2.49) can now be solved with the improved triangle method from Pedersen et al. [25]. In Fig. 2.1(a) the conductivity of graphene is shown, using the point-sampling method and the improved triangle method for the same number of k-points in the irreducible Brillouin zone, in a grid similar to the one shown in Fig. 2.1(b), where the real part of the sheet conductivity is calculated as

$\sigma_1(\omega) = \omega \varepsilon_0 \text{Im}(\chi_{2D}(\omega))$ and is given in units of the quantum unit of conductance $\sigma_0 = \frac{e^2}{4h}$. As $\hbar\omega \rightarrow 0$ the conductivity is supposed to converge to σ_0 , as the graphene conductivity is reported to never fall below this minimum value [2]. However, a great many more k-points is needed for point-sampling, than the improved triangle method to show this behaviour. The interband conductivity also becomes 0 at $\hbar\omega = 0$, but this is determined entirely by the density of the k-points used in the calculation around the \mathbf{K} special point.

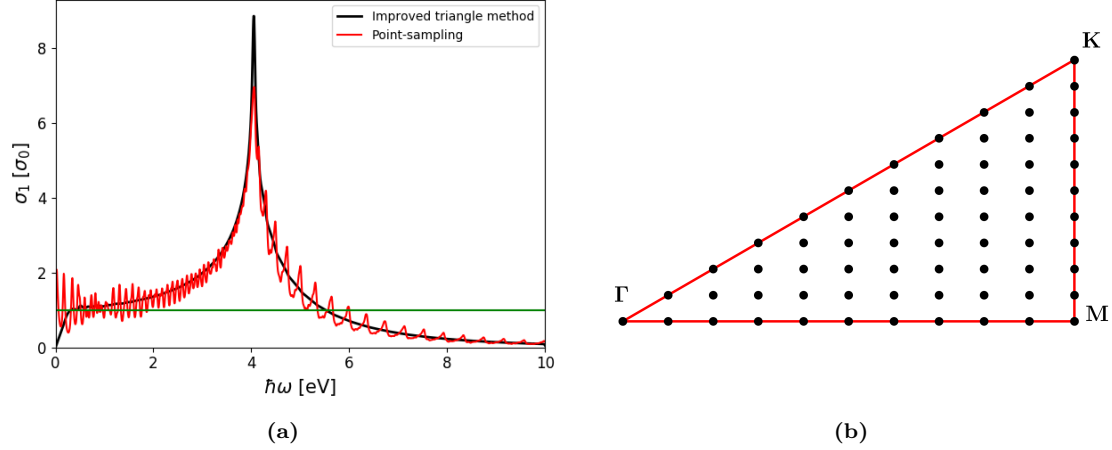


Figure 2.1: (a) Comparison of point-sampling and the improved triangle method for the interband conductivity, with the green line being the Dirac model for interband conductivity. The number of k-points used in both calculations is 1596 in the irreducible Brillouin zone. The dampening of the point sampling was set to 0.025 eV. (b) Example of the type of grid used in the calculations, here shown for a "10x10" grid.

The Dirac model shown in Fig 2.1 comes from a cone approximation of the highest valence band and lowest conduction band of graphene [26]. Assuming spin degeneracy, the density of states can be calculated as

$$D(E) = 2 \sum_{n,\mathbf{k}} \delta(E_{n,\mathbf{k}} - E). \quad (2.53)$$

However, to account for the discretization of \mathbf{k} -space the Dirac-delta function is replaced with a normalized Gaussian as

$$\delta(E_{n,\mathbf{k}} - E) \rightarrow \frac{1}{\gamma\sqrt{2\pi}} e^{-\left(\frac{E-E_{n,\mathbf{k}}}{\sqrt{2}\gamma}\right)^2}, \quad (2.54)$$

with some broadening γ , here chosen to be 0.0025 eV. The density of states of graphene is shown in Fig. 2.2. Close to the top of the highest occupied valence band around 0 eV, the density of states behaves linearly, in good agreement with the Dirac model.

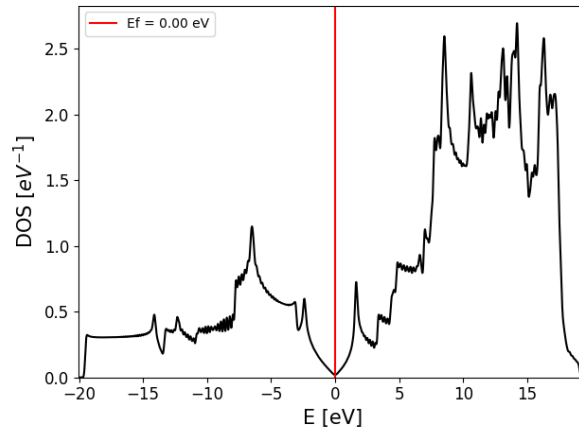


Figure 2.2: Density of states of graphene, showing linear behavior near the top of the highest occupied valence band, at 0 eV.

All valence bands will be designated as v_n with n starting from 1, with v_1 denoting the highest valence band and so on. The conduction bands will be designated c_n with n starting from the lowest conduction band at 1 and the next lowest conduction band being $n = 2$ and so on.

The conductivity of graphene for the $0 < \hbar\omega < 10$ eV range is exclusively due to interband transitions from v_1 and c_1 as shown in Fig. 2.3(a). It is seen that the conductivity has a resonance at 4 eV, which is related to the flatness of the v_1 and c_1 bands between the \mathbf{M} and \mathbf{K} special points in the Brillouin zone. This flatness leads to a high density of states near 4 eV, which in turn translates into the resonance in conductivity. The v_1 and c_1 bands are highlighted in blue in Fig. 2.3(b). As expected, graphene behaves like a semi-metal with the v_1 and c_1 bands touching in the \mathbf{K} special point.

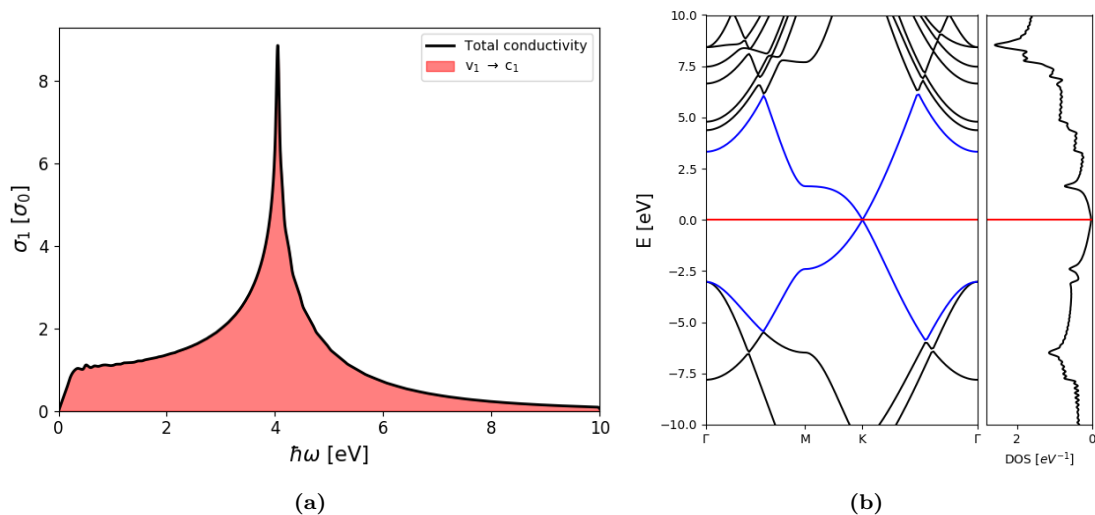


Figure 2.3: (a) Interband conductivity of graphene, with the contribution from the v_1 to c_1 transition shaded in red. (b) Graphene band structure and DOS, highlighting the v_1 and c_1 bands in blue, which are mainly responsible for the conductivity of graphene.

2.6 Optical properties of MoS₂

For MoS₂ the interband conductivity is a bit more complicated as shown in Fig. 2.4(a). The conductivity starts around 1.83 eV, which is the band gap of MoS₂, for a DFT calculation, corresponding to the direct band gap in the band structure shown in Fig. 2.4(b). The 2-3.5 eV region of the spectrum is dominated by the $v_1 \rightarrow c_1$ transition.

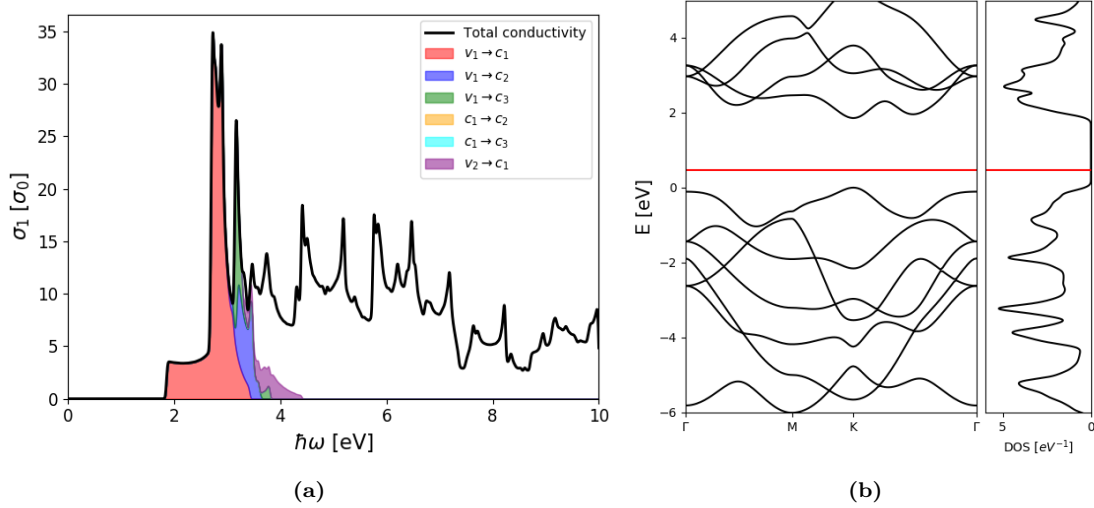


Figure 2.4: (a) Interband conductivity plot of MoS₂, showing the conductivity becoming only non-zero after 1.83 eV due to the band gap of MoS₂. (b) The band structure of MoS₂ along with its DOS.

In order to determine where in the BZ the spectral features originate, the \mathbf{k} integral of Eq. (2.47) can be limited to different regions, as is done in Fig. 2.5(a). The flat low energy part of the conductivity originates from the \mathbf{K} -region. The first peak at 2.73 eV is caused by the Γ region, with Fig. 2.5(b) showing that both the $\Gamma \rightarrow \mathbf{M}$ and $\Gamma \rightarrow \mathbf{K}$ part contributes to this peak. Fig. 2.5(b) also shows that just around Γ all matrix elements are zero, so the Γ contributions of Fig. 2.5(a) all originate from the outer parts of the Γ region. The second peak at 2.89 eV is due to the area dubbed 'Rest', and it can be seen from Fig. 2.5(b) that the maximum between Γ and \mathbf{K} has eigenvalues corresponding to this transition.

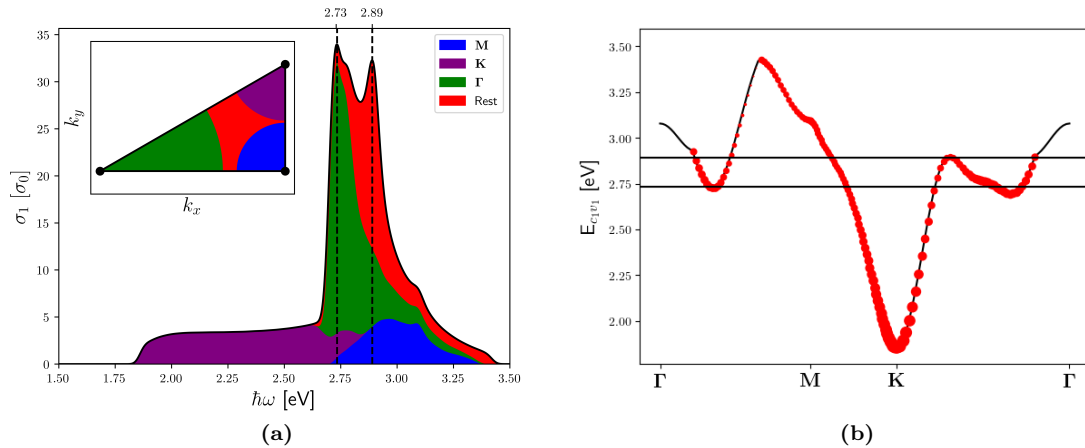


Figure 2.5: (a) Contribution to the $v_1 \rightarrow c_1$ part of the optical conductivity from different regions of the Brillouin zone. The inset shows the integration regions. (b) Difference in eigenvalues between the c_1 and v_1 bands, with the size of circles indicating the magnitude of the momentum matrix element. Horizontal lines indicate the transition energy of the two peaks from (a).

Chapter 3

Doping Models

Doping is an essential process in the manufacturing and design of micro- and nano-electronics, as it is the mechanism that enables the functionality of a range of semiconductor devices. Doping refers to adding additional charge carriers to a region of a semiconductor material. The addition of extra holes and extra electrons to separate adjoining regions is what creates the simplest semiconductor device, the pn junction and more advanced devices can be built by more elaborate doping profiles. [27]

For three dimensional semiconductors, such as the archetypal silicon that is the workhorse of the semiconductor industry today, doping is normally done by so-called substitutional doping. In this scheme a silicon atom in the lattice is replaced by group III or group V atoms, which respectively lack an electron and has an extra electron compared to silicon. Focusing on the case of group V atoms, at low temperature this extra electron will reside in a state close to the conduction band that is easily excitable to the conduction band, generating a free carrier. [27]

For the two-dimensional materials, that are the focus of this thesis, substitutional doping is also a possibility, and has been the focus of several studies [28–30]. However, due to the reduced dimensionality other doping strategies become possible. One such possibility is doping by adatom surface adsorption, which has been used to create field effect transistors on MoS₂ and DFT studies have been done exploring the effect of different adatoms on the band structure of MoS₂ [31, 32].

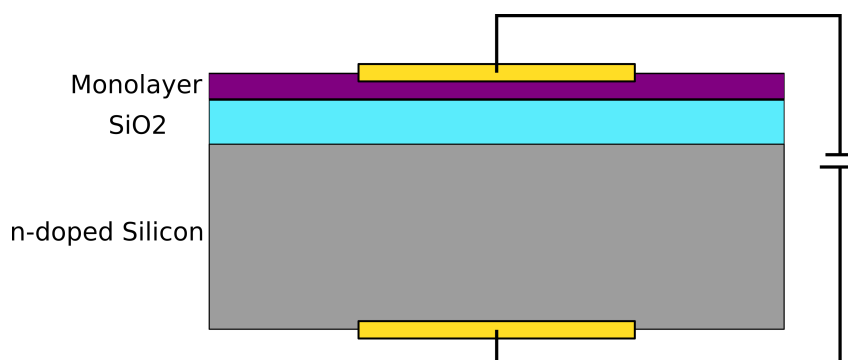


Figure 3.1: Schematic of capacitor for electrostatic doping of monolayer.

A third possibility, which while possible in 3D is more effective in 2D, is that of injecting charge carriers by gating, essentially utilizing the field effect. From a device design perspective this can be achieved by depositing a MoS₂ layer on a dielectric layer, grown on a substrate and subsequently depositing metallic gates on the MoS₂ layer and a back-gate on the silicon substrate. A voltage across the gates will move free charge carriers from the substrate into the monolayer and the doping can thus be controlled

electrically. This offers the possibility of creating re-configurable devices. While this doping strategy can be modelled on the device level, using standard semiconductor equations in conjunction with e.g. finite element methods, it is not obvious how to include it in ab-initio calculations of the electronic properties of MoS₂. A schematic of such a device is shown in Fig. 3.1.

3.1 Electrostatic doping models

For substitutional and adsorption doping the same computational strategy is essentially used in literature. A supercell containing several unit cells of the monolayer and an additional atom is constructed and the system is relaxed to its most energetically favourable positions and a DFT calculation using the relaxed geometry can be carried out [31, 32]. The doping density then depends on the dopant atom and the size of the supercell, with a larger supercell leading to fewer extra carriers per unit cell. This strategy will not adequately describe the presence of a gating potential as the electronic structure is no longer that of the pristine monolayer but rather the supercell including interactions between the monolayer and the adatom. However, if the relaxation procedure is ignored and the adatom is moved away from its equilibrium position the monolayer-adatom interactions will decrease, yet charge transfer will still occur. In a supercell of the appropriate size the bands belonging to the dopant atom will be flat as interactions between dopants in periodically repeated unit cells are weak. The geometry of the a 3x3 supercell is shown in Fig. 3.2.

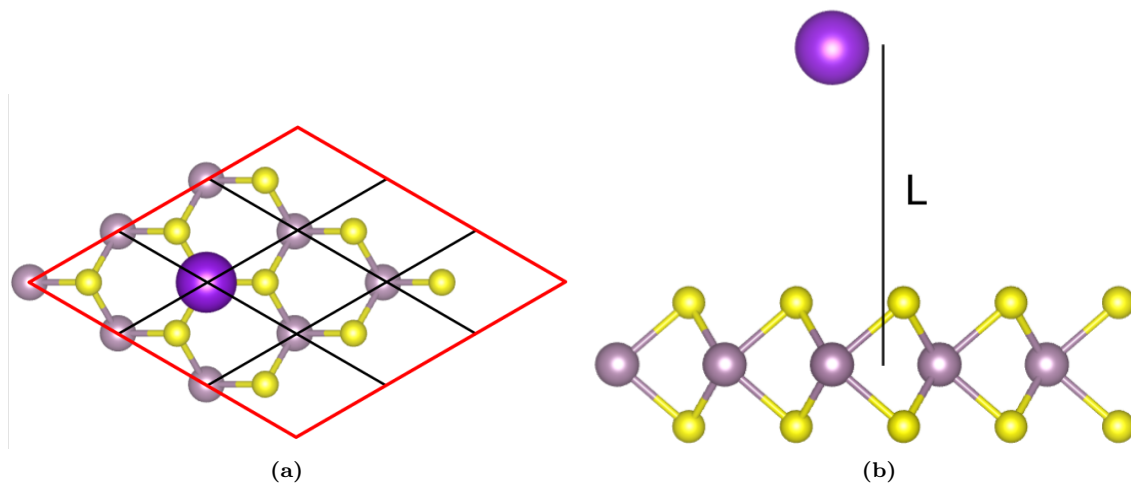


Figure 3.2: The 3x3 MoS₂ supercell used in the electrostatic doping models. (a) Supercell seen from above with an adatom above of a molybdenum atom. (b) Supercell from the side, showing the variable z-distance "L" between the layer and the adatom.

In order to determine the amount of charge transfer between the dopant atom and the layer, Bader analysis can be utilized. The idea of Bader analysis is to look for regions bounded by minimas in the electron density. Such regions will often contain a nucleus and the integrated electron density in the region is assigned to that nucleus. [33]

Another possibility is to just add or remove a fraction of an electron from the DFT calculation and compensate with a homogeneous background, a so called jellium, ensuring charge neutrality in the unit cell. This model has the advantage that a supercell is not required to obtain realistic doping levels, and everything can be done in the primitive unit cell of the material in question.

Calculations utilizing the doping models described above have been performed. The first model utilizes K and Li dopant atoms, which both n-dope MoS_2 . The calculations are carried out as follows

1. A 3×3 supercell self-consistent-field (SCF) calculation, with the dopant atom position a variable distance above the Molybdenum atom is performed
2. Bader analysis is used to determine the charge transfer from the dopant atom.
3. A SCF calculation with a jellium background and additional electrons equal to the charge transfer found by the Bader analysis is done in a 3×3 supercell.
4. Non-SCF calculations, using the electron density found from the SCF calculations, with a denser k-point grid for calculating the density of states and band structure.
5. Use the density of states to calculate the Fermi level.

DFT calculations in the GPAW code have been performed with the dopant atom 3 to 15 Å, with 1 Å steps, above the Mo atom. The supercell height was chosen to be 40 Å to ensure that the dopant atom did not interact with the Mo layer in a periodic image. The lattice constant and the z-position of S was chosen based on relaxation of the MoS_2 with the default GPAW PAW setups in plane-wave mode, leading to values of 3.115 Å and 1.551 Å respectively. Due to the large amount of electrons in a 3×3 supercell and the large vacuum layer, using a plane-wave basis for these calculations is very computationally demanding and instead a localized double-zeta-polarized (DZP) basis set was used. The SCF ground state calculations were performed on a $(4 \times 4 \times 1)$ Monkhorst Pack grid and a $(70 \times 70 \times 1)$ grid was used for calculating the DOS and a route with 200 k-points was used for evaluating band structures. The freely available program developed by Henkelman et al. that implements an efficient algorithm for Bader analysis was used for step 2 [34].

The band structure of a 3×3 MoS_2 supercell without any dopant atom or jellium background is shown in Fig. 3.3(a). Due to the increased size of the supercell, the 3×3 Brillouin zone is folded, causing the direct band gap to be located at the Γ -point with a value of 1.87 eV. The calculation is in good agreement with a similar calculation by Rastogi et al. [31].

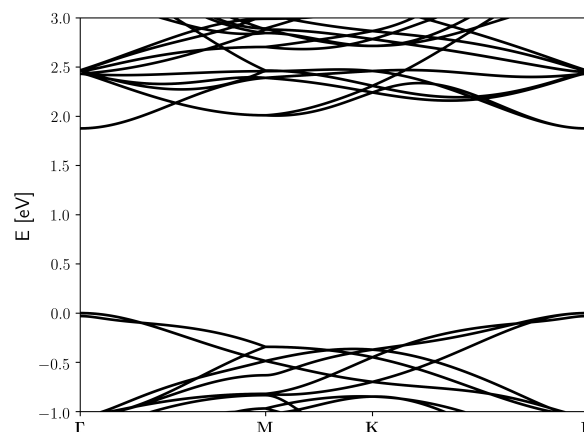


Figure 3.3: Band structure of pristine MoS_2 3×3 supercell

When a dopant atom is included in the supercell its influence depends on its distance to the layer. If it is close to the layer the system will represent the case of an atom adsorbed on the surface, which will affect

the shape of the bands. In this case distinguishing between the states of the layer and the states of the dopant atom is difficult, at least from the band structure. As the atom is moved away, the interaction should diminish and the bands of the atom should represent states which experience no interaction, i.e. become flat. In Fig. 3.4 the band structure for K and Li with the dopant atom at a distance of 4 and 13 Å from the monolayer is shown.

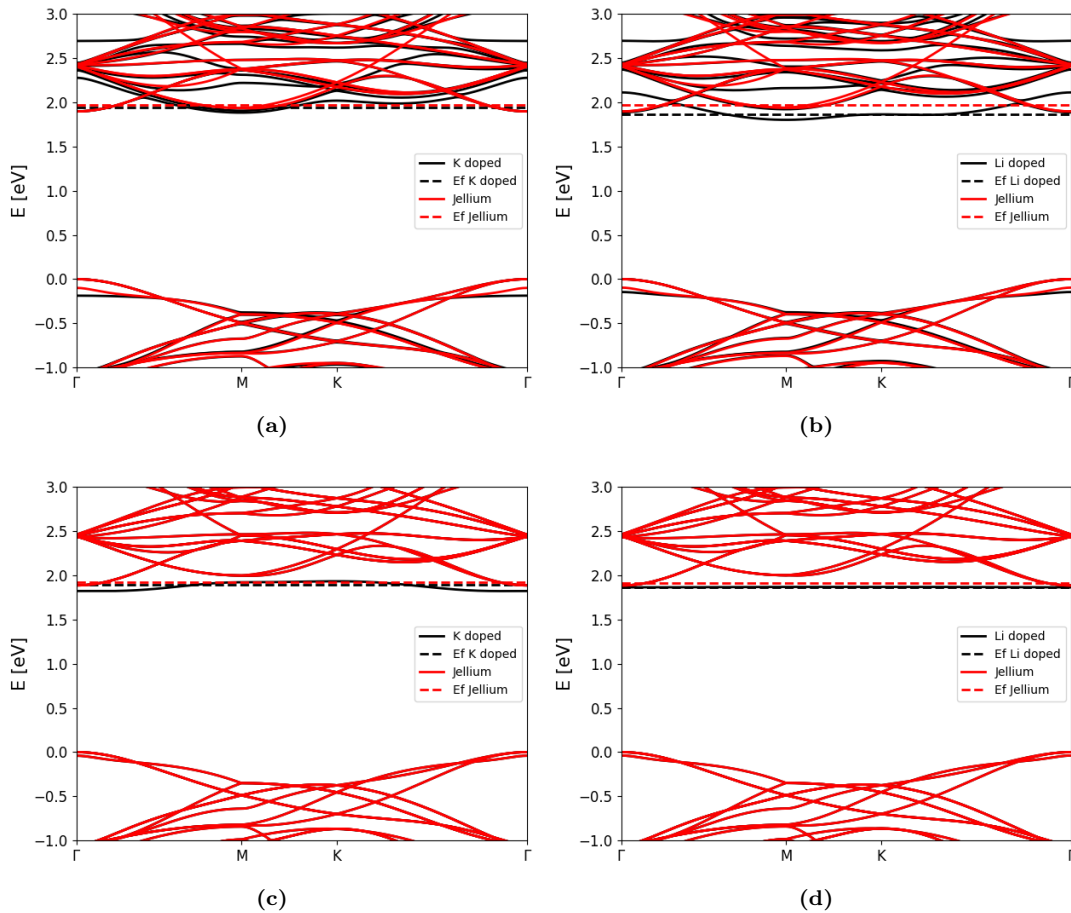


Figure 3.4: Band structures of MoS₂ 3x3 supercells with (a) K at L = 4 Å, (b) Li at L = 4 Å, (c) K at L = 13 Å, (d) Li at L = 13 Å. The black bands are from calculations including the dopant atom, while the red bands are from a calculation with a jellium background with a charge equivalent to the charge transfer from the dopant atom.

For all the band structures shown in Fig. 3.4 the jellium calculations are nearly identical to the pristine MoS₂ band structure shown in Fig. 3.3. In Fig. 3.4(a) and (b) K and Li atoms are placed 4 Å away from the monolayer, in both cases the band structure differs significantly from the band structure of the jellium calculations as expected from the argument above. When the dopant atoms are moved further away, as shown in Fig. 3.4(c) and (d), the interaction between the layer and the dopant atoms becomes weak and the bands align completely with those of the equivalent jellium calculation, except for a band just under the MoS₂ conduction band. For K it can be seen that this band is not entirely flat and further increasing the distance of the dopant atom does not change it significantly, while for Li the band is completely flat. This can be explained by the positions of K and Li in the periodic table having atomic numbers of 19 and 3 respectively, meaning that K is much larger enabling interactions with K atoms in neighbouring supercells. Using a 4x4 supercell would increase the distance between K atoms, but would require more

computational resources. The L-position required in order to reduce the dopant-layer interaction enough for the bands to align is 7 \AA for both K and Li.

As described earlier the charge transfer from the dopant atom to the MoS_2 layer was calculated from Bader analysis. The charge transfer as a function of the distance of the dopant atom is shown in Fig. 3.5. In both cases the charge transfer decreases asymptotically as the distance is increased. However, for K a slight increase in the charge transfer is observed from $L = 3 \text{ \AA}$ to $L = 4 \text{ \AA}$, likely due to it's preferred relaxed position being in that range, this is not seen for Li likely because it's relaxed position is smaller than $L = 3 \text{ \AA}$ due to it's small size. Considering that 7 \AA is required for the dopant bands to become flat, the model works only in the $L > 7 \text{ \AA}$ range, thus the doping can be controlled from 0.3 to 0.1 and 0.2 to 0.1 electrons per supercell for K and Li respectively, corresponding to doping densities of $0.99 * 10^{13} \text{ cm}^{-2}$ to $0.33 * 10^{13} \text{ cm}^{-2}$.

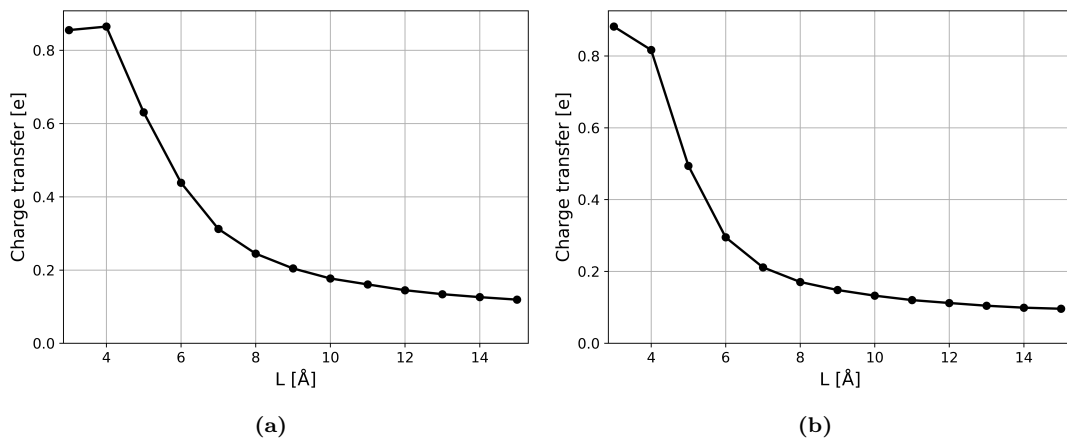


Figure 3.5: Charge transfer as a function of dopant atom position for (a) K and (b) Li

For each value of the charge transfer a corresponding jellium calculation was performed and for both the dopant calculation and the jellium calculation the Fermi level was calculated. Fig. 3.6 shows the Fermi level as a function of the charge transfer for both K and Li. In both cases the Fermi level is more well behaved in the jellium calculations.

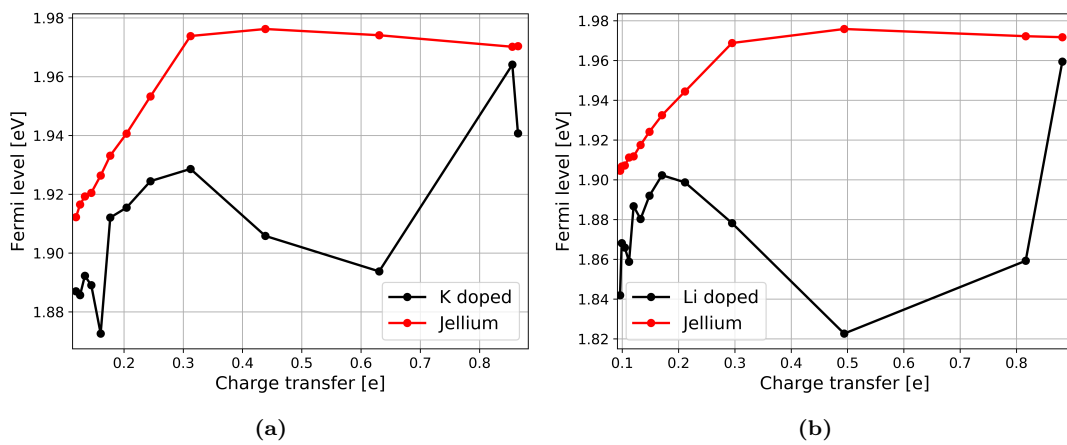


Figure 3.6: Fermi level as a function of charge transfer above the highest valence band for (a) K and (b) Li.

The analysis has shown that both doping strategies are viable. However, the jellium model has a few distinct advantages. First, it does not require a supercell to be viable, thus decreasing the computational requirements and perhaps more importantly allowing the use of a plane-wave basis set, which makes computing certain matrix elements significantly easier. Secondly, in the jellium model the amount of charge added to the layer can be directly input into the calculation, whereas in the dopant model only the z-position can be specified. The jellium model can also cover a wider range of doping concentrations. Due to these considerations the jellium model has been used for the remainder of the calculations in this work.

3.2 Doping in graphene

The jellium model described above can be used directly with the response theory presented in Chap. 2. At high doping concentrations a simple expression for the relation between the Fermi level and the doping concentration can be derived leading to

$$E_F = \hbar v_F \sqrt{\pi n}, \quad (3.1)$$

where v_F is the Fermi velocity [22]. Fig. 3.7 shows the Fermi level as a function of the doping concentration from DFT calculations. The agreement with the square-root relation is very good, considering the expected value of the Fermi velocity is around $1 \cdot 10^6$ m/s [35]. At low doping concentrations the agreement is worse, which can be explained by Eq. (3.1) being derived for the limit where $|E_F|/kT \gg 1$.

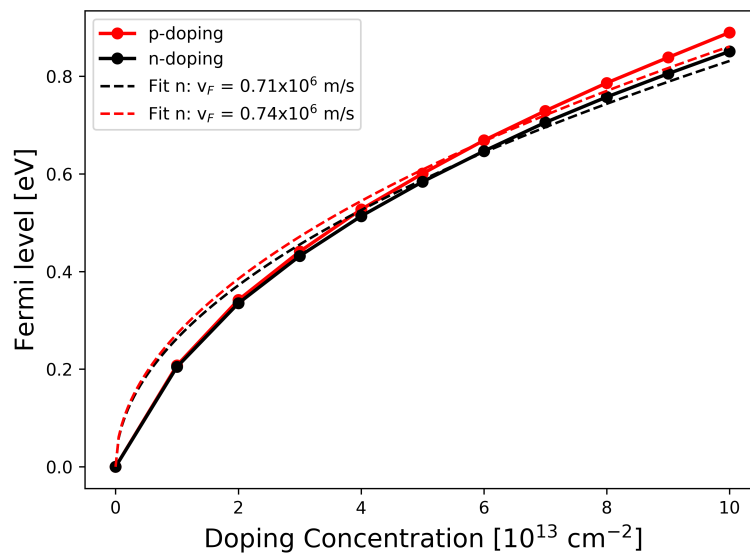


Figure 3.7: Fermi level versus doping concentration in graphene.

The effects on the interband conductivity is shown in Fig. 3.8(a), where graphene was doped with $2 \cdot 10^{13} \text{ cm}^{-2}$ electrons. It is clear that the interband conductivity at low frequencies is gone, which is due to so-called Fermi-blocking, because the lowest states of the c_1 band are now occupied. Fermi-blocking only increases further with doping concentration as shown in Fig. 3.8(b), where graphene was doped with $10 \cdot 10^{13} \text{ cm}^{-2}$ electrons. Furthermore, the interband conductivity is no longer only due to the $v_1 \rightarrow c_1$ transition as seen in the high frequency range near 9-10 eV, where the $c_1 \rightarrow c_2$ interband transition is contributing.

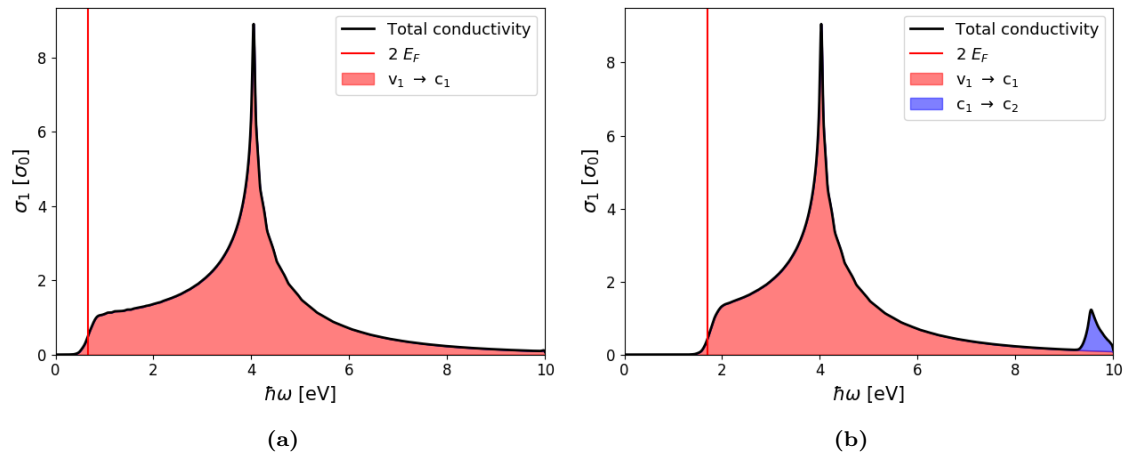


Figure 3.8: (a) Interband conductivity of graphene doped with $2 \cdot 10^{13} \text{ cm}^{-2}$ electrons, with the contribution from the $v_1 \rightarrow c_1$ transition shaded in red. (b) $10 \cdot 10^{13} \text{ cm}^{-2}$ electrons, with the contribution from the $v_1 \rightarrow c_1$ transition shaded in red, and the contribution from the $c_1 \rightarrow c_2$ transition shaded in blue.

This new contribution can also be explained by shift of the Fermi-level. As the Fermi-level increases more states in the c_1 band become occupied. These occupied states can then transition to the c_2 band, however the energy required is high, due to the occupied states being only near the \mathbf{K} special point, where the c_2 band is highly separated from the c_1 band as shown in figure 3.9(a-b) for $2 \cdot 10^{13} \text{ cm}^{-2}$ electrons and $10 \cdot 10^{13} \text{ cm}^{-2}$ electrons, respectively.

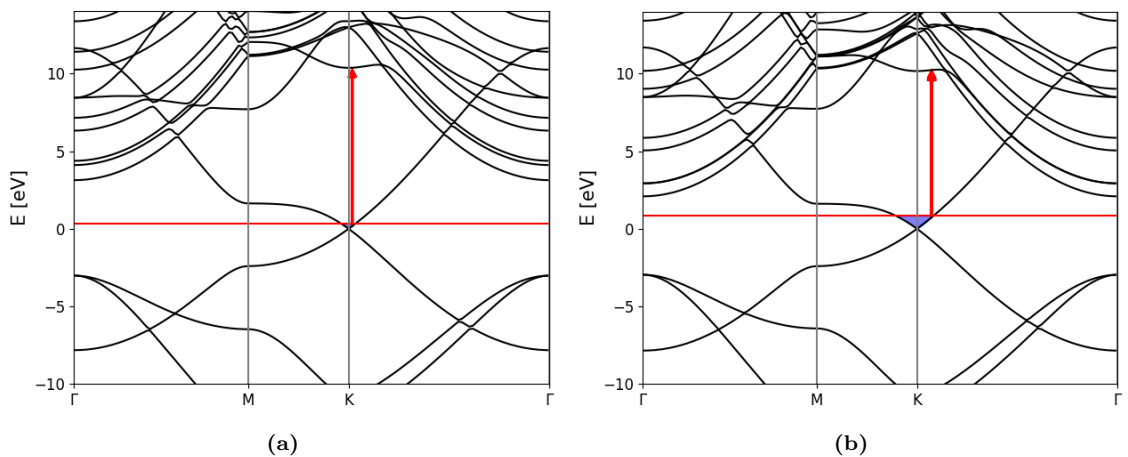


Figure 3.9: (a) Bandstructure of graphene doped with $2 \cdot 10^{13} \text{ cm}^{-2}$ electrons, occupied c_1 band states shaded in blue, and a red arrow indicating the smallest transition in energy between the c_1 occupied states and the c_2 band. (b) $10 \cdot 10^{13} \text{ cm}^{-2}$ electrons, showing the same, however the $c_1 \rightarrow c_2$ transition is now below 10 eV and therefore visible in the conductivity plot.

Furthermore the conduction bands decrease in energy with increasing doping, as is shown in Fig. 3.10 with the black solid bands being the conduction bands at 0 doping, while the red dashed bands being the same conduction bands where graphene has been doped with $10 \cdot 10^{13} \text{ cm}^{-2}$ electrons. However, the c_1 band around the \mathbf{K} special point does not change at all.

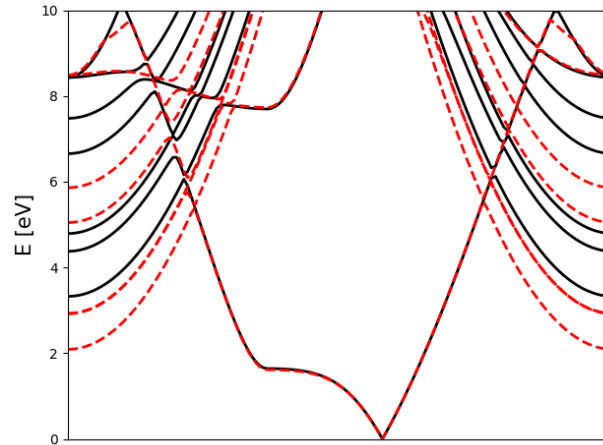


Figure 3.10: Conduction bands of graphene at 0 doping (black solid lines) and doping with $10 \cdot 10^{13} \text{ cm}^{-2}$ electrons (red dashed lines).

It is natural that the intraband contribution to the conductivity will increase as the Fermi-level shift increases the amount of occupied states in the c_1 band. The intraband contribution for $2 \cdot 10^{13} \text{ cm}^{-2}$ electrons and $10 \cdot 10^{13} \text{ cm}^{-2}$ electrons, respectively is shown in Fig. 3.11.

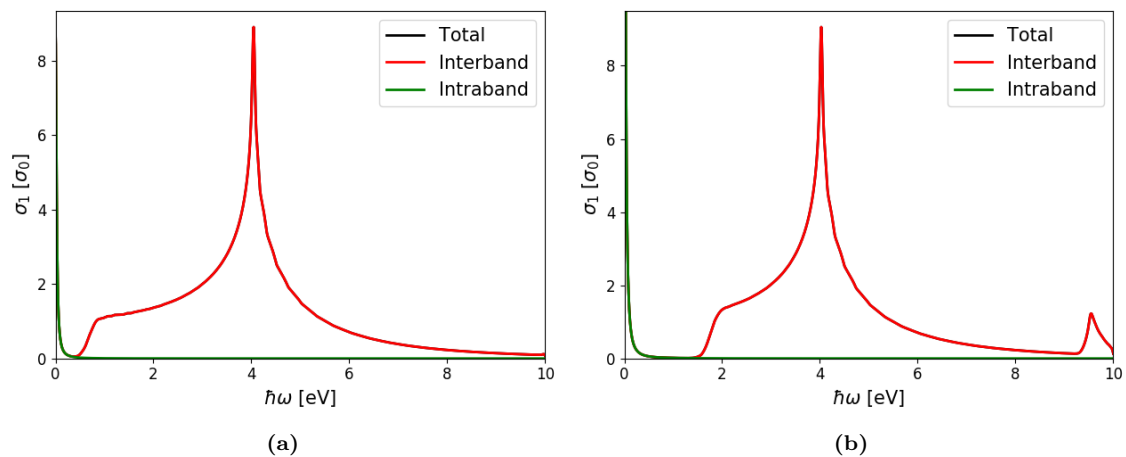


Figure 3.11: Conductivity of graphene doped with (a) $2 \cdot 10^{13} \text{ cm}^{-2}$ electrons, and (b) $10 \cdot 10^{13} \text{ cm}^{-2}$ electrons, showing intraband contribution becoming more important at low frequencies with increasing doping concentration.

The effect of doping on the intraband conductivity is easier to see when looking at the plasma-frequency as a function of the Fermi-level. In Fig. 3.12(a) it is clear that the plasma-frequency increases as the Fermi-level is shifted away from the point where v_1 and c_1 has the same energy. The DFT calculation fits well with the Dirac model, however the plasma frequency of the DFT calculation is lower for a Fermi-level of 0 eV, however this can also be attributed to the density of the k-points used in the DFT calculation. Fig. 3.12(b) shows a tight-binding calculation of the plasma frequency at a Fermi level of 0 eV at room temperature with increasing k-points, showing that as more k-points are added the plasma frequency converges to the analytical value.

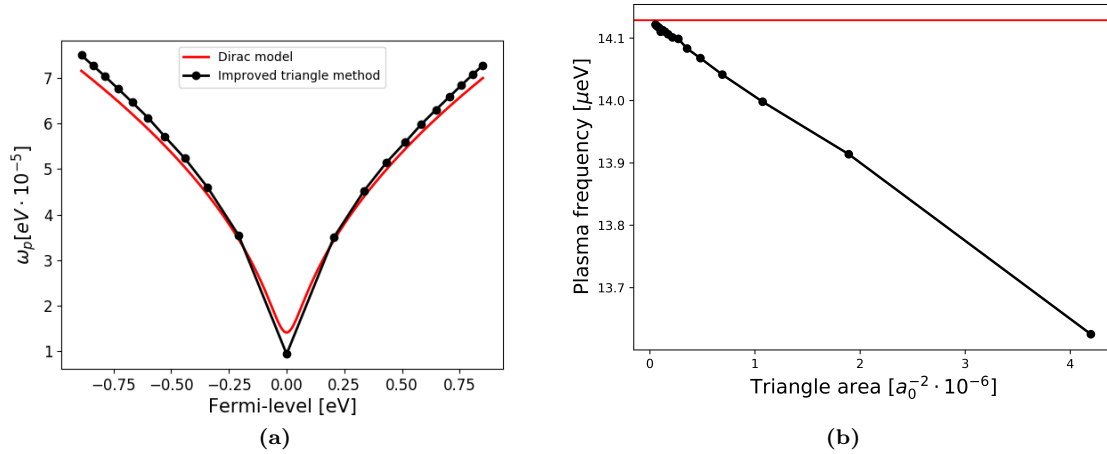


Figure 3.12: (a) Plasma-frequency of graphene as a function of Fermi-level, showing the effects of doping. (b) Tight-binding calculation of the plasma frequency for Fermi level at 0 eV, showing that the plasma frequency converges with increasing k-point density. Triangle area denotes the area of the triangles used in the grid for the improved triangle method.

3.3 Doping in MoS₂

For MoS₂ Fermi-blocking is less apparent as shown in Fig. 3.13, because the Fermi level moves only very slowly into the conduction band.

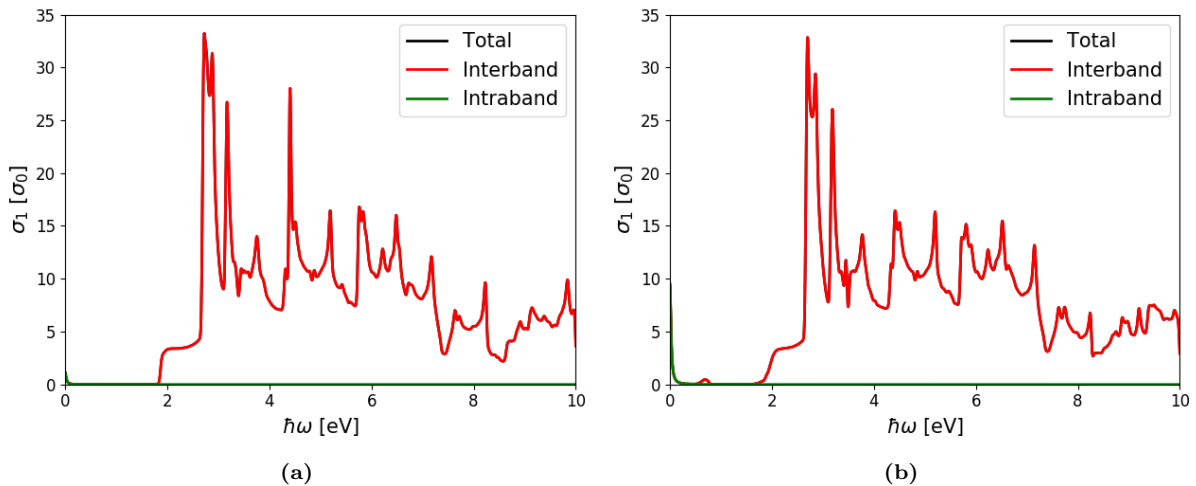


Figure 3.13: Conductivity of MoS₂ doped with (a) $2 \cdot 10^{13} \text{ cm}^{-2}$ electrons, and (b) $10 \cdot 10^{13} \text{ cm}^{-2}$ electrons, showing some intraband contribution at low frequencies with increasing doping concentration.

At higher doping concentrations a small interband contribution begins to show far below 1.83 eV as shown in Fig. 3.14(a) for MoS₂ doped with $10 \cdot 10^{13} \text{ cm}^{-2}$ electrons. This small contribution is due to the $c_1 \rightarrow c_2$ transition from the occupied states in the valley in the c_1 band between the \mathbf{K} and $\mathbf{\Gamma}$ special points as indicated by the red arrow in Fig. 3.14(b).

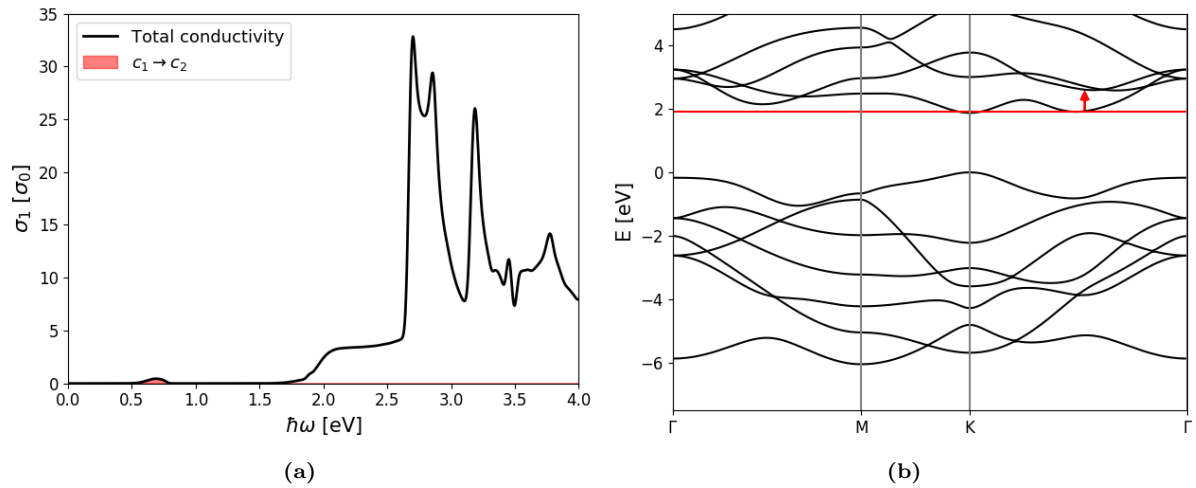


Figure 3.14: (a) Interband conductivity of MoS₂ doped with $10 \cdot 10^{13} \text{ cm}^{-2}$ electrons, showing a small contribution from the $c_1 \rightarrow c_2$ transition. (b) Band structure of MoS₂ at the same doping concentration, with a red arrow indicating the $c_1 \rightarrow c_2$ transition corresponding to around 0.6 eV.

Chapter 4

Excitons

Thus far a framework has been presented that allows for the calculation of the optical properties within a independent particle picture. However, this framework is in poor agreement with experiments for MoS₂ [10]. In this chapter the Bethe-Salpeter framework that allows for the inclusion of excitons is presented. In the first section the Bethe-Salpeter equation is derived, followed by an analytical model for the screening of 2D materials. After which the calculation of matrix elements is discussed, leading to the Wannier model, which allows for calculating approximative binding energies in a much less complicated fashion. The remaining sections consider the details of using the Bethe-Salpeter equation and presents results for MoS₂.

4.1 The Bethe-Salpeter equation

In order to obtain more accurate optical properties, many-body effects have to be included. DFT calculations are based on representing the all-electron wave function as a Slater determinant, where the ground-state Slater determinant is given by valence Kohn-Sham (KS) orbitals. An intuitive way to obtain an excited state is to replace one valence KS orbital with a conduction KS orbital. A singly excited Slater determinant with total spin equal to zero, can be defined as a superposition of Slater determinants with a valence spin up orbital replaced by a conduction spin up orbital and likewise for spin down

$$|v_i \rightarrow c_j\rangle = \frac{1}{\sqrt{2}} \left(|v_i^\uparrow \rightarrow c_j^\uparrow\rangle + |v_i^\downarrow \rightarrow c_j^\downarrow\rangle \right), \quad (4.1)$$

so that the excited state can be expressed in a basis of singly excited states

$$|S\rangle = \sum \alpha_{ij} |v_i \rightarrow c_j\rangle. \quad (4.2)$$

The Hamiltonian describing this excited state consists of a single-particle term and a Coulomb two-particle term

$$H = \sum_n h(\mathbf{r}_n) + \sum_{n<m} W(\mathbf{r}_n - \mathbf{r}_m), \quad (4.3)$$

where W is the screened Coulomb interaction. The equation governing this system is

$$H |S\rangle = E |S\rangle. \quad (4.4)$$

Multiplying by one conjugated basis function from the left and integrating, amounts to multiplying by the bra form of a basis function:

$$\sum_{ij} \alpha_{ij} \langle v_k \rightarrow c_l | H |v_i \rightarrow c_j\rangle = E \sum_{ij} \alpha_{ij} \langle v_k \rightarrow c_l |v_i \rightarrow c_j\rangle = E \alpha_{kl}, \quad (4.5)$$

where the last equality is due to orthonormality of the states. Eq. (4.5) is an eigenvalue problem, and can be solved by diagonalizing the matrix $H_{ij,kl}$ defined by the left side of the equation. The problem is then to compute the matrix elements of this equation, which amounts to computing matrix elements between Slater determinants. Using Eq. (4.1) the matrix elements become

$$\begin{aligned} \langle v_k \rightarrow c_l | H | v_i \rightarrow c_j \rangle = \frac{1}{2} \left[\langle v_k^\uparrow \rightarrow c_l^\uparrow | H | v_i^\uparrow \rightarrow c_j^\uparrow \rangle + \langle v_k^\downarrow \rightarrow c_l^\downarrow | H | v_i^\downarrow \rightarrow c_j^\downarrow \rangle \right. \\ \left. + \langle v_k^\uparrow \rightarrow c_l^\uparrow | H | v_i^\downarrow \rightarrow c_j^\downarrow \rangle + \langle v_k^\downarrow \rightarrow c_l^\downarrow | H | v_i^\uparrow \rightarrow c_j^\uparrow \rangle \right], \end{aligned} \quad (4.6)$$

with the first two terms being between singly excited states of the same spin, and the last two terms being cross-terms between singly excited states with opposite spin. Evaluating the diagonal elements of the first term using the rules of matrix elements between Slater determinants yields [36]

$$\begin{aligned} \langle v_i^\uparrow \rightarrow c_j^\uparrow | H | v_i^\uparrow \rightarrow c_j^\uparrow \rangle = 2 \sum_{n \neq i}^N \langle v_n | h | v_n \rangle + \langle c_j | h | c_j \rangle \langle \uparrow | \uparrow \rangle + \langle v_i | h | v_i \rangle \langle \downarrow | \downarrow \rangle \\ + \sum_{n,m}^N (2 \langle v_n v_m | W | v_n v_m \rangle - \langle v_n v_m | V | v_m v_n \rangle) + \langle v_i c_j | W | v_i c_j \rangle \langle \downarrow | \downarrow \rangle \langle \uparrow | \uparrow \rangle \\ - \sum_m^N (2 \langle v_i v_m | W | v_i v_m \rangle - \langle v_i v_m | V | v_m v_i \rangle) + \sum_{m \neq i}^N (2 \langle c_j v_m | W | c_j v_m \rangle - \langle c_j v_m | V | v_m c_j \rangle). \end{aligned}$$

The first term on the right hand side is a sum of single particle terms neglecting the i 'th valence orbitals and the 2nd and 3rd terms are corrections. The fourth term corresponds to the ground state two-particle terms, and the remaining terms correct this for the excited state. As the last term is limited to $m \neq i$ a Coulomb term between the i 'th spin down valence orbital and the j 'th spin up conduction orbital is added. Exchange terms require both orbitals to be the same spin and thus no exchange term between $v_i \downarrow$ and $c_j \uparrow$ exists. The second term of Eq. (4.6) is exactly the same. Thus, for the diagonal, only the cross terms remain. As there are two differences between the Slater determinants of the cross terms, single particle terms are zero and the two particle contribution is

$$\langle v_i^\uparrow \rightarrow c_l^\uparrow | H | v_i^\downarrow \rightarrow c_j^\downarrow \rangle = \langle v_i^\downarrow c_j^\uparrow | W | c_j^\downarrow v_i^\uparrow \rangle. \quad (4.7)$$

Easier notation can be made by comparing with the ground state

$$\langle 0 | H | 0 \rangle = 2 \sum_n^N \langle v_n | h | v_n \rangle + \sum_{n,m} (2 \langle v_n v_m | W | v_n v_m \rangle - \langle v_n v_m | V | v_m v_n \rangle), \quad (4.8)$$

and defining quasi-particle energies as

$$\begin{aligned} E_{c_j} &= \langle c_j | h | c_j \rangle + \sum_m^N (2 \langle c_j v_m | W | c_j v_m \rangle - \langle c_j v_m | V | v_m c_j \rangle) \\ E_{v_i} &= \langle v_i | h | v_i \rangle + \sum_m^N (2 \langle v_i v_m | W | v_i v_m \rangle - \langle v_i v_m | V | v_m v_i \rangle), \end{aligned} \quad (4.9)$$

which correspond to the quasiparticle energies which could be obtained from the GW approximation. Now writing the full diagonal matrix elements on the form of the ground state matrix element gives

$$\langle v_i \rightarrow c_j | H | v_i \rightarrow c_j \rangle = \langle 0 | H | 0 \rangle + E_{c_j} - E_{v_i} - \langle v_i c_j | W | v_i c_j \rangle + 2 \langle v_i c_j | V | c_j v_i \rangle. \quad (4.10)$$

As the sum in E_{c_j} is not limited to $m \neq i$ the third term compensates for an extra Coulomb term compared to the single Coulomb term given by the matrix elements between up-up and down-down

Slater determinants, while the fourth term compensates for the subtraction of an exchange term which is present in the cross-terms. For the off-diagonal matrix elements, which are also given by the four terms in Eq. (4.6), there are always two differences between the Slater determinants. For the spin up on spin up part this yields

$$\langle v_k^\uparrow \rightarrow c_l^\uparrow | H | v_i^\uparrow \rightarrow c_j^\uparrow \rangle = \langle c_l^\uparrow v_i^\uparrow | W | v_k^\uparrow c_j^\uparrow \rangle - \langle c_l^\uparrow v_i^\uparrow | V | c_j^\uparrow v_k^\uparrow \rangle, \quad (4.11)$$

where both terms survive after spin integration. Both cross terms yield

$$\langle v_k^\uparrow \rightarrow c_l^\uparrow | H | v_i^\downarrow \rightarrow c_j^\downarrow \rangle = \langle c_l^\uparrow v_i^\downarrow | W | v_k^\uparrow c_j^\downarrow \rangle - \langle c_l^\uparrow v_i^\downarrow | V | c_j^\downarrow v_k^\uparrow \rangle = \langle c_l^\uparrow v_i^\downarrow | W | v_k^\uparrow c_j^\downarrow \rangle, \quad (4.12)$$

where the last equality is due to the spin integration. These equations can be combined to finally give an expression for the full matrix elements

$$\langle v_k \rightarrow c_l | H | v_i \rightarrow c_j \rangle = [E_{c_j} - E_{v_i}] \delta_{ki} \delta_{lj} - \langle c_l v_i | W | c_j v_k \rangle + 2 \langle c_l v_i | V | v_k c_j \rangle, \quad (4.13)$$

where the ground state has been chosen as the zero-point energy. For periodic structures the indices used so far need to be understood as composites of band and k-point. The basis Slater determinants of Eq. (4.1) are thus replaced with $|v_{i\mathbf{k}} \rightarrow c_{j\mathbf{k}'}\rangle$ considering only excited states created through optical processes, which involve photons with negligible momentum, a fair assumption is $\mathbf{k} = \mathbf{k}'$. Thus the matrix elements become

$$\langle v_{k\mathbf{k}} \rightarrow c_{l\mathbf{k}} | H | v_{i\mathbf{k}} \rightarrow c_{j\mathbf{k}'} \rangle = [E_{c_{j\mathbf{k}}} - E_{v_{i\mathbf{k}}}] \delta_{ki} \delta_{lj} \delta_{\mathbf{k}\mathbf{k}'} - \langle c_{l\mathbf{k}} v_{i\mathbf{k}} | W | c_{j\mathbf{k}'} v_{k\mathbf{k}} \rangle + 2 \langle c_{l\mathbf{k}} v_{i\mathbf{k}} | V | v_{k\mathbf{k}} c_{j\mathbf{k}'} \rangle. \quad (4.14)$$

This is the Bethe-Salpeter matrix. [22]

4.2 Quasi-particle energy

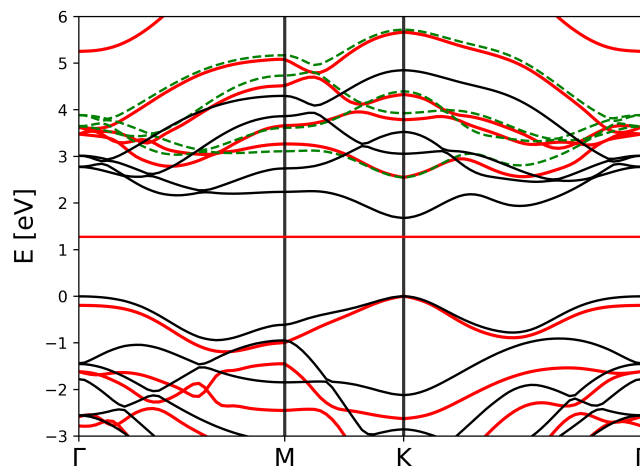


Figure 4.1: DFT and G0W0 band structure of MoS₂, black bands are DFT while red bands are G0W0 and dashed green bands are scissor shifted DFT.

From DFT independent-particle Kohn-Sham eigenvalues can be obtained, however the energies that enter a Bethe-Salpeter calculation should be true quasiparticle energies that include electron-electron interactions, obtained from e.g. GW calculations. The G0W0 band structure of MoS₂ has been calculated

using the GPAW code and is shown in Fig. 4.1 along with the DFT band structure. The zeros in G0W0 refer to both the Green's function and the screened potential being found directly from DFT without iterating for a self-consistent solution [37]. The main difference between the two band structures is that the G0W0 conduction bands are shifted upwards, this enables the use of a scissor operator that shifts the DFT conduction bands to align with the G0W0 bands. A scissor of 0.87 eV is used for the green bands in Fig. 4.1, which greatly decreases the difference between the DFT and G0W0 bands, so that the scissored DFT eigenvalues are a fair approximation for the QP energies. Unless explicitly specified the remainder of the results presented in this chapter are calculated using scissor-shifted DFT energies, but G0W0 calculations are revisited in Chapter 5.

4.3 Screening in 2D

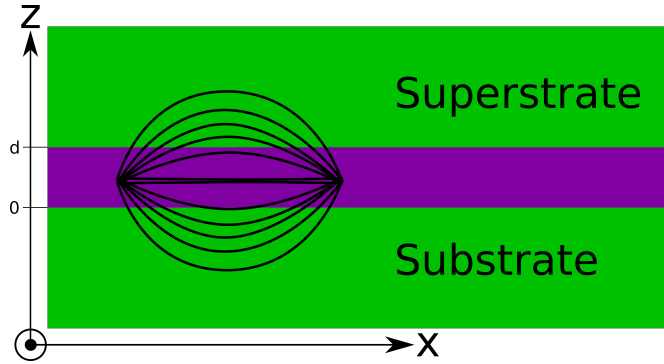


Figure 4.2: Illustration of encapsulated monolayer.

The screened potential W could be found from ab-initio calculations, however this is very computationally expensive. Instead an analytical approximation can be constructed starting Gauss' law from [22]

$$\nabla \cdot \mathbf{D} = e^2 \delta(\mathbf{r} - \mathbf{r}'). \quad (4.15)$$

As $\mathbf{D} = \epsilon_0 \epsilon \mathbf{E}$ and the electric field relates to the potential through $\mathbf{E} = -\nabla W$, these equations can be combined to give

$$\nabla \cdot [\epsilon(\mathbf{r})(-\nabla W(\mathbf{r}))] = \frac{e^2}{\epsilon_0} \delta(\mathbf{r} - \mathbf{r}'). \quad (4.16)$$

Writing the real-space potential in terms of the 2D Fourier transform

$$W(r, z, z') = \frac{1}{4\pi^2} \int w(z, z'; q) e^{i\mathbf{q} \cdot \mathbf{r}} d^2 q, \quad (4.17)$$

where \mathbf{q} and \mathbf{r} is the momentum and position in the xy-plane. This can be inserted into Eq. (4.16)

$$\frac{1}{4\pi^2} \int \left[-q^2 \epsilon(z) + \frac{d}{dz} \epsilon(z) \frac{d}{dz} \right] w(z, z'; q) e^{i\mathbf{q} \cdot \mathbf{r}} d^2 q = \frac{e^2}{\epsilon_0} \delta(\mathbf{r} - \mathbf{r}'). \quad (4.18)$$

The right-hand side can be represented in terms of its Fourier components as well and the inverse Fourier transform can be used on both sides, leading to the equation

$$\left[-q^2 \epsilon(z) + \frac{d}{dz} \epsilon(z) \frac{d}{dz} \right] w(z, z'; q) = \frac{e^2}{\epsilon_0} \delta(z - z'). \quad (4.19)$$

This equation can be solved in the geometry shown in Fig. 4.2 using the anzats

$$w(z, z'; q) = \frac{e^2}{2\epsilon_0 q} \begin{cases} C e^{-q|z-z'|} & z > d \\ \epsilon^{-1} e^{-q|z-z'|} + A e^{-q|z+z'|} + B e^{-q|2d-z-z'|} & 0 \leq z \leq d \\ D e^{-q|z-z'|} & z < 0 \end{cases} \quad (4.20)$$

In order to solve the equation using this ansatz, boundary conditions are required at both interfaces $z = \{0, d\}$. The boundary conditions are that the potential should be continuous and that the normal component of the \mathbf{D} -field should be continuous i.e

$$\begin{aligned} w(z^+, z'; q) &= w(z^-, z'; q) \\ \varepsilon^+ \frac{d}{dz} w(z^+, z'; q) &= \varepsilon^- \frac{d}{dz} w(z^-, z'; q). \end{aligned} \quad (4.21)$$

Using these boundary conditions four equations can be constructed and the unknown coefficients can be isolated leading to a solution when both z and z' are in the layer.

$$w(z, z'; q) = \frac{e^2 e^{-q|z+z'|} (\varepsilon - \varepsilon_b + (\varepsilon + \varepsilon_b) e^{2qz}) (\varepsilon + \varepsilon_a + (\varepsilon - \varepsilon_a) e^{2q(z-d)})}{2q\varepsilon\varepsilon_0 (\varepsilon + \varepsilon_b)(\varepsilon + \varepsilon_a) - (\varepsilon - \varepsilon_b)(\varepsilon - \varepsilon_a) e^{-2qd}}, \quad (4.22)$$

where ε , ε_a , ε_b refer to a homogeneous monolayer dielectric constant, superstrate dielectric constant, and substrate dielectric constant, respectively. $z_<$ and $z_>$ are the smallest and largest of z and z' . To simplify further the assumption $z = z' = d/2$ is used

$$w(q) = \frac{e^2}{2q\varepsilon_0} \frac{1}{\varepsilon \left(1 - \frac{\varepsilon - \varepsilon_a}{\varepsilon - \varepsilon_a + (\varepsilon + \varepsilon_a) e^{qd}} - \frac{\varepsilon - \varepsilon_b}{\varepsilon - \varepsilon_b + (\varepsilon + \varepsilon_b) e^{qd}} \right)}, \quad (4.23)$$

which amounts to assuming a truly 2D dimensional material. Comparing with the unscreened potential $v(q) = \frac{e^2}{2\varepsilon_0 q}$ the denominator of the second fraction can be identified as the effective dielectric function

$$\varepsilon(q) = \varepsilon \left(1 - \frac{\varepsilon - \varepsilon_a}{\varepsilon - \varepsilon_a + (\varepsilon + \varepsilon_a) e^{qd}} - \frac{\varepsilon - \varepsilon_b}{\varepsilon - \varepsilon_b + (\varepsilon + \varepsilon_b) e^{qd}} \right). \quad (4.24)$$

Taylor expanding to first order around $d = 0$ leads to

$$\varepsilon(q) = \frac{\varepsilon_a + \varepsilon_b}{2} + \left(\frac{\varepsilon - 1}{2} - \frac{\varepsilon_a^2 + \varepsilon_b^2 - 2\varepsilon}{4\varepsilon} \right) qd. \quad (4.25)$$

which can be rewritten as

$$\varepsilon(q) = \bar{\varepsilon} + r_0 q, \quad (4.26)$$

where $\bar{\varepsilon}$ is the average substrate and superstrate dielectric constants, and it has been assumed that the last term is small so that $r_0 = \frac{\varepsilon - 1}{2} d$ is the screening length of the material, which for MoS₂ is 44.3 Å [22]. The effective dielectric function for different substrate/superstrate combinations for MoS₂ shown in Fig. 4.3(a), and Fig. 4.3(b) shows how the real space potential is weakened by the screening.

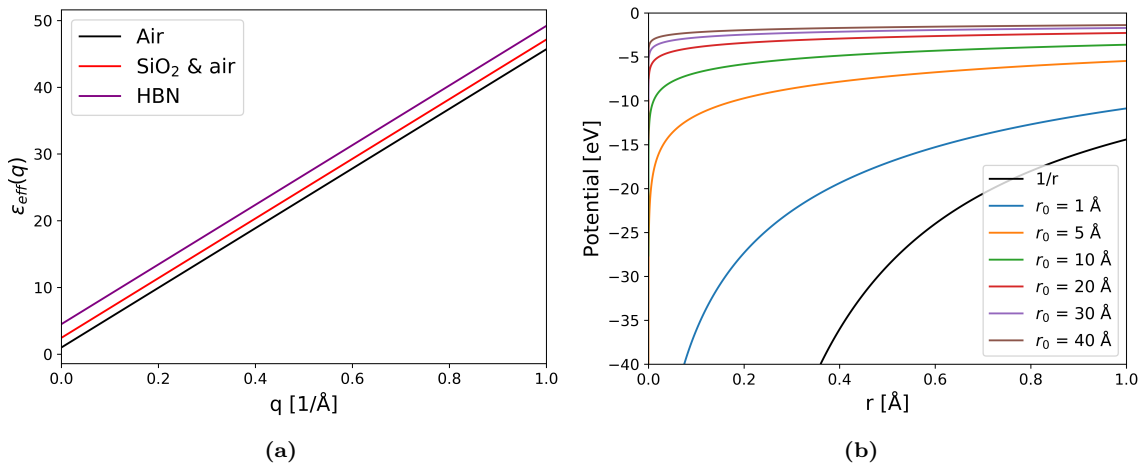


Figure 4.3: (a) Graphs of the linear screening function of MoS₂ for different substrate/superstrate combinations. (b) Screened real space potential at different r_0 .

4.4 Slow-rapid approximation

In order to continue, the screened potential from the previous should be inserted into Eq. (4.14), which results in matrix elements on the form of

$$V_{kl,ij} = \langle c_{l\mathbf{k}} v_{i\mathbf{k}'} | V | c_{j\mathbf{k}'} v_{k\mathbf{k}} \rangle = \iint \varphi_{c\mathbf{k}}^*(\mathbf{r}) \varphi_{v'\mathbf{k}'}^*(\mathbf{r}') W(\mathbf{r} - \mathbf{r}') \varphi_{c'\mathbf{k}'}(\mathbf{r}) \varphi_{v\mathbf{k}}(\mathbf{r}') d^3 r d^3 r'. \quad (4.27)$$

In principle the screened potential from Eq. (4.23) could be Fourier transformed and inserted, but an approximation can be made. The orbitals used to construct the Slater determinants are on the form

$$\varphi_{v\mathbf{k}}(\mathbf{r}) = \frac{1}{\sqrt{\Omega}} u_{v\mathbf{k}}(\mathbf{r}) e^{i\mathbf{k}\cdot\mathbf{r}}, \quad (4.28)$$

where $u_{v\mathbf{k}}$ is a lattice periodic function, which can be obtained from DFT calculations. The integral in Eq. (4.27) can be written as

$$V_{kl,ij} = \frac{1}{\Omega^2} \iint \underbrace{u_{c\mathbf{k}}^*(\mathbf{r}) u_{v'\mathbf{k}'}^*(\mathbf{r}') u_{c'\mathbf{k}'}(\mathbf{r}) u_{v\mathbf{k}}(\mathbf{r}')}_{\text{Rapid part}} \underbrace{W(\mathbf{r} - \mathbf{r}') e^{i(\mathbf{k}' - \mathbf{k})\cdot\mathbf{r}} e^{i(\mathbf{k} - \mathbf{k}')\cdot\mathbf{r}'}}_{\text{Slow part}} d^3 r d^3 r', \quad (4.29)$$

where the product of the lattice periodic parts has been identified as a rapidly varying function, and the product of the potential and the Bloch phases as a slowly varying function. This enables the integral to be approximated as the product of the average of the rapid part and the integral of the slow part,

$$V_{kl,ij} \approx \frac{1}{\Omega^2 \Omega_{uc}^2} \iint_{uc} u_{c\mathbf{k}}^*(\mathbf{r}) u_{v'\mathbf{k}'}^*(\mathbf{r}') u_{c'\mathbf{k}'}(\mathbf{r}) u_{v\mathbf{k}}(\mathbf{r}') d^3 r d^3 r' \iint W(\mathbf{r} - \mathbf{r}') e^{i(\mathbf{k}' - \mathbf{k})\cdot\mathbf{r}} e^{i(\mathbf{k} - \mathbf{k}')\cdot\mathbf{r}'} d^3 r d^3 r', \quad (4.30)$$

where the periodicity of the rapid part has been used to limit the integral to the unit cell. Thus the rapid integrals can be calculated as

$$\begin{aligned} I_{v'\mathbf{k}'v\mathbf{k}} &= \frac{1}{\Omega_{uc}} \int_{uc} u_{v'\mathbf{k}'}^*(\mathbf{r}') u_{v\mathbf{k}}(\mathbf{r}') d^3 r' \\ I_{c\mathbf{k}c'\mathbf{k}'} &= \frac{1}{\Omega_{uc}} \int_{uc} u_{c\mathbf{k}}^*(\mathbf{r}) u_{c'\mathbf{k}'}(\mathbf{r}) d^3 r. \end{aligned} \quad (4.31)$$

Returning to the slow part and introducing $\mathbf{q} = \mathbf{k} - \mathbf{k}'$ allows the slow integral to be written as

$$S_{\mathbf{k}\mathbf{k}'} = \frac{1}{\Omega^2} \iint W(\mathbf{r} - \mathbf{r}') e^{-i\mathbf{q}\cdot(\mathbf{r}-\mathbf{r}')} d^3 r d^3 r' = \frac{1}{\Omega} \int W(\mathbf{r}) e^{-i\mathbf{q}\cdot\mathbf{r}} d^3 r, \quad (4.32)$$

which can be identified as the Fourier transform of the screened potential which gives the screened potential in reciprocal space, which was approximated in the previous section. The Coulomb matrix elements can then finally be written as

$$V_{kl,ij} \approx \frac{1}{\Omega} I_{v'\mathbf{k}'v\mathbf{k}} I_{c\mathbf{k}c'\mathbf{k}'} w(\mathbf{q}). \quad (4.33)$$

The exchange matrix elements are zero within this approximation. Assuming the lattice periodic u functions are known in a basis of plane waves

$$u_n(\mathbf{r}) = \sum_{\mathbf{G}} c_n(\mathbf{G}) e^{i\mathbf{G}\cdot\mathbf{r}}, \quad (4.34)$$

where n is a composite band and \mathbf{k} -index. With this notation all the rapid I integrals can be evaluated as

$$I_{n\mathbf{k}n'\mathbf{k}'} = \frac{1}{\Omega_{uc}} \sum_{\mathbf{G}} \sum_{\mathbf{G}'} c_{n\mathbf{k}}(\mathbf{G}) c_{n'\mathbf{k}'}^*(\mathbf{G}') \int_{uc} e^{i(\mathbf{G}-\mathbf{G}')\cdot\mathbf{r}} d^3 r = \sum_{\mathbf{G}} c_{n\mathbf{k}}(\mathbf{G}) c_{n'\mathbf{k}'}^*(\mathbf{G}), \quad (4.35)$$

where orthonormality of the plane waves was used for the last equality.

4.5 Wannier approximation

At this point the framework has been developed enough to become useful. The difficulty when applying the framework at this point is calculating the $I_{n\mathbf{k}n'\mathbf{k}'}$ factors. Within the Wannier approximation these are approximated by $I_{n\mathbf{k}n'\mathbf{k}'} = \delta_{n,n'}$, which in effect decouples the bands in the Coulomb terms and ignores the exchange terms in the BSE. This is exact for $\mathbf{k} = \mathbf{k}'$ and will thus be an okay approximation if the \mathbf{k} -dependence of these integrals is not too large. Furthermore the quasiparticle energies that enter the BSE matrix are approximated within the effective mass approximation so that

$$E_{cv}(\mathbf{k}) = E_g + \frac{\hbar^2 \mathbf{k}^2}{2m_{eh}}, \quad (4.36)$$

where m_{eh} is the effective electron-hole mass [22]. In principle this allows the problem to be transformed to real-space rather than k-space, but as a test of the numerical implementation it is kept in reciprocal space. Figure 4.4 shows the binding energy of the 1s exciton in MoS₂ using $m_{eh} = 0.28$ [22]. For a suspended MoS₂ layer it can be seen that a binding energy of 0.51 eV is obtained in good agreement with 0.47 eV obtained by [38]. It is clear from the approximations above that the Wannier approximation will always overestimate the Coulomb attraction due to approximating $I_{n\mathbf{k}n'\mathbf{k}'}$ as a delta function, which leads to a larger binding energy than would be obtained by a calculation where $I_{n\mathbf{k}n'\mathbf{k}'}$ is explicitly calculated as these factors will always be less than 1 for $\mathbf{k} \neq \mathbf{k}'$. The k-grid consists of 100x100 k-points within a square with width/height equal to the length of the in-plane reciprocal lattice vectors centered around the \mathbf{K} special point.

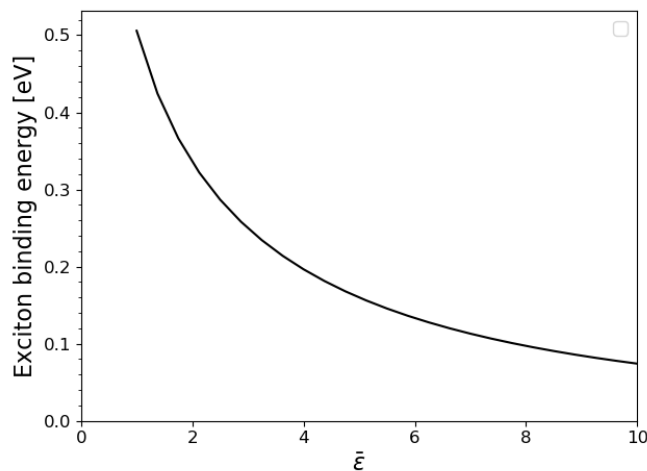


Figure 4.4: Exciton binding energy in MoS₂ calculated in the Wannier approximation in k-space.

4.6 Two-band approximation

The basis in Eq. (4.1) included Slater determinants between an unspecified amount of conduction and valence bands. Limiting the basis to Slater determinants where the highest valence orbital has been changed with the lowest conduction orbital leads to

$$|S\rangle = \sum_{\mathbf{k}} \alpha_{\mathbf{k}} |v_{\mathbf{k}} \rightarrow c_{\mathbf{k}}\rangle. \quad (4.37)$$

In this basis the Hamiltonian matrix elements of Eq. (4.14) can be formulated as

$$H_{k,k'} = [E_c(\mathbf{k}) - E_v(\mathbf{k})] \delta_{\mathbf{k}\mathbf{k}'} - \frac{1}{\Omega} I_{c\mathbf{k}c\mathbf{k}'} I_{v\mathbf{k}v\mathbf{k}'} w(\mathbf{k} - \mathbf{k}'), \quad (4.38)$$

where it has been utilized that both of the band delta functions are unity. With the matrix elements formulated in this way Eq. (4.5) can be written as $\sum_{\mathbf{k}'} H_{\mathbf{k}\mathbf{k}'} \alpha_{\mathbf{k}'} = E \alpha_{\mathbf{k}}$ or

$$E_{cv}(\mathbf{k}) \alpha_{\mathbf{k}} - \frac{1}{\Omega} \sum_{\mathbf{k}'} I_{c\mathbf{k}c\mathbf{k}'} I_{v\mathbf{k}v\mathbf{k}'} w(\mathbf{k} - \mathbf{k}') \alpha_{\mathbf{k}'} = E \alpha_{\mathbf{k}}. \quad (4.39)$$

Converting the sum over \mathbf{k}' to an integral using $\sum_{\mathbf{k}'} \rightarrow \frac{L}{2\pi} \int d\mathbf{k}$ leads to

$$E_{cv}(\mathbf{k}) \alpha(\mathbf{k}) - \frac{1}{4\pi^2} \int I_{c\mathbf{k}c\mathbf{k}'} I_{v\mathbf{k}v\mathbf{k}'} w(\mathbf{k} - \mathbf{k}') \alpha(\mathbf{k}') d^2k' = E \alpha(\mathbf{k}), \quad (4.40)$$

where the integral goes over the entire Brillouin zone. In order to solve the problem numerically the equations needs to be discretized, which is easier on a square grid than on the usual hexagonal Brillouin zone. The rectangular integration area must have the same area as the hexagonal Brillouin zone, and it must be shaped so that it is possible to fold and cut it into the hexagonal Brillouin zone. The width and height of the new Brillouin zone is denoted L_x and L_y respectively.

L_x is taken to be the width of the hexagonal Brillouin zone from the \mathbf{M} special point to the $-\mathbf{M}$ special point. L_y can then be found by requiring that the area of the rectangular integration area is the same as the hexagonal Brillouin zone. The area of the irreducible Brillouin zone is

$$A_{IBZ} = \frac{1}{2} K_x K_y, \quad (4.41)$$

with K_x , and K_y being the x-y components of the \mathbf{K} special point which is given by

$$\mathbf{K} = \frac{2\pi}{\sqrt{3}a} \left[1, \frac{1}{\sqrt{3}} \right]. \quad (4.42)$$

L_x will be $2 \cdot K_x$, thus L_y is found by

$$A_{BZ} = L_y \cdot L_x = 12 \cdot A_{IBZ} = 6K_x K_y, \quad (4.43)$$

as $L_x = 2 \cdot K_x$

$$L_y = 3K_y = \frac{2\pi}{a}. \quad (4.44)$$

This rectangular integration area can then be translated by some vector in reciprocal space. In Fig. 4.5 the rectangular integration area is shown, translated so that the lower left corner is placed in $[-\frac{1}{4}L_y, -\frac{1}{2}L_y]$.

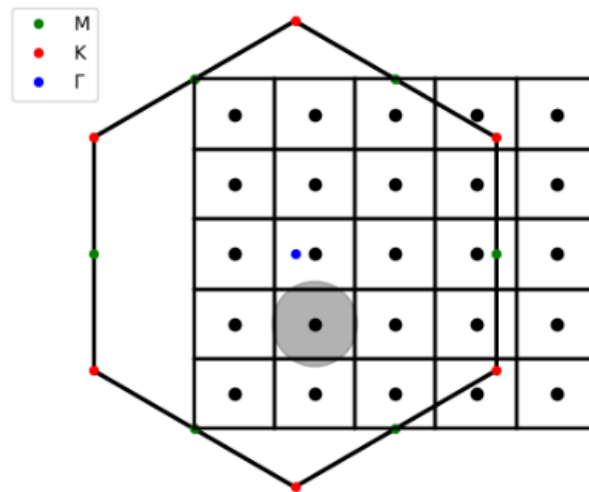


Figure 4.5: Illustration showing the new rectangular Brillouin zone. The gray circle indicates that the k-integration performed in the diagonal of the Hamiltonian is done in polar coordinates.

The integral can of course be written as a sum of integrals over each rectangular element of the grid. Each of these integrals are then approximated by assuming that the function is constant within the rectangle equal to the value at the center. This amount to rewriting Eq. (4.40) as

$$E_{cv\mathbf{k}}\alpha_{\mathbf{k}} - \frac{1}{4\pi^2} \sum_{\mathbf{k}'} I_{c\mathbf{k}c\mathbf{k}'} I_{v\mathbf{k}v\mathbf{k}'} w(\mathbf{k} - \mathbf{k}') \alpha_{\mathbf{k}'} \Delta k_x \Delta k_y = E \alpha_{\mathbf{k}}. \quad (4.45)$$

The $\mathbf{k} = \mathbf{k}'$ term in the discretized sum is problematic as the potential is divergent. This can, however, be remedied by converting to polar coordinates, the integral over this element is then given by

$$-\frac{1}{4\pi^2} \int_0^{2\pi} \int_0^a w(q) q \, dq d\theta = -\frac{e^2}{4\pi\epsilon_0} \int_0^a \frac{q}{q(r_0 q + \bar{\epsilon})} \, dq = -\frac{e^2}{4\pi r_0 \epsilon_0} \ln \left(\frac{ar_0 + \bar{\epsilon}}{\bar{\epsilon}} \right). \quad (4.46)$$

Finally, the entries of the Hamiltonian matrix can be written as

$$H_{\mathbf{k}\mathbf{k}'} = \begin{cases} E_{cv\mathbf{k}} - \frac{e^2}{4\pi r_0 \epsilon_0} \ln \left(\frac{ar_0 + \bar{\epsilon}}{\bar{\epsilon}} \right) & \mathbf{k} = \mathbf{k}' \\ -\frac{1}{4\pi^2} I_{c\mathbf{k}c\mathbf{k}'} I_{v\mathbf{k}v\mathbf{k}'} w(\mathbf{k} - \mathbf{k}') \Delta k_x \Delta k_y & \mathbf{k} \neq \mathbf{k}'. \end{cases} \quad (4.47)$$

4.7 Optical properties of excitons

The optical properties can be calculated by the many-body version of Eq. (2.35), in which the single-particle momentum matrix elements has been replaced by many-body momentum matrix elements using the operator

$$\hat{P} = \sum_n^{2N} \hat{p}_x, \quad (4.48)$$

and differences in band energies replaced by exciton energies, leading to

$$\chi(\omega) = \frac{2e^2 \hbar^2}{\epsilon_0 m^2 \Omega} \sum_S \frac{|\langle 0 | \hat{P} | S \rangle|^2}{E_s [E_s^2 - \hbar^2 (\omega + i\Gamma)^2]}. \quad (4.49)$$

The many-body momentum operator is a sum of single-body operators and there is one difference between the ground state and each of the basis states, thus the momentum matrix elements become a weighted sum as

$$\langle 0 | \hat{P} | S \rangle = \sqrt{2} \sum_{\mathbf{k}} \alpha_{\mathbf{k}} \langle v_{\mathbf{k}} | \hat{p}_{xy} | c_{\mathbf{k}} \rangle = \sqrt{2} \sum_{\mathbf{k}} \alpha_{\mathbf{k}} \hat{p}_{cv,\mathbf{k}}, \quad (4.50)$$

where spin degeneracy has been assumed. The single particle momentum in a basis of plane-waves can readily be calculated from Eq. (2.51). The exciton wavefunction $\alpha_{\mathbf{k}}$ is normalized as

$$\sum_{\mathbf{k}} |\alpha_{\mathbf{k}}|^2 = 1, \quad (4.51)$$

However, by inserting $\tilde{\alpha}_{\mathbf{k}}$, which is normalized as

$$\int |\tilde{\alpha}_{\mathbf{k}}|^2 d^2 k = \frac{4\pi^2}{A} \sum_{\mathbf{k}} \tilde{\alpha}_{\mathbf{k}} = 1, \quad (4.52)$$

so that $|\alpha_{\mathbf{k}}|^2 = \frac{4\pi^2}{A} |\tilde{\alpha}_{\mathbf{k}}|^2$, the equation becomes

$$\langle 0 | \hat{P} | S \rangle = \sqrt{2} \sqrt{\frac{4\pi^2}{A}} \sum_{\mathbf{k}} \tilde{\alpha}_{\mathbf{k}} \hat{p}_{cv,\mathbf{k}}. \quad (4.53)$$

Converting the sum over \mathbf{k} to an integral and discretizing leads to

$$\langle 0 | \hat{P} | S \rangle = \sqrt{2} \sqrt{\frac{4\pi^2}{A}} \frac{A}{4\pi^2} \int \tilde{\alpha}_{\mathbf{k}} p_{cv}(\mathbf{k}) \, d^2 k = \sqrt{2} \sqrt{\frac{A}{4\pi^2}} \sum_{\mathbf{k}} \tilde{\alpha}_{\mathbf{k}} p_{cv\mathbf{k}} \Delta k_x \Delta k_y. \quad (4.54)$$

Denoting the sum over \mathbf{k} as P and taking the absolute square leads to

$$|\langle 0|\hat{P}|S\rangle|^2 = \frac{2A}{4\pi^2}|P_S|^2. \quad (4.55)$$

Finally the susceptibility can be calculated as

$$\chi(w) = \frac{2A}{4\pi^2} \frac{2e^2\hbar^2}{\varepsilon_0 m^2 \Omega} \sum_S \frac{|P_S|^2}{E_S [E_S^2 - \hbar^2(w + i\Gamma)^2]}, \quad (4.56)$$

and the 2D susceptibility as

$$\chi_{2d}(w) = \frac{e^2\hbar^2}{\pi^2\varepsilon_0 m^2} \sum_S \frac{|P_S|^2}{E_S [E_S^2 - \hbar^2(w + i\Gamma)^2]}. \quad (4.57)$$

As matrix elements are calculated from DFT instead of G0W0, the momentum matrix elements should be renormalized such that the magnitude of each transition is conserved, which is achieved by [39]

$$\langle v_{\mathbf{k}}|\hat{p}|c_{\mathbf{k}}\rangle = \langle v_{\mathbf{k}}|\hat{p}|c_{\mathbf{k}}\rangle^{DFT} \frac{E_{cv}^{GW}(\mathbf{k})}{E_{cv}^{DFT}(\mathbf{k})}. \quad (4.58)$$

The BSE matrix couples different \mathbf{k} states through the Coulomb interaction. If this coupling is removed, the BSE matrix becomes a diagonal with the differences in band energies as entries. Without coupling, the same spectrum as presented in Chap. 2 should be obtained, but be shifted in energy by the scissor operator. Fig. 4.6 shows the spectrum obtained for MoS₂ from both the BSE equation without coupling and the one from independent particle framework discussed previously, both using a lattice constant of 3.18 Å. The differences in the two spectra are due to the different integration/interpolation schemes employed in the calculations. Comparing to Fig. 2.5(a) it is seen that good agreement is obtained. One difference is that in Fig. 2.5(a) the maximum conductivity for the $v_1 \rightarrow c_1$ transition was the first peak, but now it is the second. These differences can be explained by differences in numerical implementation, i.e Fig. 2.5(a) was calculated using the improved triangle method compared to the discretization/interpolation scheme used for the BSE and differences in the momentum matrix elements caused by using a different lattice constant for the DFT calculation Fig. 4.6 is based on.

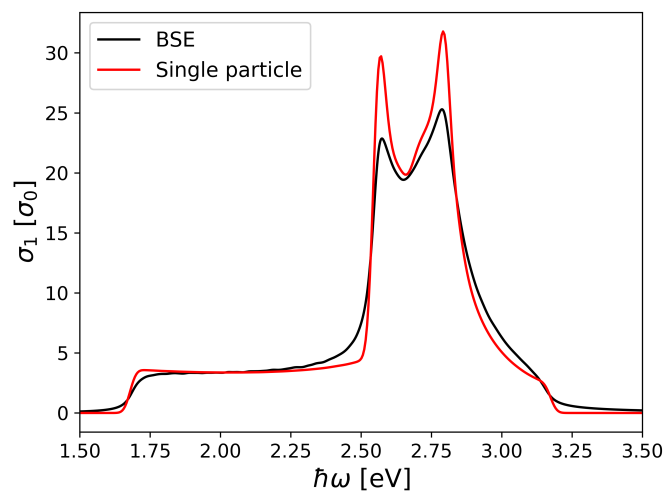


Figure 4.6: Optical conductivity for the $c_1 \rightarrow v_1$ transition of MoS₂ calculated from Eqs. (4.47) & (4.57), when ignoring the Coulomb interaction.

4.8 Numerical implementation

The $I_{ckck'}$ and $I_{vkvk'}$ integrals are given by Eq. (4.35), however, as it is impossible to include plane-waves with all \mathbf{G} -vectors in the basis of the underlying DFT calculation, truncation of the basis set is required. In GPAW, and most other plane-wave DFT packages, this truncation is achieved by limiting the kinetic energy of the plane-waves to some value, commonly referred to as the cut-off energy. The kinetic energy of each basis function does not depend solely on \mathbf{G} but also on the \mathbf{k} -point, thus different \mathbf{k} -points will have different bases, which makes evaluation of Eq. (4.35) difficult. To deal with this problem only the \mathbf{G} -vectors that are common among all \mathbf{k} -points are used in the evaluation of these integrals. This approach only works if the coefficients that are not used are small, or in other terms that the overlap integral of $u_k(\mathbf{r})$ using only the common \mathbf{G} -vectors is close to 1 when $u_k(\mathbf{r})$ is normalized with respect to the basis functions in the original calculation. It was found that this overlap integral differs from 1 in the order of 10^{-7} .

The amount of Slater determinants required to converge exciton energies and wave functions can be large, i.e. Eq. (4.37) should be evaluated on a fine \mathbf{k} -point grid on the order of 100×100 \mathbf{k} -points. A DFT calculation of this size is computationally expensive, and functions such as $E_{cv}(\mathbf{k})$ are smooth and can as such be interpolated from a DFT calculation with a coarser \mathbf{k} -point grid. A convenient interpolation scheme can be crafted by triangulating the coarse mesh and apply barycentric linear interpolation in each triangle. Using Fig. 4.7 the interpolation of a function $F(\mathbf{k})$, which is explicitly calculated at the corners can be found from

$$F(\mathbf{k}) = \frac{A_1}{A} F(\mathbf{k}_1) + \frac{A_2}{A} F(\mathbf{k}_2) + \frac{A_3}{A} F(\mathbf{k}_3), \quad (4.59)$$

where A_1 refers to the area of the region in the triangle defined by the three \mathbf{k} -points \mathbf{k} , \mathbf{k}_2 , \mathbf{k}_3 and A is the total area. This interpolation scheme is employed where DFT calculations are done on Monkhorst-Pack grids with \mathbf{k} -points added on the edges of the rectangular BZ to ensure that extrapolation is never necessary, and the important quantities are calculated on rectangular grids that do not have time-reversal symmetry, to reduce symmetry in the basis set entering Eq. (4.37).

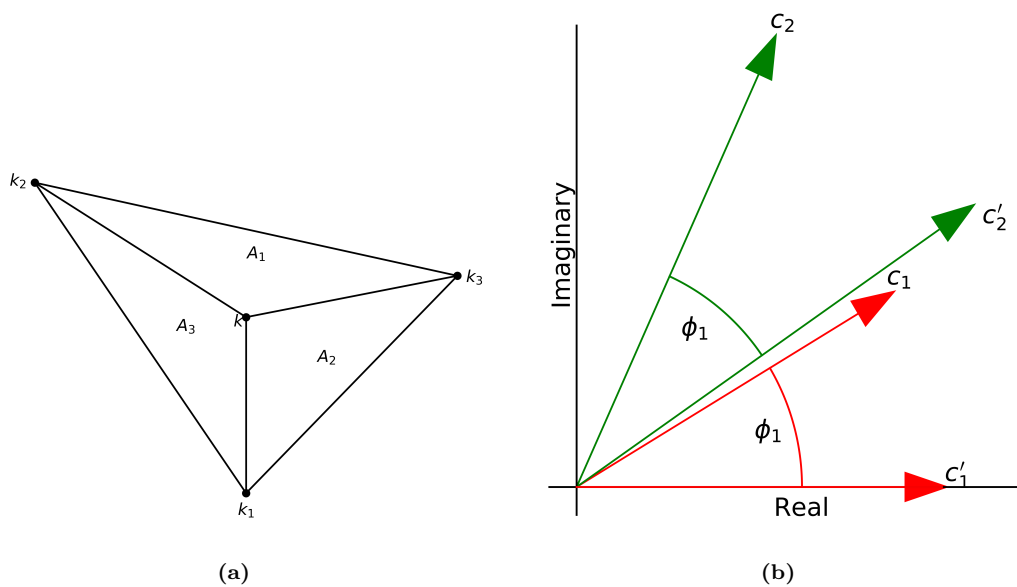


Figure 4.7: (a) Interpolation scheme employed for all required quantities. (b) The phase of c_1 is removed so that c_1 becomes c'_1 which is entirely real, c_2 is the coefficient of a different basis function for the same \mathbf{k} and c'_2 has the phase adjusted by ϕ_1

One important issue arises when interpolating complex quantities such as the basis coefficients of the Kohn-Sham orbitals. The coefficients have an arbitrary k -point dependent phase which must be removed, as otherwise interpolation is impossible. This is done by requiring that the coefficient corresponding to a specific \mathbf{G} that is nonzero and large is entirely real and that the phase of all other coefficients are defined in relation to that. As an example, consider that the coefficient of \mathbf{G}_n are chosen to be real for all k , then the \mathbf{G}_n coefficient of \mathbf{k}_1 can be written as $C_{\mathbf{k}_1}(\mathbf{G}_1) = |C_{\mathbf{k}_1}| \exp(i\phi_{n1})$ then all coefficients of \mathbf{k}_1 are multiplied by $\exp(-i\phi_{n1})$. For \mathbf{k}_2 all coefficients are multiplied by $\exp(-i\phi_{n2})$ and so on. This phase convention is illustrated in Fig. 4.7(b). The difference between adjusting the phase and not adjusting the phase is shown in Fig. 4.8, which clearly illustrates that interpolation without adjusting the phase would be a bad idea. For momentum matrix elements the PAW correction has been neglected as it breaks the phase convention and has been found to be a small correction for the two bands in question.

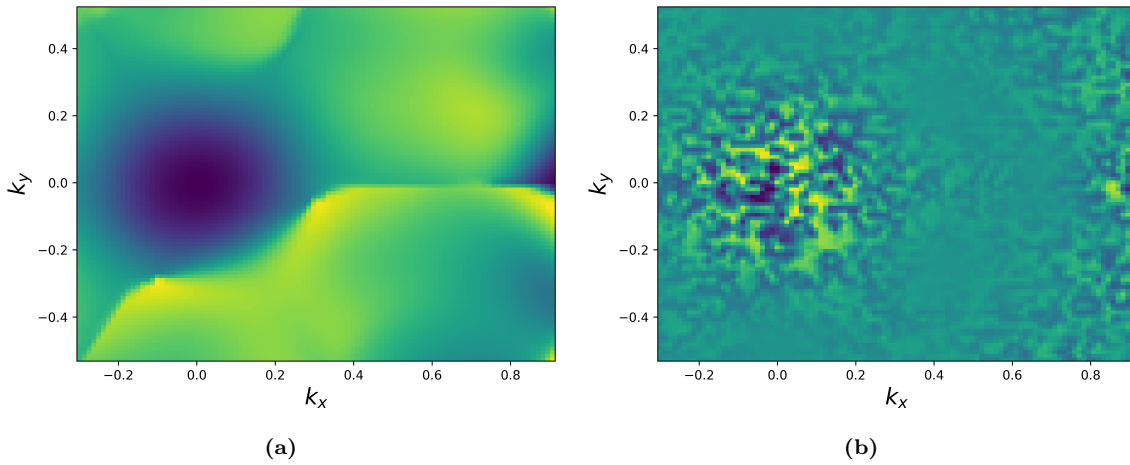


Figure 4.8: Pseudocolor plots of the real part of the $\mathbf{G} = \mathbf{0}$ coefficient on a 100x100 grid interpolated from 55x55 Monkhorst-Pack grid, (a) with phase correction, (b) without phase correction.

In regions where the surfaces that are being interpolated are not actually linear, interpolation will introduce an error. A quantification of this error is the overlap of the interpolated lattice periodic part of the orbitals $u_n(\mathbf{r})$ which should equal 1. Fig. 4.9 shows the average overlap after interpolating to a 100x100 grid from a range of Monkhorst-Pack grids. It is clear that as the grid size increases the interpolation error decreases and asymptotically approaches zero. The small non-monotonic behaviour is due to differing placements of the grid points causing the change over triangular interpolation regions to be better approximated by a linear function. Considering this error the remaining calculations are based on 50x50 Monkhorst-Pack grid DFT calculations.

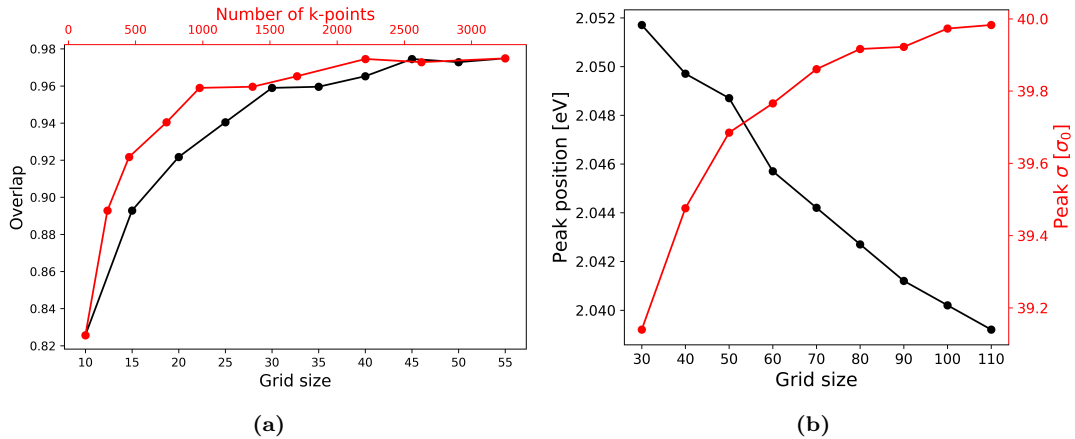


Figure 4.9: (a) Average overlap of interpolated 100x100 grid from a range of Monkhorst-Pack grids as a function of grid size and total number of k-points. (b) The position of the 1s exciton conductivity peak and the conductivity at the peak position as functions of grid size.

To ensure that enough states were included in Eq. (4.37) the optical conductivity was calculated on grids ranging from 30x30 to 110x110. The position of the conductivity peak and the value at the peak corresponding to the 1s exciton is plotted in Fig. 4.9 as calculated from the different grids. The position of the peak decreases as more states are included in the calculation, while the maximum conductivity of the 1s exciton changes by $0.04 \sigma_0$ between a 80x80 to a 110x110 grid calculation. The remaining results are calculated on 100x100 grids unless otherwise specified.

4.9 Substrate effects

The framework developed thus far allows for including the substrate and the superstrate dielectric constants through the average between the two $\bar{\epsilon}$, which when increased will further screen the electron-hole interaction and lower the exciton binding energy. Exciton energies E_s are calculated with the zero point at the top of the valence band, and thus the exciton binding energy is given by

$$E_{binding} = E_{g,GW} - E_s, \quad (4.60)$$

where $E_{g,GW}$ is the fundamental band gap. The exciton binding energy of the lowest exciton in MoS₂ with varying dielectric environments is shown in Fig. 4.10(a). The same tendency can be observed from plots of the optical conductivity in Fig. 4.10(b), where the resonance of the A-exciton moves to higher energies and becomes weaker. It has been shown that changing the dielectric environment has very little effect on the position of the lowest exciton peak, but rather changes the GW band gap, which is not taken into account in this calculation [40].

The decrease in binding energy can be explained through increased screening, but the decrease in the strength of the resonance must be caused by the exciton being composed of states that are less optically active.

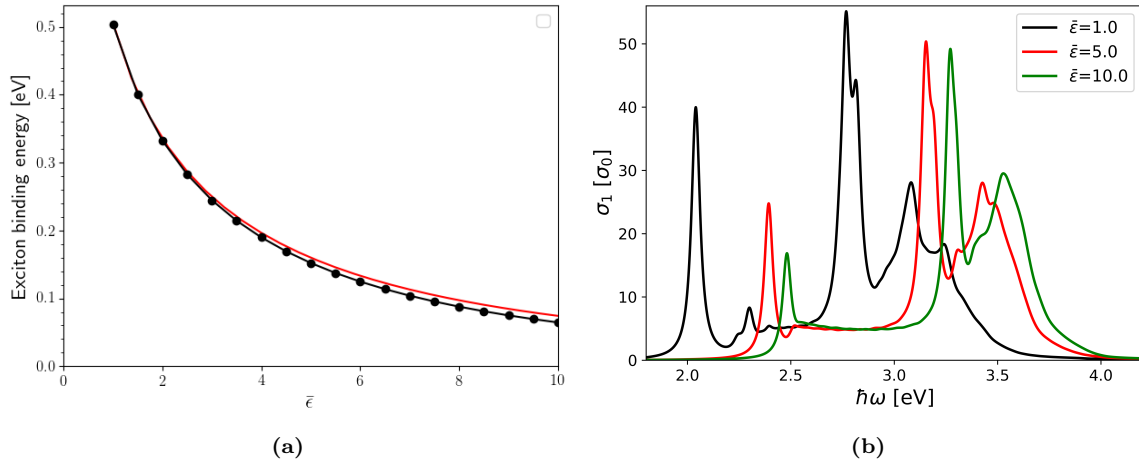


Figure 4.10: (a) Binding energy of the lowest energy exciton in MoS₂ for different dielectric environments from BSE and Wannier calculations. (b) Optical conductivity of MoS₂ for $\bar{\epsilon} = 1, 5, 10$.

Fig. 4.11 shows color plots of the exciton wave function in reciprocal space of the lowest lying state with an average substrate dielectric function of 1 and of 5. In both cases the regions around the two \mathbf{K} special points are the dominant contributors to the exciton wave function, however, as the screening increases the wave function becomes more localized in k-space.

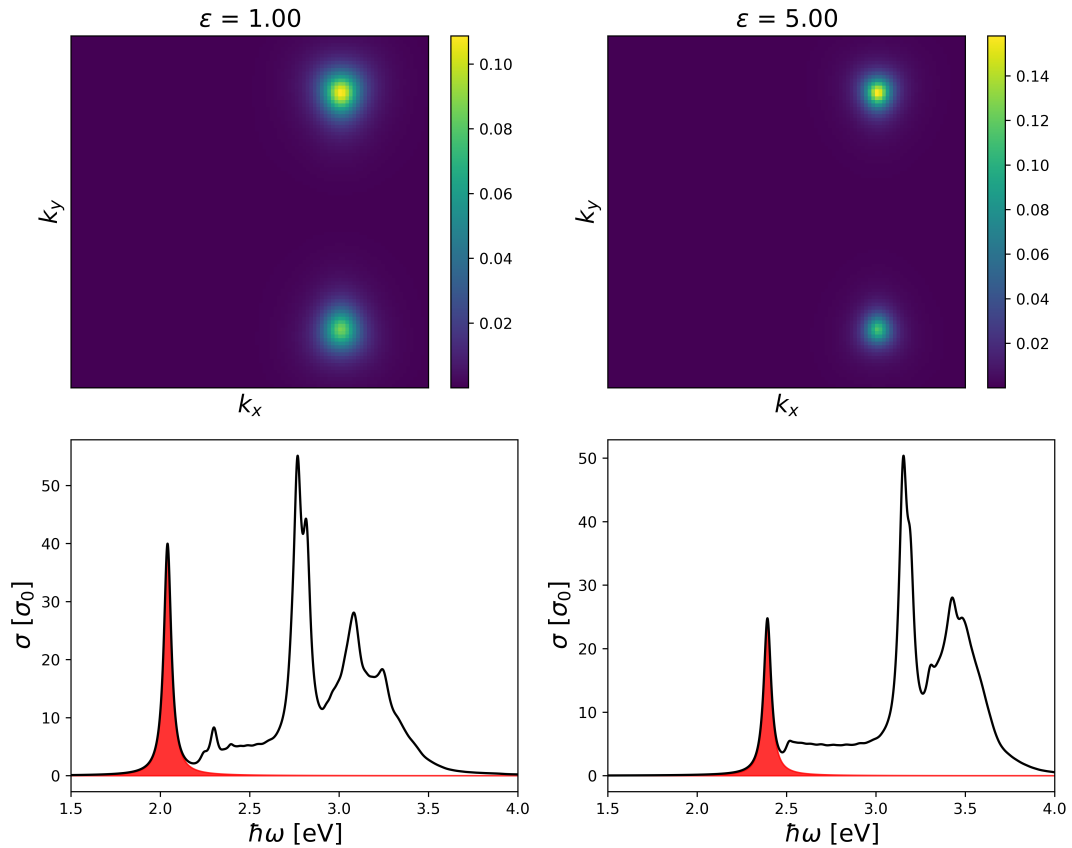


Figure 4.11: Absolute value of the expansion coefficients of the lowest energy exciton for $\epsilon = 1$ and $\epsilon = 5$ and the corresponding optical conductivity spectra. The colored areas in the spectra are the contributions of this exciton to the optical conductivity

4.10 Spin-orbit interaction

It is well known that the spin-orbit interaction splits the highest valence band near the \mathbf{K} special point, as shown in Fig. 4.12, where the spin-orbit coupling at \mathbf{K} is found to be $\Delta_E = 0.151$ eV, which is in good agreement with [38]. Experimental measurements find that two distinct exciton peaks are measured in MoS_2 , which is caused by splitting of the valence band [41, 42]. These effects could be included in the BSE calculation by extending the framework to include more than one pair of bands and using DFT wave functions where spin-orbit coupling has been included, however, the inclusion of more bands makes the framework more complicated and much more computationally expensive. Instead the effect can be included phenomenologically by shifting the energy of the two lowest lying exciton energies by $\pm\Delta_E/2$ and normalizing the momentum matrix elements of these four new states according to

$$|P_S|^2 \rightarrow \frac{1}{2} \frac{E_s \pm \frac{1}{2}\Delta_E}{E_s} |P_S|^2. \quad (4.61)$$

The one half factor removes the spin degeneracy factor included in Eq. (4.57) and the second fraction scales the conductivity so the magnitude of the individual peaks is conserved independently of the size of Δ_E . This is done for the two lowest lying states to ensure that the same optical conductivity is calculated independently of whether \hat{p}_x or \hat{p}_y is used, as one exciton couples to \hat{p}_x and the other \hat{p}_y with nearly identical energies. The result of this phenomenological model is shown in Fig. 4.12(b).

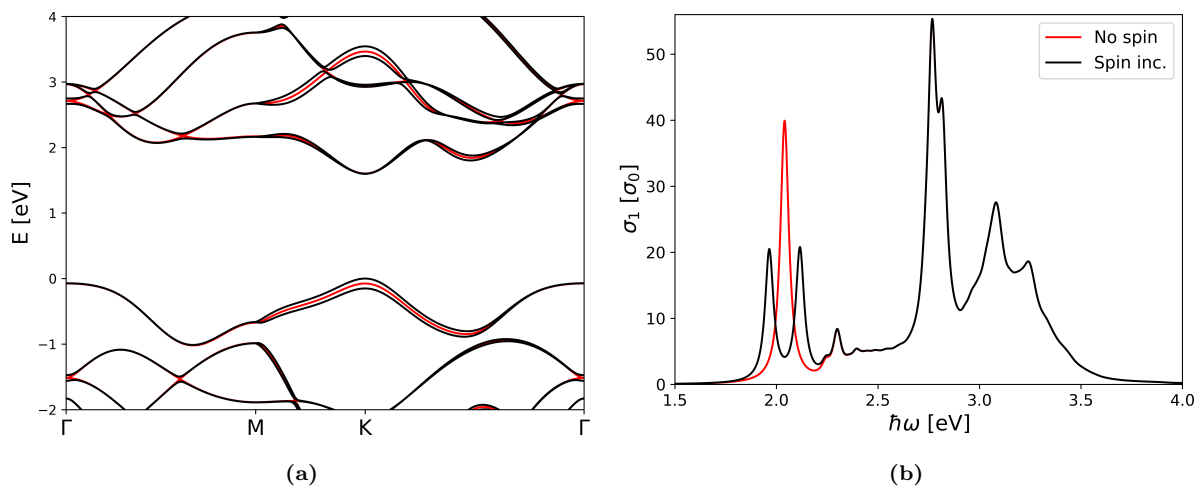


Figure 4.12: (a) MoS_2 DFT band structures including spin-orbit coupling (black lines) and without spin-orbit coupling (red lines). (b) Optical conductivity of MoS_2 as calculated within the BSE framework with and without phenomenological inclusion of spin-orbit coupling.

4.11 Coulomb and exchange integrals

So far the slow-rapid approximation has been used, which neglects exchange and underestimates the Coulomb interaction. The Coulomb and exchange integrals can be written in general as

$$E_{\alpha\beta\gamma\delta} = \iint \phi_{\alpha\mathbf{k}_\alpha}^*(\mathbf{r})\phi_{\beta\mathbf{k}_\beta}(\mathbf{r})W(\mathbf{r},\mathbf{r}')\phi_{\gamma\mathbf{k}_\gamma}^*(\mathbf{r}')\phi_{\delta\mathbf{k}_\delta}(\mathbf{r}')d^3rd^3r', \quad (4.62)$$

with $\phi(\mathbf{r})$ being single particle orbitals, and $W(\mathbf{r},\mathbf{r}')$ being either the screened or unscreened potential. The single particle orbitals are Bloch waves, where the product of the lattice periodic functions $u(\mathbf{r})$ of two different orbitals are expanded in Fourier as

$$u_{\alpha\mathbf{k}_\alpha}^*(\mathbf{r})u_{\beta\mathbf{k}_\beta}(\mathbf{r}) = \sum_{\mathbf{G}_{\alpha\beta}} I_{\alpha\beta}(\mathbf{G}_{\alpha\beta})e^{i\mathbf{G}_{\alpha\beta}\cdot\mathbf{r}}, \quad (4.63)$$

with the other orbitals expanded similarly. The potential W is also expanded, however, only in 2D Fourier components as

$$W(\mathbf{r},\mathbf{r}') = \frac{1}{\Omega} \sum_{\mathbf{p}_\parallel, \mathbf{G}_\parallel} W(\mathbf{p}_\parallel + \mathbf{G}_\parallel)e^{i(\mathbf{p}_\parallel + \mathbf{G}_\parallel)\cdot(\mathbf{r}-\mathbf{r}')}, \quad (4.64)$$

with \mathbf{p}_\parallel being limited to the first Brillouin zone. The integrals can now be written as

$$\frac{1}{\Omega} \sum_{\mathbf{p}_\parallel, \mathbf{G}_\parallel, \mathbf{G}_{\alpha\beta}, \mathbf{G}_{\gamma\delta}} w(\mathbf{p}_\parallel + \mathbf{G}_\parallel)I_{\alpha\beta}(\mathbf{G}_{\alpha\beta})I_{\gamma\delta}(\mathbf{G}_{\gamma\delta}) \iint e^{i((\mathbf{k}_\beta - \mathbf{k}_\alpha) + \mathbf{G}_{\alpha\beta} + \mathbf{p}_\parallel + \mathbf{G}_\parallel)\cdot\mathbf{r}} e^{i((\mathbf{k}_\delta - \mathbf{k}_\gamma) + \mathbf{G}_{\gamma\delta} - \mathbf{p}_\parallel - \mathbf{G}_\parallel)\cdot\mathbf{r}'} d^3rd^3r'. \quad (4.65)$$

The z-part of the integrals demand that $\mathbf{G}_{\alpha\beta}$ and $\mathbf{G}_{\gamma\delta}$ both have a zero z-component. The only surviving terms of the sum are those that fulfill both of the following conditions

$$\begin{aligned} (\mathbf{k}_\beta - \mathbf{k}_\alpha) + \mathbf{G}_{\alpha\beta} + \mathbf{p}_\parallel + \mathbf{G}_\parallel &= 0 \\ (\mathbf{k}_\delta - \mathbf{k}_\gamma) + \mathbf{G}_{\gamma\delta} - \mathbf{p}_\parallel - \mathbf{G}_\parallel &= 0. \end{aligned} \quad (4.66)$$

As \mathbf{p}_\parallel is limited to the first Brillouin zone it can only cancel with the \mathbf{k} 's, thus

$$\begin{aligned} (\mathbf{k}_\beta - \mathbf{k}_\alpha) &= \mathbf{p}_\parallel = (\mathbf{k}_\delta - \mathbf{k}_\gamma) = \mathbf{q} \\ \mathbf{G}_{\alpha\beta} &= -\mathbf{G}_\parallel \\ \mathbf{G}_{\gamma\delta} &= \mathbf{G}_\parallel. \end{aligned} \quad (4.67)$$

Thus the integrals for exchange and Coulomb can both be written as

$$E_{\mathbf{q}} = \Omega \sum_{\mathbf{G}} w(\mathbf{q} + \mathbf{G}_\parallel)I_{\alpha\beta}(-\mathbf{G}_\parallel)I_{\gamma\delta}(\mathbf{G}_\parallel). \quad (4.68)$$

Remembering that the I 's are related to the lattice periodic functions $u(\mathbf{r})$, they can be found by expanding the $u(\mathbf{r})$'s in a plane wave basis. Thus

$$\frac{1}{\Omega} \sum_{\mathbf{G}_1, \mathbf{G}_2} c_{\alpha\mathbf{k}_\alpha}^*(\mathbf{G}_1)c_{\beta\mathbf{k}_\beta}(\mathbf{G}_2)e^{i(\mathbf{G}_2 - \mathbf{G}_1)\cdot\mathbf{r}} = \sum_{\mathbf{G}_{\alpha\beta}} I_{\alpha\beta}(\mathbf{G}_\parallel)e^{i\mathbf{G}_\parallel\cdot\mathbf{r}}, \quad (4.69)$$

with c 's being the plane wave expansion coefficients. As only $I_{\alpha\beta}(-\mathbf{G}_\parallel)$ is needed, the only terms that survive are those where $-\mathbf{G}_\parallel = \mathbf{G}_2 - \mathbf{G}_1$. Remembering that \mathbf{G}_\parallel has a zero z-component this means that the z-component of \mathbf{G}_1 and \mathbf{G}_2 must be the same. The I 's are thus

$$I_{\alpha\mathbf{k}_\alpha\beta\mathbf{k}_\beta}(-\mathbf{G}_\parallel) = \sum_{\mathbf{G}_1} c_{\alpha\mathbf{k}_\alpha}^*(\mathbf{G}_1)c_{\beta\mathbf{k}_\beta}(\mathbf{G}_1 - \mathbf{G}_\parallel). \quad (4.70)$$

A similar expression can be found for the other orbital product as

$$I_{\gamma\mathbf{k}_\gamma\delta\mathbf{k}_\delta}(\mathbf{G}_\parallel) = \sum_{\mathbf{G}_1} c_{\gamma\mathbf{k}_\gamma}^*(\mathbf{G}_1) c_{\delta\mathbf{k}_\delta}(\mathbf{G}_1 + \mathbf{G}_\parallel). \quad (4.71)$$

Thus, in a plane wave expansion the integrals can be found as

$$E_{\alpha\beta\gamma\delta} = \frac{1}{\Omega} \sum_{\mathbf{G}_\parallel} w(\mathbf{q} + \mathbf{G}_\parallel) I_{\alpha\mathbf{k}_\alpha\beta\mathbf{k}_\beta}(-\mathbf{G}_\parallel) I_{\gamma\mathbf{k}_\gamma\delta\mathbf{k}_\delta}(\mathbf{G}_\parallel). \quad (4.72)$$

For Coulomb in the two-band approximation the α and β bands are both the same valence band, the γ and δ bands are both the same conduction band and the \mathbf{k} 's are different giving

$$E_C = \frac{1}{\Omega} \sum_{\mathbf{G}_\parallel} w(\mathbf{q} + \mathbf{G}_\parallel) I_{v\mathbf{k}'v\mathbf{k}}(-\mathbf{G}_\parallel) I_{c\mathbf{k}c\mathbf{k}'}(\mathbf{G}_\parallel). \quad (4.73)$$

If only the $\mathbf{G}_\parallel = \mathbf{0}$ term is used it can be seen that the equation reverts to the slow-rapid approximation derived in Sec. 4.4. For exchange the α and γ band are the same valence band, while the β and δ bands are the same conduction band. The Bloch phases cancel for exchange thus $\mathbf{k}_\alpha = \mathbf{k}_\beta$ and $\mathbf{k}_\gamma = \mathbf{k}_\delta$, so that $\mathbf{q} = \mathbf{0}$. Also the $\mathbf{G}_\parallel = \mathbf{0}$ term is not allowed in exchange, meaning the exchange matrix element is given as

$$E_{X,\alpha\beta\gamma\delta} = \frac{1}{\Omega} \sum_{\mathbf{G}_\parallel \neq \mathbf{0}} V(\mathbf{G}_\parallel) I_{v\mathbf{k}c\mathbf{k}}(-\mathbf{G}_\parallel) I_{c\mathbf{k}'v\mathbf{k}'}(\mathbf{G}_\parallel). \quad (4.74)$$

In the two-band approximation the Hamiltonian matrix elements become

$$H_{\mathbf{k},\mathbf{k}'} = E_{cv}(\mathbf{k}) - \frac{1}{\Omega} \sum_{\mathbf{G}_\parallel} I_{c\mathbf{k}c\mathbf{k}'}(-\mathbf{G}_\parallel) I_{v\mathbf{k}'v\mathbf{k}}(\mathbf{G}_\parallel) w(\mathbf{k} - \mathbf{k}' + \mathbf{G}_\parallel) + \frac{2}{\Omega} \sum_{\mathbf{G}_\parallel \neq \mathbf{0}} I_{v\mathbf{k}c\mathbf{k}}(-\mathbf{G}_\parallel) I_{c\mathbf{k}'v\mathbf{k}'}(\mathbf{G}_\parallel) V(\mathbf{G}_\parallel). \quad (4.75)$$

Using the same discretization as was used for Sec. 4.6 the Bethe-Salpeter equation becomes

$$E_{cv\mathbf{k}} + \frac{1}{4\pi^2} \sum_{\mathbf{k}'} \left[\sum_{\mathbf{G}_\parallel \neq \mathbf{0}} 2 \cdot I_{v\mathbf{k}c\mathbf{k}}(-\mathbf{G}_\parallel) I_{c\mathbf{k}'v\mathbf{k}'}(\mathbf{G}_\parallel) V(\mathbf{G}_\parallel) - \sum_{\mathbf{G}_\parallel} I_{c\mathbf{k}c\mathbf{k}'}(-\mathbf{G}_\parallel) I_{v\mathbf{k}'v\mathbf{k}}(\mathbf{G}_\parallel) w(\mathbf{k} - \mathbf{k}' + \mathbf{G}_\parallel) \right] \alpha_{\mathbf{k}'} \Delta k_x \Delta k_y = E \alpha_{\mathbf{k}}. \quad (4.76)$$

As previously the $\mathbf{k} = \mathbf{k}'$ term of the Coulomb part is divergent when $\mathbf{G}_\parallel = \mathbf{0}$ and can be calculated in the same way as Eq. (4.46). In order to actually calculate these matrix elements the sum over \mathbf{G}_\parallel needs to be truncated, which can be done by limiting the kinetic energy of the plane-waves to some maximum, in a similar way to how the plane-wave basis of a DFT calculation is truncated. Fig. 4.13(a) shows the different sets of \mathbf{G}_\parallel that the summation can be limited to. Each set is defined by a number dubbed the circle number $C\#$ and all \mathbf{G} -vectors within/on that circle are included in a calculation done with that $C\#$. For the 7 sets of \mathbf{G} 's shown in Fig. 4.13(a) the exciton binding energy has been calculated. It is found that including the \mathbf{G} 's lowers the binding energy by 0.05 eV which corresponds to 11% compared to the slow-rapid approximation, suggesting that going beyond the slow-rapid approximation may be necessary for obtaining accurate results. This increased accuracy does come at the cost of dramatically increased computation time. For the 50x50 K-grid used for the calculations in Fig. 4.13(b) $C\# = 0$ takes 10 minutes and the time increases linearly with the amount of \mathbf{G}_\parallel so that $C\# = 1$ takes 70 minutes and nearly 8 hours for $C\# = 6$. The difference of the binding energy at $C\# = 0$ in Fig. 4.13(b) compared to previous calculations are due to the lower k-grid and using G0W0 QP directly in Fig. 4.13(b) whereas scissor-shifted DFT eigenvalues have been used for all previous results.

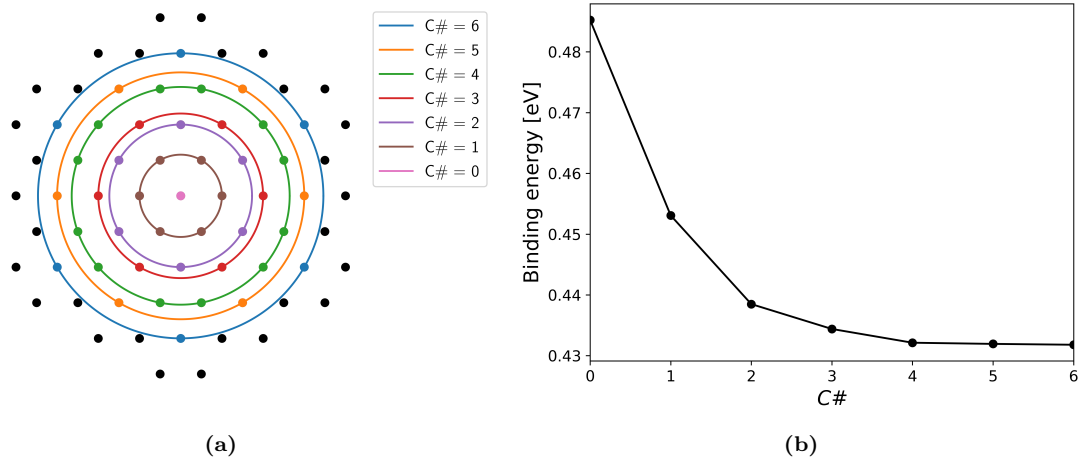


Figure 4.13: (a) Representation of the sets of \mathbf{G} -vectors that the calculation can be truncated to include, each point represents a \mathbf{G} -vector, it's color corresponds to the first set it is part of. Each set contain all other sets defined by circles with smaller radii. (b) Convergence of the exciton binding energy versus the circle number, calculated on a 50x50 k-point grid and using G0W0 QP energies.

Chapter 5

Doping and Excitons

For the single-particle response calculations in Chap. 3 including doping through the jellium model is simple, as all that is required is a DFT calculation with the jellium included. However, including doping in the BSE framework developed in Chapter 4 requires a few additional considerations. Doping adds additional charge carriers, and these charge carriers will screen the electron-hole interaction in addition to the screening by the intrinsic monolayer, thus a new expression for the effective dielectric function is required. This additional screening can be modelled by adding a so-called Lindhard function to the effective dielectric function. Furthermore a derivation of the Bethe-Salpeter equation where the occupation factors of the orbitals used to construct the basis of Slater determinants are not binary, leads to a Fermi function appearing on the non-diagonal terms of the BSE matrix [43]. In the slow-rapid approximation this means that the BSE matrix should be constructed according to

$$H_{\mathbf{k}\mathbf{k}'} = \begin{cases} E_{c\nu\mathbf{k}} - \frac{e^2}{4\pi r_0 \epsilon_0} \ln\left(\frac{ar_0 + \epsilon}{\epsilon}\right) & \mathbf{k} = \mathbf{k}' \\ -\frac{1}{4\pi^2} f_{vc}(\mathbf{k}) I_{c\mathbf{k}\mathbf{k}'} I_{v\mathbf{k}\mathbf{k}'} w(\mathbf{k} - \mathbf{k}') \Delta k_x \Delta k_y & \mathbf{k} \neq \mathbf{k}', \end{cases} \quad (5.1)$$

so that the coupling due the Coulomb interaction is suppressed between state, where electrons have been added or removed compared to the intrinsic case where $f_{vc} = 1$.

5.1 Screening by additional charge carriers

A thorough derivation of the screened potential could start with the single-particle density response function. This function relates total potential, which is the sum of the external/applied potential and an induced potential caused by the electron-electron interactions in the material, to the induced charge density. The microscopic dielectric function can be defined in terms of this density response function and thus it relates to the screened potential. Eventually, one can arrive at an expression for the density response function on the form

$$\chi_{\mathbf{G},\mathbf{G}'}(\mathbf{q},\omega) = \frac{2}{\Omega} \sum_{n,m,\mathbf{k}} \left(f(E_{n\mathbf{k}}) - f(E_{m\mathbf{k}+\mathbf{q}}) \right) \frac{I_{nm\mathbf{k}\mathbf{q}}(\mathbf{G}) I_{nm\mathbf{k}\mathbf{q}}(\mathbf{G}')}{\hbar\omega + E_{n\mathbf{k}} - E_{m\mathbf{k}+\mathbf{q}}}, \quad (5.2)$$

where $I_{nm\mathbf{k}\mathbf{q}}(\mathbf{G})$ is the Fourier component of the product of the lattice periodic functions i.e. it is given by Eq. (4.63). The Lindhard function amounts to neglecting everything but the $\mathbf{G} = \mathbf{G}' = 0$ part of the density response function and assuming that only one band is important and using an effective mass description for that band. With these approximations the Brillouin zone integrations can be carried out analytically and an expression for the frequency dependent Lindhard function can be found. In the static

limit $\omega = 0$ one gets the effective dielectric function [22]

$$\varepsilon(q) = \bar{\varepsilon} + r_0 q + \frac{g m_e^*}{a_0 q} \left(1 - \theta(q - 2k_F) \sqrt{1 - \frac{4k_F^2}{q^2}} \right). \quad (5.3)$$

The first two terms is the linear model for the intrinsic monolayer from Sec. 4.3 and the third due to doping where m_e^* is the effective electron mass, a_0 is the Bohr radius, g is the product of spin and valley degeneracies and k_F is the Fermi wave vector which can be found from the doping density n as $k_F = \sqrt{\frac{4\pi n}{g}}$ and θ is the Heavi-side step function. Fig. 5.1(a) shows the inverse of this function for several doping concentrations. This expression is only valid for zero kelvin, so to include temperature the following expression should be used

$$\varepsilon(q) = \bar{\varepsilon} + r_0 q + \frac{g m_e^*}{a_0 q} L_t \left(\frac{q}{k_F}, \frac{kT}{E_F} \right), \quad (5.4)$$

where E_F is the Fermi level at the temperature T . The Fermi distribution broadened Lindhard function $L(z, t)$ is given by

$$L_t(z, t) = \frac{2}{z} \int_0^{z^2/4} \frac{1}{\left[\exp\left(\frac{x - \text{sgn}(t)}{|t|} + 1\right) + 1 \right] \sqrt{z^2 - 4x}} dx. \quad (5.5)$$

This integral can be evaluated numerically using a trapezoidal integration scheme, alternatively a different expression can be obtained by employing integration-by-parts and that expression can be solved numerically. The integration-by-parts expression works well for higher doping concentrations, but was found to lead to numerical problems at low doping concentrations because of overflows in the exponential functions, therefore Eq. (5.5) was solved numerically using trapezoidal integration with 5000 points for x for all concentrations/ q -points. The inverse of the effective dielectric function for a range of doping concentration is shown in Fig. 5.1(b). Compared to the undoped case it is seen that at small q the effective dielectric function no longer approaches one but trends towards infinity, so that the electron-hole interaction becomes greatly reduced at large separations in real-space due to the extra screening.

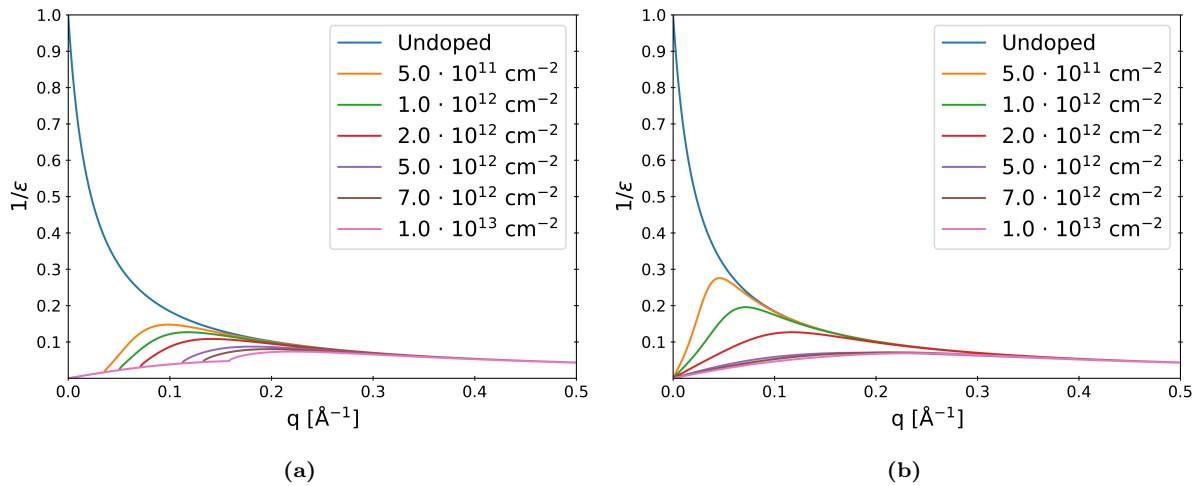


Figure 5.1: Inverse effective dielectric function for different doping concentrations using parameters for MoS_2 for (a) Zero temperature (b) Room temperature.

Interestingly it is seen that the screening decreases with temperature meaning the binding energy should be higher at room temperature. The BSE matrix is still given by Eq. (4.47), but now Eq. (5.4) should be

used for the screened potential, which means that the analytical expression for the diagonal is no longer valid. Instead it needs to be calculated through

$$W_{diag} = -\frac{e^2}{4\pi\epsilon_0} \int_0^a \frac{1}{(r_0q + \bar{\epsilon} + L(q))} dq, \quad (5.6)$$

where $L(q)$ denotes the third-+ term of Eq. 5.4 including the front factor. With $L(q)$ in the denominator this can no longer be calculated analytically and must be done numerically.

For every matrix element Eq. (5.5) needs to be evaluated in order to calculate the screening. Even for a small k-grid with 900 k-points this means the time it takes to calculate the BSE matrix increases by a factor of 10, because this integral is evaluated ~ 405000 times. To solve this problem the inverse dielectric function is evaluated at 5000 points between $q = 10^{-10} \text{ \AA}^{-1}$ and the maximum q that enters the calculation and linear interpolation is employed for each q that enters the BSE matrix. This approach makes including additional screening negligible in terms of computational time.

Returning to the Wannier approximation the effects of the Lindhard function can be analyzed without obtaining ab-initio wave functions and eigenvalues for each doping concentration. Within the effective mass approximation the zero-temperature Fermi level relates to the Fermi wave vector as $E_F^0 = \frac{\hbar^2 k_F^2}{2m_e}$ and the Fermi level with temperature can be found from $E_F = kT \ln(\exp(E_F^0/kT) - 1)$ [22]. The binding energy of the 1s exciton in MoS₂ with doping has been calculated using the Wannier approximation, with and without temperature as shown in Fig. 5.2.

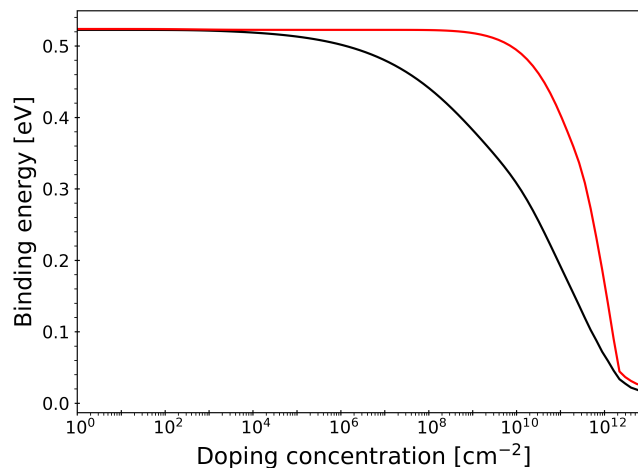


Figure 5.2: Wannier exciton binding energy in MoS₂ at various doping concentrations, with (red line) and without (black line) temperature included in the Lindhard function.

5.2 Quasiparticle energies with doping

As mentioned in Chap. 4, the energies entering the Bethe-Salpeter equation should be quasiparticle energies, which can be calculated through the G0W0 approximation. However, screening also enters in the G0W0 calculation, and the QP energies will change accordingly. In the undoped BSE calculations a scissor shift was determined to be appropriate, but with screening by additional carriers, a scissor operation is not guaranteed to be a good approximation. G0W0 eigenvalues have been calculated for a range of doping concentrations, and the band structures of a few of them are shown in Fig. 5.3.

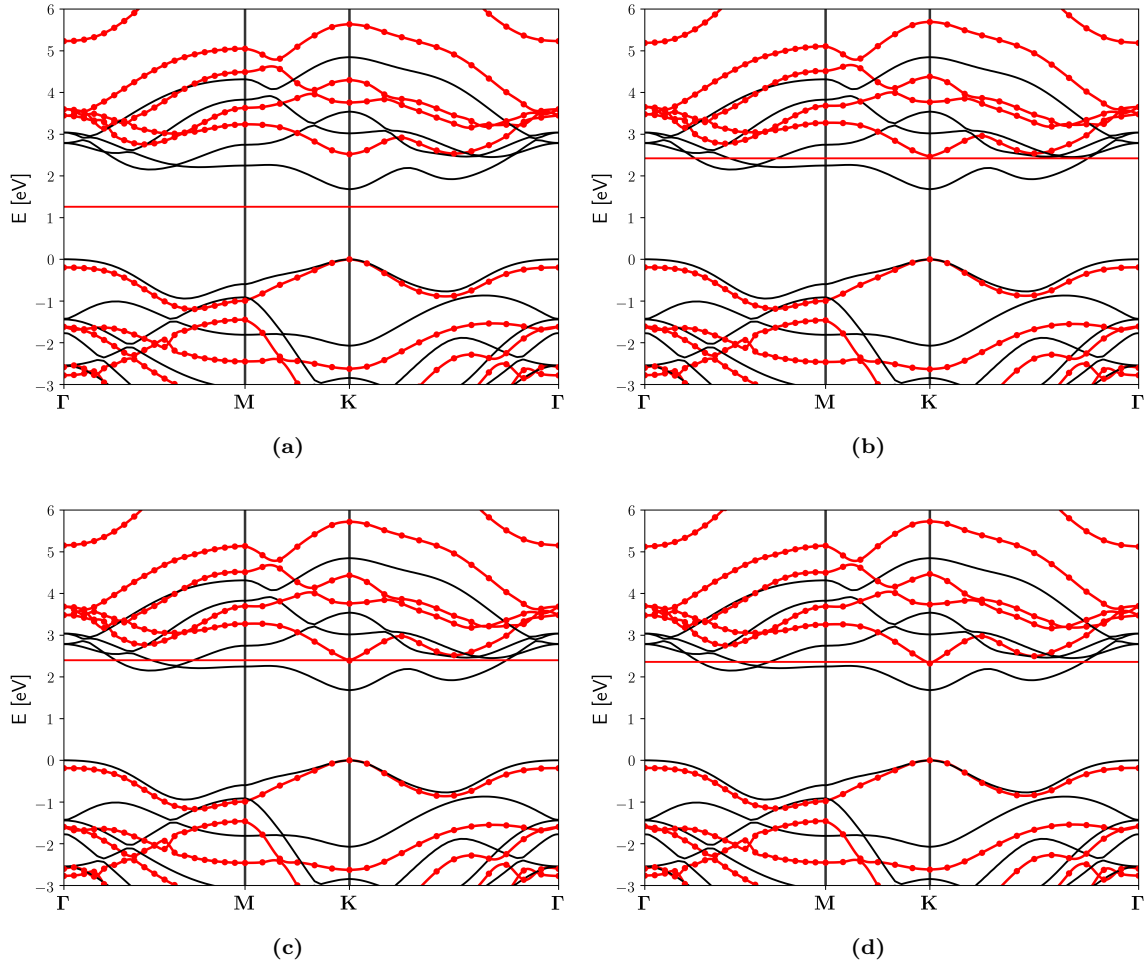


Figure 5.3: MoS₂ band structures from DFT (black lines) and G0W0 (red lines) and G0W0 room temperature Fermi level (red line) for different doping levels, (a) 0 cm⁻², (b) 1 · 10¹² cm⁻², (c) 2 · 10¹² cm⁻², (d) 3 · 10¹² cm⁻². The G0W0 band structures are interpolated from a 36x36 Monkhorst-Pack grid using piecewise cubic 2D interpolation, dots represent calculated data points.

Two important effects are present in the G0W0 band structures, the band gap becomes smaller also known as band gap renormalization, which is an effect that other studies have also found, however, it is also clear that the effective electron mass decreases as the doping increases [44]. Changes in the effective mass influences the additional screening added by the Lindhard term in the effective dielectric function and will thus be quite important. Both of these effects make it necessary to include QP energies directly for G0W0 calculations rather than scissor shifted DFT calculations. The G0W0 calculations are performed on 36x36 Monkhorst-Pack grids and then interpolated by a piecewise cubic 2D interpolation scheme both for viewing band structures and for the QP energies entering the BSE equation. The room-temperature Fermi level is calculated based on the interpolated grid and is shown in Fig 5.4(a). As expected the Fermi level is below the conduction band edge at low doping concentrations and moves into the band as the doping level increases. The band gap as a function of doping concentration is shown in Fig. 5.4, showing a 0.4 eV decrease between 0 and 1 · 10¹³ cm⁻² doping concentrations. Both properties behave monotonically from 0 to 7 · 10¹² cm⁻² where the band gap increases sharply which is somewhat puzzling.

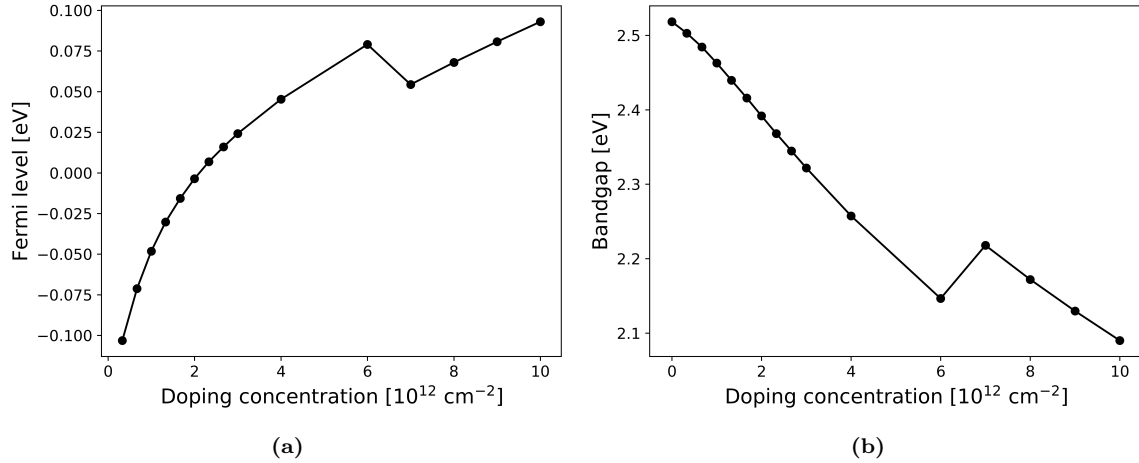


Figure 5.4: (a) Room temperature G0W0 Fermi level relative to the conduction band at different doping concentrations. (b) G0W0 band gap for different doping concentrations.

The effective masses were found by fitting a matrix \mathbf{A} to the 17 \mathbf{k} -points closest to the \mathbf{K} special point according to

$$E = \frac{\hbar^2}{2m_e} \mathbf{k}^T \mathbf{A} \mathbf{k}. \quad (5.7)$$

The eigenvalues of \mathbf{A} is the inverse effective mass, for intrinsic MoS_2 this yields an effective electron mass of 0.54, in good agreement with Rasmussen et al. who calculated a mass of 0.55 for MoS_2 [38]. Figure 5.5(a) shows the band structure zoomed in around \mathbf{K} plotted alongside the parabola defined by the effective mass, showing that this technique fits the mass quite well, even though the amount of k-points is low.

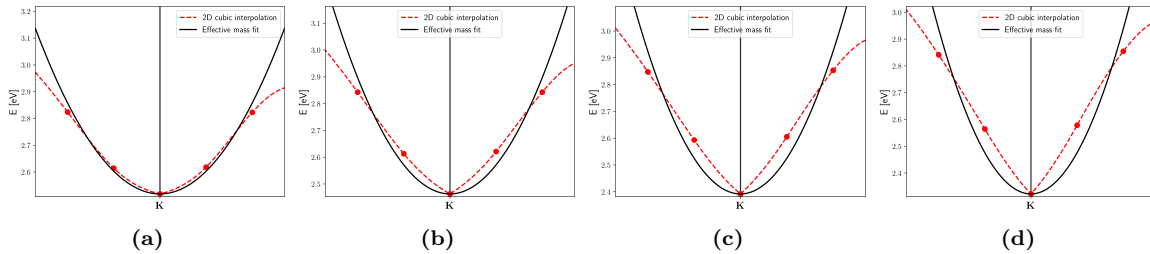


Figure 5.5: Conduction band of MoS_2 for G0W0 around the \mathbf{K} -point and parabolic band from calculated effective masses for (a) 0 cm^{-2} , (b) $1 \cdot 10^{12} \text{ cm}^{-2}$, (c) $2 \cdot 10^{12} \text{ cm}^{-2}$, (d) $3 \cdot 10^{12} \text{ cm}^{-2}$

However, in Fig. 5.5(b-d), which shows similar zooms around the \mathbf{K} for different doping concentrations, it is seen that the fit becomes worse when doping is included. It is clear from Fig. 5.5(b-d) that the fit is not perfect, however, it should be noted that fitting overestimates the effective mass but including the obtained masses will still be a better approximation than using the mass of the intrinsic case regardless of the doping concentration. Fig. 5.6 shows the effective electron and hole masses versus doping concentration, with a quadratic fit between $0 \cdot 10^{12} \text{ cm}^{-2}$ and $3 \cdot 10^{12} \text{ cm}^{-2}$.

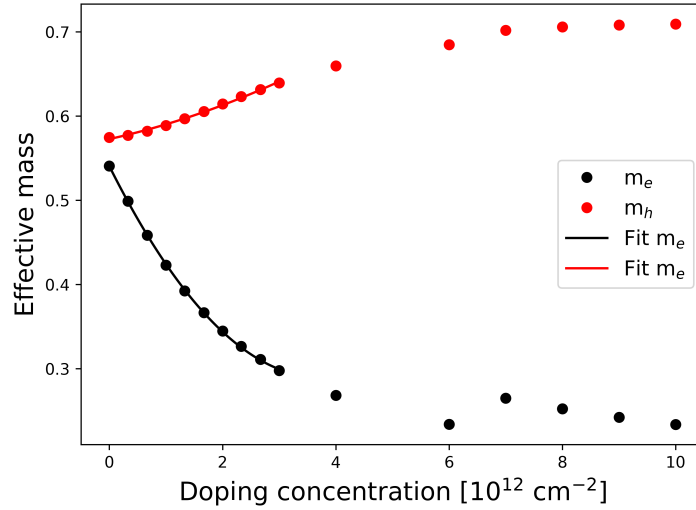


Figure 5.6: Effective mass as a function of doping concentration for both electron and hole. Effective masses are calculated from the 17 nearest k-points to the \mathbf{K} special point from 36x36 G0W0 calculations. Fits are 2nd order polynomials.

The fits of the effective mass presented in Fig. 5.6 can be used in the Wannier model, so that both the effective exciton mass present in the effective mass approximation for the dispersion of the bands and the effective electron mass in the Lindhard screening term become functions of the doping concentration, rather than being independent of the doping concentration as in Fig. 5.2. At low temperature the effect is barely visible, however, at room temperature this doping dependence causes the binding energy to decrease faster than if it had been neglected.

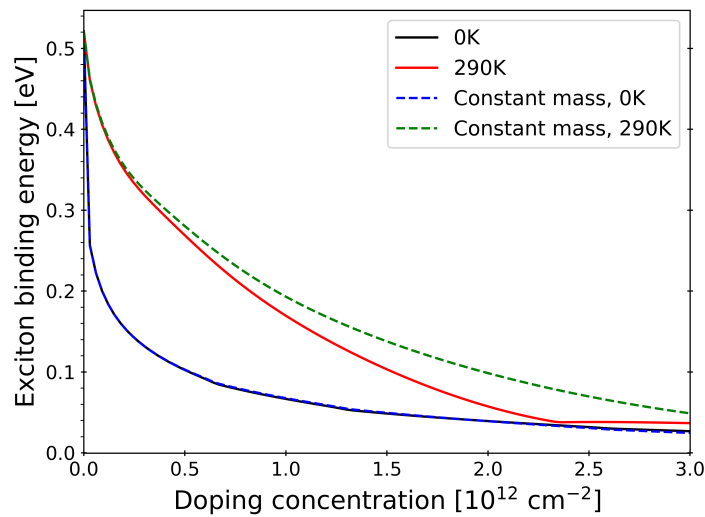


Figure 5.7: Exciton binding energy from the Wannier model, solid lines are calculated using the polynomial fit to calculate effective masses from Fig. 5.6, dashed lines are calculated using an effective electron mass of 0.55 and electron-hole mass of 0.28 independently of doping concentration.

5.3 Doped MoS₂

The exciton binding energy as a function of doping is shown in Fig. 5.8. It is found that the binding energy decreases steadily with doping concentration, dropping under 100 meV for doping concentrations higher than $1.33 \cdot 10^{12} \text{ cm}^{-2}$. The model thus matches the experimentally found behaviour of decreasing the binding energy as the doping concentration is increased [10].

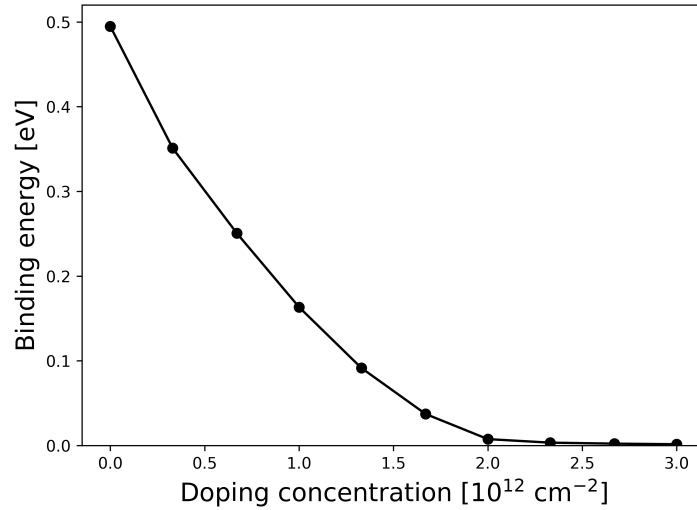


Figure 5.8: Freestanding MoS₂ exciton binding energy versus doping concentrations using G0W0 QP energies in the slow-rapid approximation and doping dependent effective mass in Lindhard screening.

The optical conductivity of MoS₂ was calculated according to Eq. (4.57) at a range of doping concentrations as shown in Fig. 5.9. Experimentally it is found that the position of the exciton absorption peak is unaffected by increased doping. This behavior is not replicated in the calculation, visible from both Fig. 5.9 and Fig. 5.10(b).

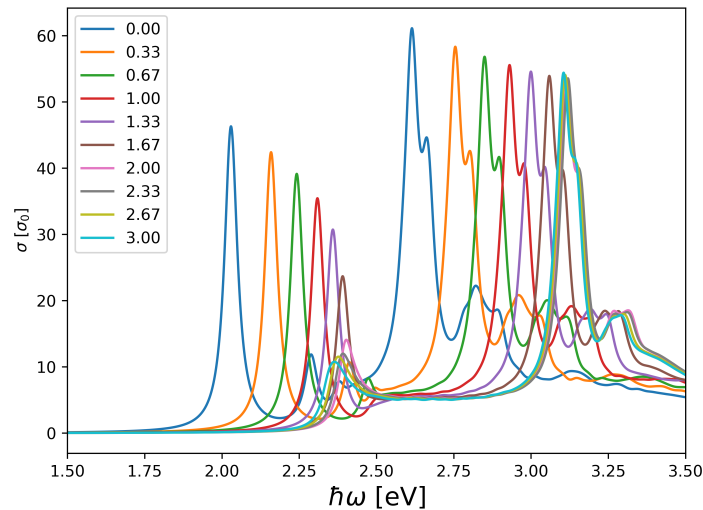


Figure 5.9: Optical conductivity of MoS₂ at different doping concentrations, legends are in 10^{12} cm^{-2} .

However, the calculation does show that with increasing doping concentration the conductivity of the first exciton peak decreases, see Fig. 5.10(a). Fig. 5.10(a) shows both the conductivity of the first peak

and the absolute square of the momentum matrix element corresponding to $|P_S|^2$ with $S = 0$ in Eq. (4.57) normalized according to $|P_0|^2$ in the undoped case, dubbed 'normalized momentum' in the figure. The conductivity has an inverse dependence on $\hbar\omega$, meaning even if $|P_0|^2$ was independent of doping concentration the conductivity would decrease due to the increase in the exciton position. It is however found that $|P_0|^2$ also decreases monotonically with doping.

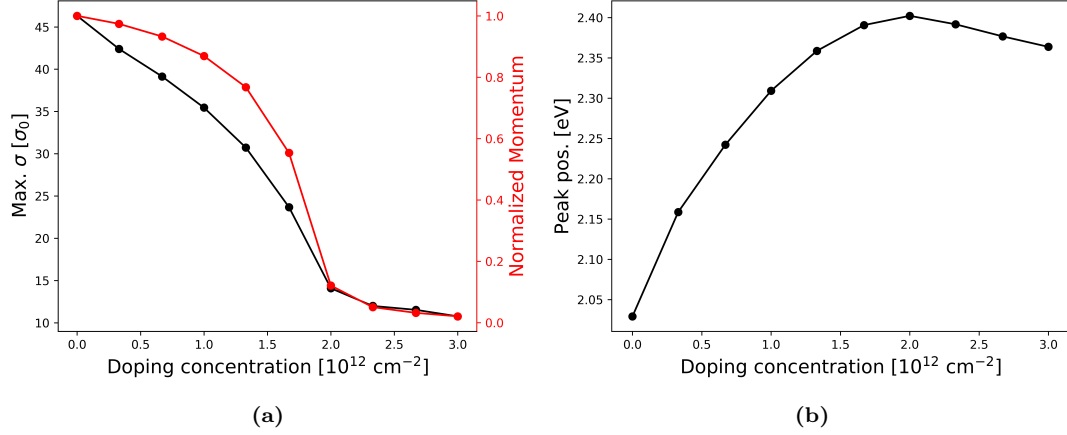


Figure 5.10: (a) Maximum optical conductivity and normalized momentum of the lowest energy exciton. (b) Position of the exciton peak as a function of doping concentration.

5.4 Doped hBN encapsulated MoS_2

The effective dielectric constant used allows for including screening caused by substrate/superstrate and a calculation has been performed with MoS_2 encapsulated in hBN with a dielectric constant of $\bar{\epsilon} = 4.5$. The intrinsic binding energy of MoS_2 is reported to be 0.220 eV [45], with the model resulting in a value of 0.166 eV. Again it is observed that the binding energy becomes nearly zero when the doping concentration reaches $2 \cdot 10^{12} \text{ cm}^{-2}$.

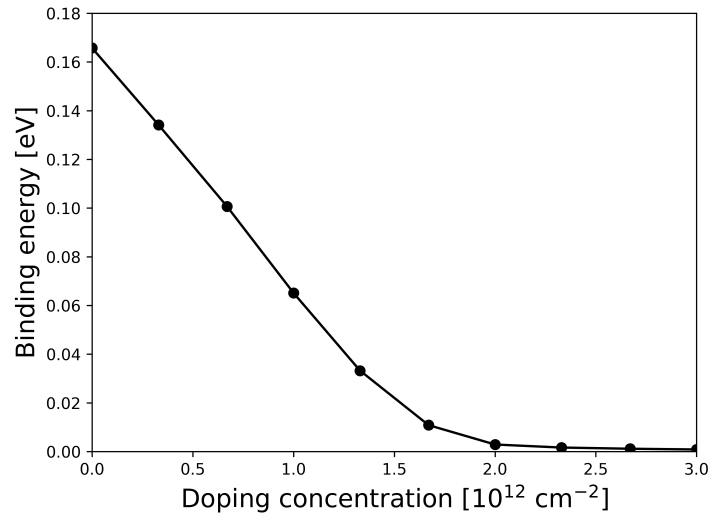


Figure 5.11: Binding energy of lowest exciton in hBN ($\bar{\epsilon} = 4.5$) encapsulated MoS_2 at different doping concentrations with slow-rapid BSE with G0W0 QP energies

The optical conductivity has also been calculated for hBN encapsulated MoS₂ as shown in Fig. 5.12, and the same behavior as in the suspended case is observed; as the doping concentration increases the maximum conductivity of the lowest lying exciton decreases monotonically and the same is true for the normalized momentum, see Fig. 5.13(a). However, in this case the band gap renormalization is large enough to keep the exciton position nearly constant with a maximum difference of the position of the conductivity peak of 0.06 eV as seen in Fig. 5.13(b). This is, however, not a completely fair comparison. While an approximation of the screening caused by the encapsulation is included in the BSE calculation, the QP energies are still calculated from a G0W0 calculation of suspended MoS₂.

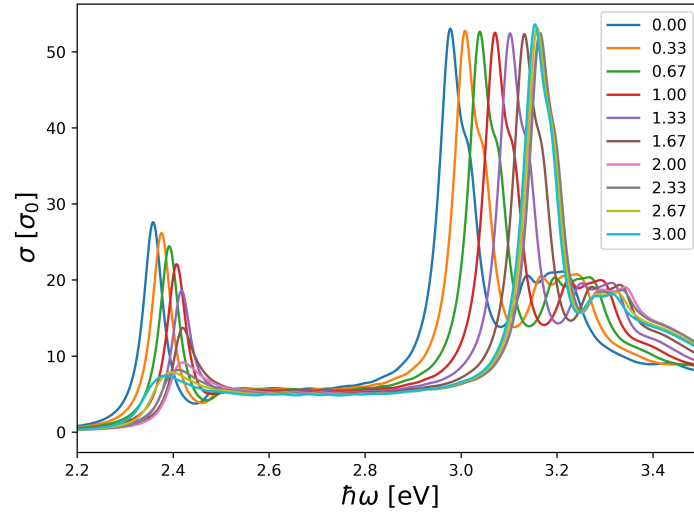


Figure 5.12: Optical conductivity of hBN ($\bar{\epsilon} = 4.5$) encapsulated MoS₂ at different doping concentrations calculated with slow-rapid BSE with G0W0 QP energies. Legends are in 10^{12} cm^{-2}

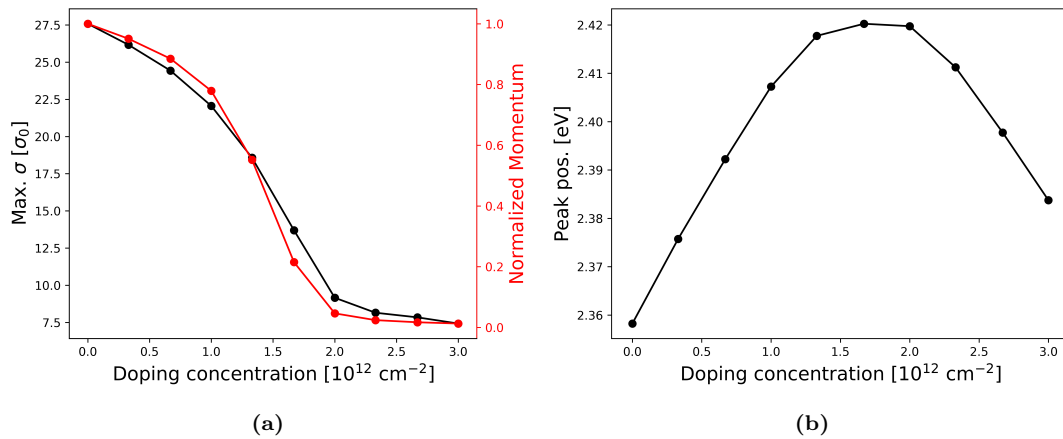


Figure 5.13: (a) Maximum optical conductivity of the A exciton from slow-rapid BSE for hBN encapsulated MoS₂. (b) Position of the exciton peak as a function of doping concentration for hBN encapsulated MoS₂.

5.5 Dynamic screening

The use of a static dielectric screening has been found to be insufficient in literature, as it underestimates the binding energy at high doping concentration. The model presented by Gao et al. includes a plasmon-pole approximation for the dielectric function [44]. In their plasmon-pole approximation (PPA) the dielectric function is self-consistently updated according to

$$\varepsilon^{-1}(q, E_{int}) = \varepsilon^{-1}(q, 0) + \frac{E_{int} \left(1 - \varepsilon^{-1}(q, 0)\right)^{3/2}}{\omega_p(q) + E_{int} \sqrt{1 - \varepsilon^{-1}(q, 0)}}, \quad (5.8)$$

where $\varepsilon^{-1}(q, 0)$ is the static dielectric function and E_{int} is a quantification of electron-hole interaction energy given by $E_{int} = \sum_{\mathbf{k}} E_{cv}(\mathbf{k}) |\alpha_k|^2 - E_S$ and $\omega(q) = \sqrt{2\pi n q}$ is the plasma frequency and n is the total 2D charge density. This is solved self-consistently as the screening depends on E_{int} and E_{int} depends on the screening. The convergence criteria has been chosen to be that the difference in the smallest eigenvalue of the BSE matrix being below 10^{-5} Ha. As has been shown previously the inclusion of the Lindhard screening term causes the inverse dielectric function to go to 0 at low q signifying infinite screening for long-range interactions in real-space. Inspection of Eq. (5.8) shows that at low q the PPA effective dielectric function goes to 1, which allows long-range interactions in real-space increasing the binding energy. The choice of n is somewhat arbitrary Gao et. al. uses 26 valence electrons per unit cell plus doping, which corresponds to the amount of electrons in the pseudopotential they use for the calculation. The inverse effective dielectric function at different doping concentrations for $n = 26$ after convergence has been reached is plotted in Fig. 5.14(a), clearly the PPA screening is equal or smaller than the static screening for all q which will increase the exciton binding energy. To study how the choice of n influences the calculation the PPA screening at a doping concentration of $1 \cdot 10^{12} \text{ cm}^{-2}$ has been calculated for $n = 7, 14, 26$ and is plotted in Fig. 5.14(b). As mentioned $n = 26$ corresponds to including semi-core states for MoS_2 , $n = 14$ corresponds the number of electrons in the block of bands near the Fermi level and $n = 7$ is half of that.

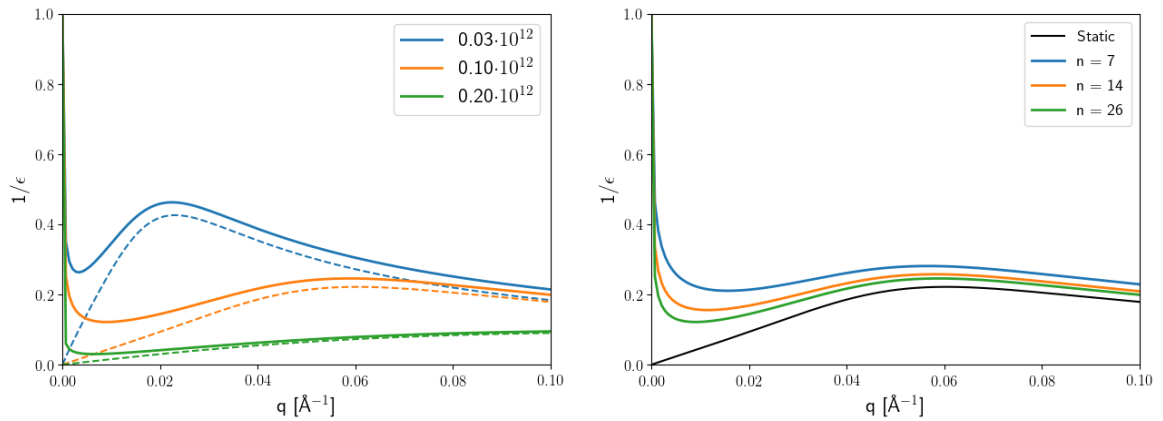


Figure 5.14: (a) Converged PPA dielectric function at different doping concentrations, full lines are PPA and dashed lines are static (b) Converged PPA dielectric function for different choices for the number of electrons in the plasma frequency at a doping concentration of $1 \cdot 10^{12} \text{ cm}^{-2}$.

The binding energy versus doping of the lowest lying exciton in MoS_2 has been calculated for different choices of n , and is shown in Fig. 5.15. As expected the binding energy is increased for all doping concentrations irrespectively of the choice of n , including for zero doping. In the undoped case Gao et al. finds that the PPA decreases the binding energy by 40 meV compared to a static calculation, this

is clearly not reproduced in Fig. 5.15 with increases of 80 meV, 120 meV and 200 meV for $n = 26, 14, 7$. Secondly the exciton binding energy is not stabilized at higher doping concentrations as it is in Gao et al.'s calculation, this can be explained by an inconsistent used of the PPA model. Gao et al. use the PPA model for both the the GW and BSE calculations causing bandgap renormalization and exciton renormalization to cancel, thus stabilizing the binding energy at higher doping concentrations.

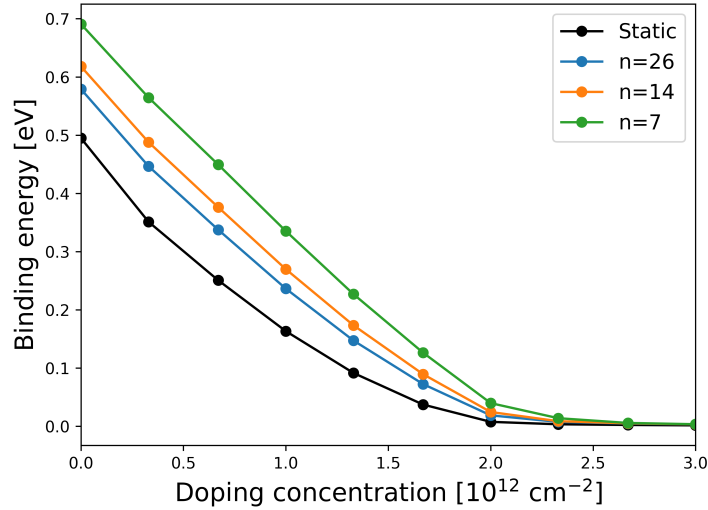


Figure 5.15: Exciton binding energy versus doping for different choices of the number of electrons entering the plasma frequency n .

Although the theory that has been presented has in most cases been in good agreement with experiments and other levels of theory, there is room for improvement. The use of an analytical expression for the screening can allow for calculations without having to perform expensive quasiparticle calculations, but as it has been found that the effective masses depend significantly on doping in practice a G0W0 calculation is still required. For example, if one wants to compare the optical properties of a large amount of TMDS doing several G0W0 calculations for each material would require enormous computational resources. Furthermore, as the screened potential is determined during the G0W0 calculation one might as well not approximate and just utilize the potential already calculated. The level of theory used in this thesis is thus at an unfortunate middle ground between computational efficiency and accuracy of the theory, any improvement should focus on either of these. A study of the physics behind the decreasing effective mass with increased doping concentration could allow one to estimate this dependence and include this effect in the model without requiring a G0W0 calculation. On the other side, using the screened potential from the G0W0 calculation would return the framework to an ab-initio model which one would expect increases agreement with experiments.

Chapter 6

Experimental Results

Two 1x1 cm samples of monolayer MoS₂ on thermally grown SiO₂ on a degenerately doped Si-substrate were obtained from the company "2D semiconductors", the MoS₂ layer was grown by atmospheric pressure chemical vapor deposition. The SiO₂ thickness was chosen to increase contrast in microscopy images to make the characterization and fabrication processes easier, studies have shown that maximum contrast can be reached with a SiO₂ thickness between 230-280 for a wide range of wavelengths thus 260 nm was chosen [46]. The first sample was characterized by photoluminescence, and Raman spectroscopy measurements, as well as AFM, while the second and last sample was characterized with Raman spectroscopy.

6.1 Characterization of MoS₂

Raman Spectroscopy was used to determine the amount of layers of the first MoS₂ sample, by looking at the relative position of the Raman peaks, E_{2g}^1 and A_{1g} as shown in Fig. 6.1(a) from Li et al. For a monolayer the relative difference in Raman shift for a 532 nm laser line for E_{2g}^1 and A_{1g} is 18 cm⁻¹, while for a bilayer the relative difference is 22 cm⁻¹ according to [47].

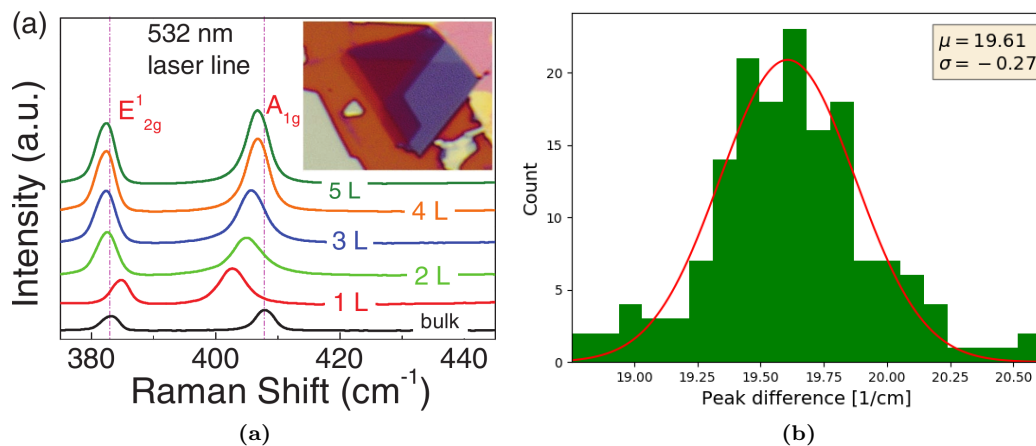


Figure 6.1: (a) Raman scattering taken from Li et al., showing how the Raman peaks change position in relation to each other, depending on the amount of layers of MoS₂. It is seen that the A_{1g} blue-shifts, while the E_{2g}^1 red-shifts with increasing amount of MoS₂ layers. [47] (b) Histogram of difference in Raman peak position for E_{2g}^1 and A_{1g} for 160 measurements performed in an array on the first sample.

160 measurements were done in an array on the first MoS₂ sample using a 532 nm excitation laser line. Comparing the relative position of the Raman peaks E_{2g}^1 and A_{1g} for all measurements gives the histogram shown in figure 6.1(b). A Gaussian fit gives a peak difference of 19.6 cm⁻¹ for the sample, thus closer to the reported 18 cm⁻¹ for monolayer MoS₂, than the 22 cm⁻¹ for bilayer MoS₂. The second sample showed similar Raman peak positions, with an average peak position of 19.6 cm⁻¹, over 3 measurements. Furthermore the two samples were indistinguishable in an optical microscope, with a homogeneous layer covering the entire samples, except for slight inconsistencies in the corners.

PL spectroscopy showed that the first sample exhibited large photoluminescence, in comparison to the Raman-peaks seen on the far left in figure 6.2(a). This is in agreement with Splendiani et al. who did a similar experiment on different amounts of layers of MoS₂, and found that monolayer MoS₂ had a high photoluminescence in comparison to the Raman peaks as seen in Fig. 6.2(b). However, the shape and location of the photoluminescence peak for the sample is not similar to Splendiani et al.. Splendiani asserts that the two photoluminescence peaks are due to the direct excitonic transitions known as A1 and B1, however, neither are easily visible in the PL spectra of the sample. [41]

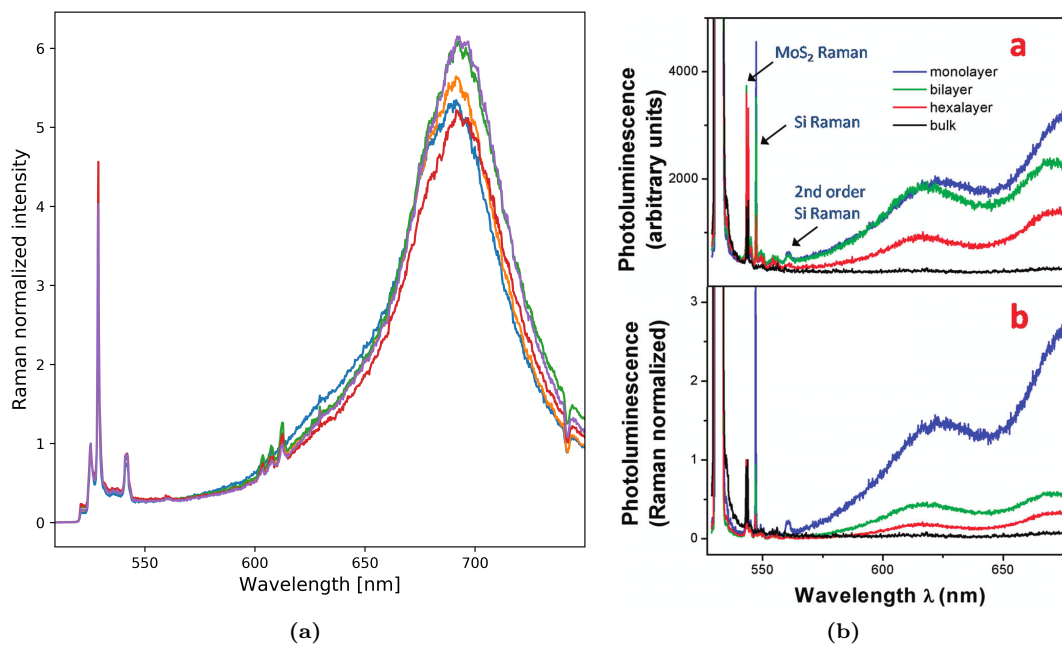


Figure 6.2: (a) 5 PL spectra of MoS₂ sample taken at random locations on the sample, normalized to the Raman peaks seen on the far left, showing a large photoluminescence near 690 nm in comparison to the Raman peaks. (b) PL spectra from Splendiani et al., showing a large photoluminescence for monolayer MoS₂ at 625 nm and 675 nm. [41]

As both of the optical measurements above were somewhat inconclusive, with differences in Raman shifts being consistently in between what is reported for monolayer and bilayer and the excitonic transition not being clearly visible in photoluminescence spectroscopy, AFM images were taken to ensure that the sample was monolayer. AFM measurements were done in a corner of the first sample, which showed only triangular islands of MoS₂ on SiO₂ as seen in Fig. 6.3(a). The measurements shows, as indicated by figure 6.3(c) that the MoS₂ layer has a thickness of 6.8 Å, which agrees well with the thickness reported by Li et al. and Splendiani et al. for a monolayer. [41, 47]

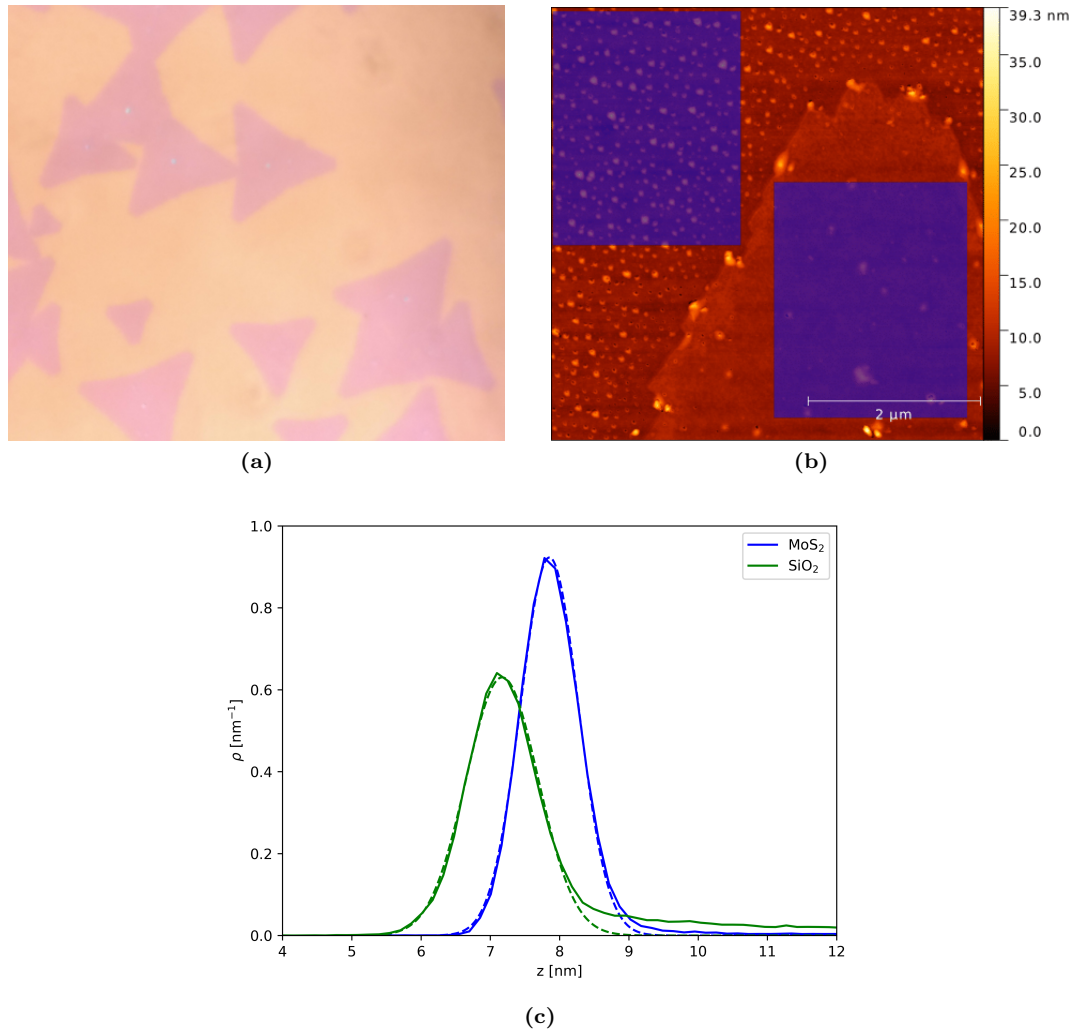


Figure 6.3: (a) Image of island growth in a corner of one of the MoS₂ sample. (b) AFM height image, with two shaded areas indicating locations for the histograms in figure (c). The upper left shaded area is SiO₂, while the lower left shaded area is MoS₂. (c) Height-histogram of the two blue-shaded areas of figure (b), indicating a height difference between the two shaded areas of 6.8 Å.

6.2 Fabrication of capacitor

In order to gate the MoS₂ monolayer plate capacitors were fabricated, to function similarly to the schematic shown in Fig. 3.1. The silicon substrate was heavily doped in order to act as one side of the capacitor, while an array of gold plates were fabricated on top. The sample had about 250nm SiO₂ thermally grown on both sides, allowing for better contrast of the MoS₂ in an optical microscope as shown in Fig 6.4(a). The gold plates on the first sample were made by E-beam lithography (EBL), and were 100x100 μm in size and 70 nm thick. However, it proved to be extremely difficult to wire bond to these gold plates for several reasons. In order to ensure that successful wire bonding was possible for the second sample, a more rapid fabrication method was required so that test contacts could be produced on Si substrates. For this reason direct laser writing was used over EBL as it has micrometer resolution and is orders of magnitude faster than EBL. It was found that wire bonding had a higher success rate on 300x300 μm contacts of 140 nm thickness. To confirm that the wires had successfully bonded, the resistance over the wires and the gold-plates was measured resulting in resistances of 1 – 3Ω.

In order to ensure electrical contact to the Si substrate, a hole through the bottom SiO_2 layer was etched with hydrofluoric acid, while the MoS_2 layer was coated with photoresist to be protected during the application of the hydrofluoric acid as shown in Fig. 6.4(b). Then the bottom was coated with 70 nm gold by magnetron sputtering and the photoresist was removed as shown in Fig. 6.4(c). Afterwards the gold plates on top needed to be made. First the sample was spin-coated to a layer of about $2 \mu\text{m}$ photoresist, which was then exposed using direct laser writing and developed as shown in Fig. 6.4(d). Then the sample top was sputtered with 7 nm titanium and 140 nm gold as shown in Fig 6.4(e). After liftoff in acetone using ultrasound the sample had 167 gold plates on top of the MoS_2 layer. The finished sample was attached to an aluminum backplate using conductive silver epoxy and pieces of goldplated PCBs were mounted on the top of the aluminum using insulating tape and wire bonding was done from the PCB to the gold contacts on the MoS_2 layer, as schematically shown in 6.4(f).

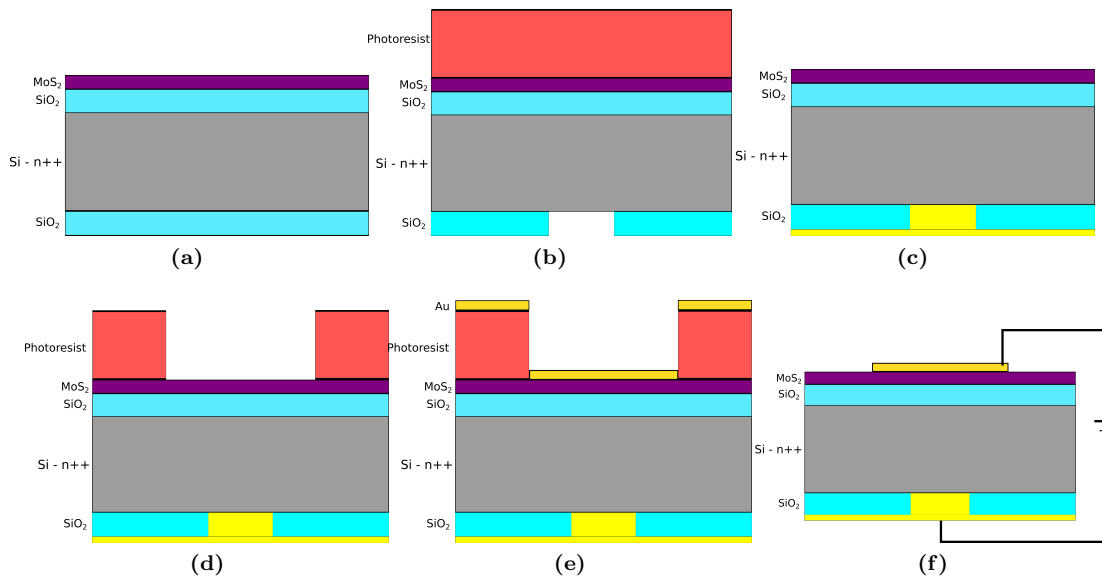


Figure 6.4: Illustration of fabrication process: (a): MoS_2 sample before fabrication. (b): Etching of bottom SiO_2 layer with hydrofluoric acid, while the top is protected by a layer of photoresist. (c): 70 nm gold is sputtered on the bottom of the sample. (d): Photoresist is put on top, and exposed to direct laser writing at 167 $300 \times 300 \mu\text{m}$ squares, and then developed. (e): 7 nm Titanium and 140 nm gold is sputtered on the top of the sample. (f): Photoresist is removed by liftoff and sample is connected to external power supply.

The 167 gold contacts were made on top of the MoS_2 layer, distributed in the pattern shown in Fig. 6.5 to allow different spacing between the gold plates. A picture of the sample (in all its glory) after fabrication and mounting is shown in Fig. 6.5(b).

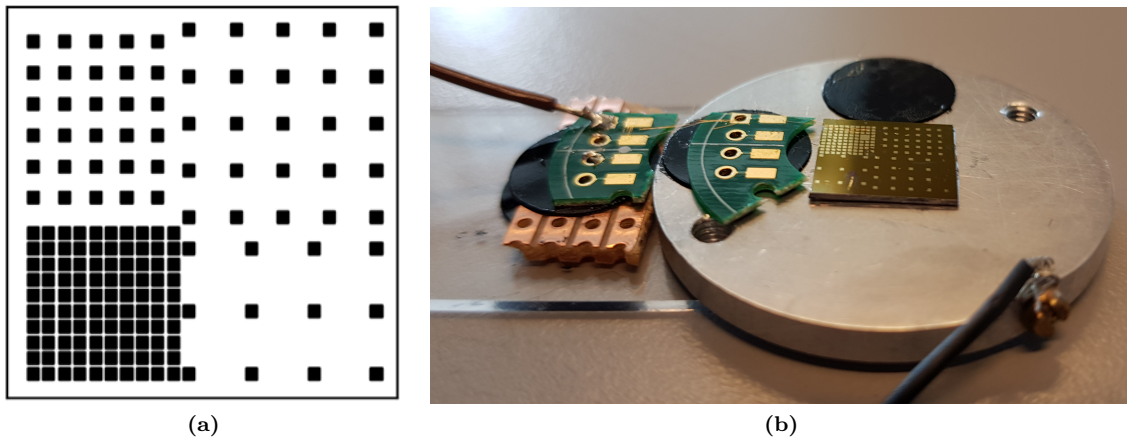


Figure 6.5: Illustration of the $300 \times 300 \mu\text{m}$ gold plates fabricated using direct laser writing, with 100, 200, 300, and $400 \mu\text{m}$ spacing.

6.3 Reflection experiment

After the fabrication of the gold plates the sample was investigated using reflection spectroscopy, using an optical microscope equipped with a field iris diaphragm to limit the field of view to only include the MoS_2 using a halogen light source, Fig. 6.6 shows a schematic of the measurement equipment. An Andor Shamrock 303i spectrometer cooled to $-40 \text{ }^\circ\text{C}$ was used for measurements.

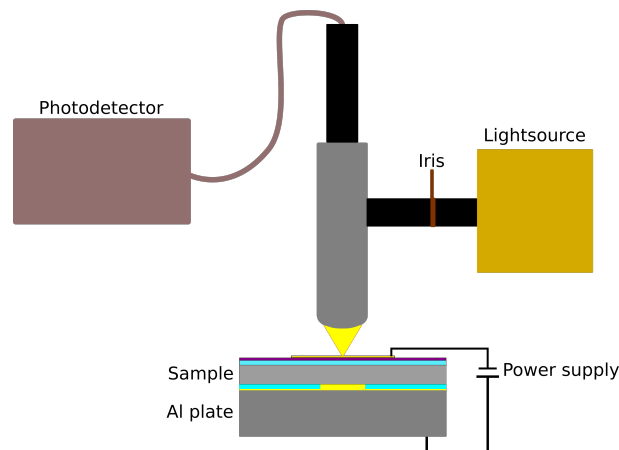


Figure 6.6: (a) Schematic of the measurement setup for reflection spectroscopy.

Signal spectra were obtained for areas with and without MoS_2 . A reference spectrum was measured using a mirror and a background spectrum was measured with the internal shutter of the spectrometer closed. The reflectance was calculated as

$$R = \frac{\text{signal} - \text{background}}{\text{reference} - \text{background}} \quad (6.1)$$

The reflectance of the sample on spots with and without MoS_2 is shown in figure 6.7(a). For further analysis the reflectance data was smoothed with a moving average filter, showing fairly clearly two valleys in reflectance near 1.9 and 2.0 eV as seen in Fig. 6.7(b) which correspond to the absorption of the A and B exciton of MoS_2 [41, 48].

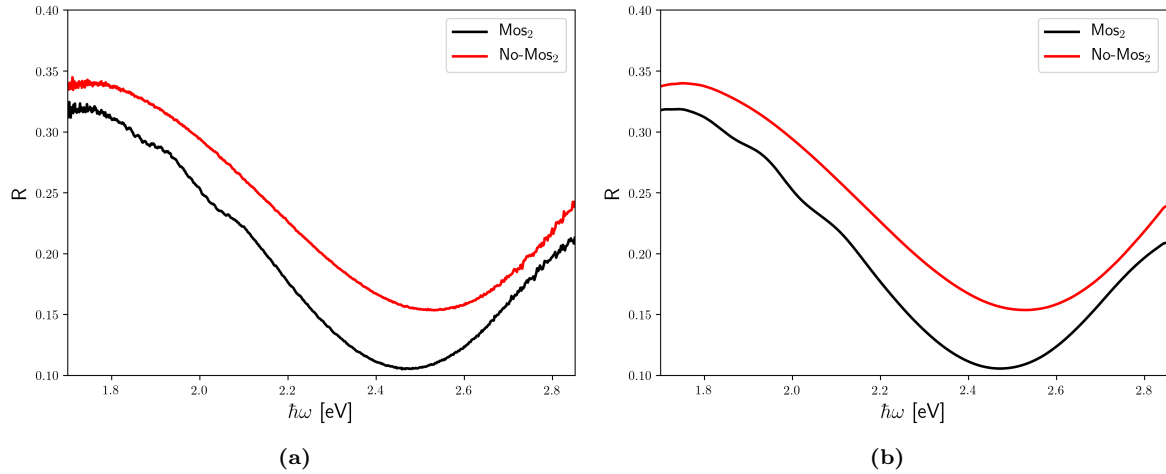


Figure 6.7: (a) Reflectance of the sample on spots with and without MoS_2 , showing some noise from the experiment. (b) Smoothed reflectance of the sample on spots with and without MoS_2 . Two small valleys can be seen near 1.9 eV and 2.0 eV, respectively for the spot with MoS_2 .

However, it is difficult to find the minima of these valleys. Therefore, the derivative of the reflectance with respect to frequency was calculated, making it easier to find the minima position of the valleys, as shown in Fig. 6.8. Due to noise in the data the differentiated reflectance still contains a considerable amount of noise, leading to an uncertainty in the position of the minima. Therefore, the minimum in each valley was determined and the lower and upperbound of the minima position were set as the frequencies where the derivate of the reflectance differed 10% from the minimum value.

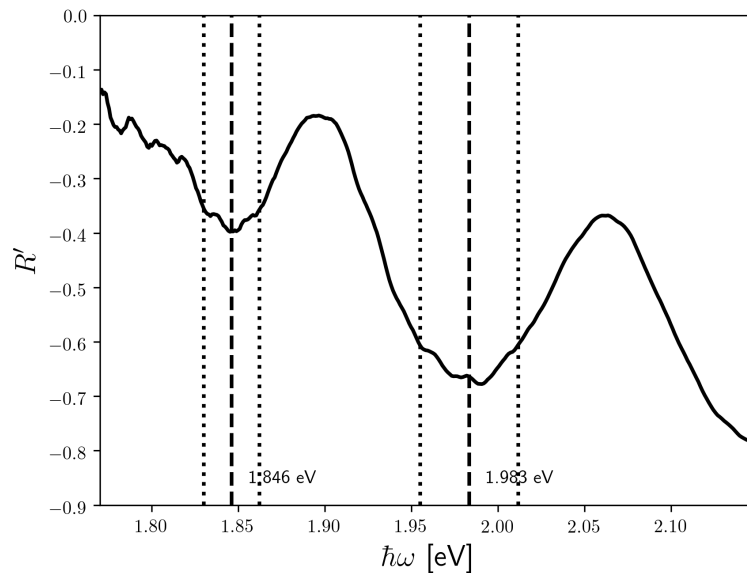


Figure 6.8: Derivative of the reflectance, showing the positions of the A and B excitons, indicated by vertical dashed lines. The dotted lines indicate the uncertainty of the exciton positions.

Then the exciton position was calculated as the average of the position of both dotted vertical lines, with the uncertainty being the distance to the lower/upper bound. Using this procedure the exciton position was found to be 1.846 ± 0.016 eV and 1.983 ± 0.28 eV, which is in excellent agreement with Splendiani et

al., who reports A1 and B1 exciton peaks at 1.85 eV and 1.98 eV, respectively [41]. As these valleys correspond to the A1 and B1 exciton of MoS₂, where the difference comes from spin-orbit splitting of the valence band. The spin-orbit splitting is 0.137±0.044 eV, which is in fair agreement with [17], whom report a splitting of 0.160 eV for MoS₂.

In order to compute the refractive index, a 4 medium transfer matrix model was used with air/MoS₂/SiO₂/Si as explained in App. C. The refractive index of MoS₂ was modeled using a sum of Lorentz oscillators, as done in [10],

$$\varepsilon = A + \sum_j \frac{F_j}{\omega^2 - \omega_j^2 - i\omega\Gamma_j}, \quad (6.2)$$

with $A, F_j, \omega_j, \Gamma_j$ being fitting parameters. The fit of the reflectance for 9 Lorentz oscillators is shown in Fig. 6.9(a). After fitting the transfer matrix model to the reflectance data, the refractive index shown in Fig. 6.9(b) was found.

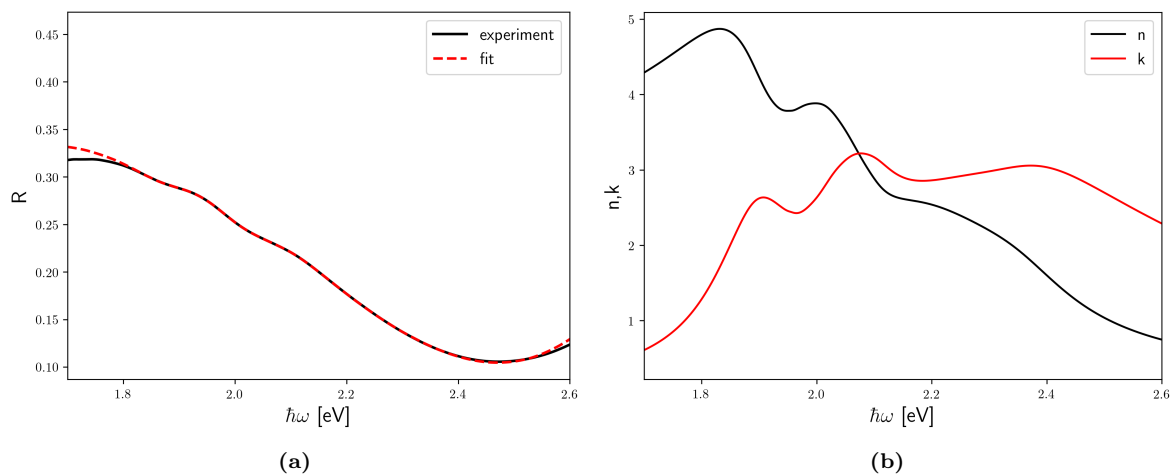


Figure 6.9: (a) Fit of the smoothed reflectance data, showing good agreement within 1.8 eV to 2.5 eV. (b) The refractive index of MoS₂ used in the transfer matrix model for the fit.

The real part of the refractive index shows fairly good agreement with [49] around 1.8 eV and 2.0 eV, however, the transfer matrix model used in this thesis was limited to a fairly small frequency range and does not agree well beyond 2.0 eV.

Reflectance was also measured, while the MoS₂ was gated via the gold plate capacitors. The measured reflectances with gating show no difference compared to the above measurements except for a constant reflectance shift over the entire spectrum. Yu et al. finds that the reflectance changes by 0.005 at the position of the A-exciton when applying -50 V compared to 0 V, which is a very small change. Applying the same analysis of the derivative as above no changes in the exciton positions were found. The reflectance spectrum at 0V, 60V and -60V across the capacitor is shown in Fig. 6.10.

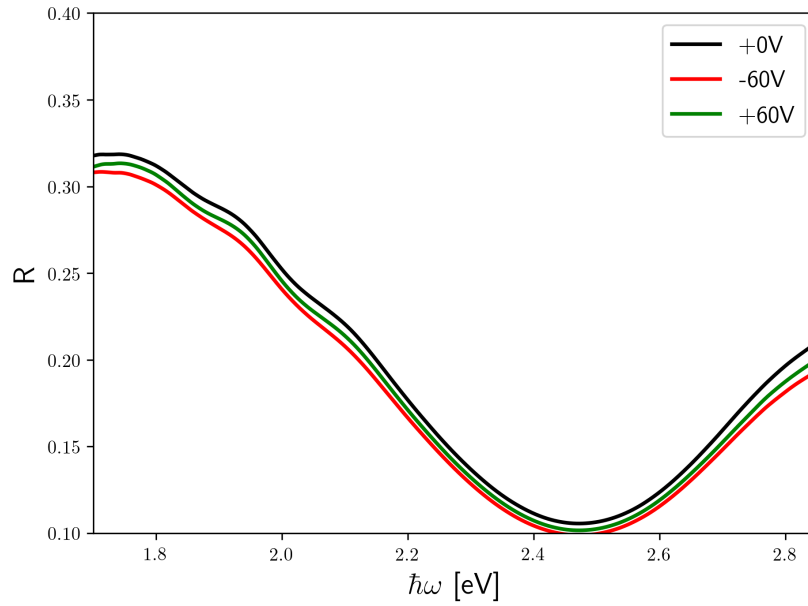


Figure 6.10: Reflectance from the MoS₂ sample, while the sample was gated with -60V, 0V, and 60V. No conclusive difference can be seen from the reflectance data.

During the fabrication process the MoS₂ layer underneath some of the gold contacts was damaged which would cause the gating to be ineffective for these contacts. It is expected that the measurements in Fig. 6.10 were performed on one of these, and that more measurements in another region would hopefully show the expected tunability of the optical properties.

Chapter 7

Conclusion

The introduction pointed out the goals of this thesis, the first one of which was to develop tools to calculate the optical properties of monolayer materials in the independent particle picture. The theory has been reviewed and code has been written that uses DFT wave functions from GPAW. As expected the agreement with experiment is rather poor for MoS₂, as electron-hole interactions are not taken into account. This has however served as an introduction to the calculation of optical properties and the use of GPAW, aiding the development of more accurate models. The main motivation for this work was the observation of tunable optical properties related to doping of TMDs, in order to include doping in DFT calculations two models have been proposed and compared, with the jellium background model found to be more controllable and easier to use. It has been found that high doping concentrations in the jellium model shift the conduction bands down, moving optical transitions to lower energies. However, the prominent effect of doping in the independent particle framework is Fermi blocking of the lowest states in the conduction band and the appearance of transitions between conduction bands. Thus such a calculation does not at all reveal the expected tunability.

It is evident that the independent particle framework cannot correctly explain the optical properties of MoS₂, thus a more sophisticated theory that includes the important electron-hole interaction has been presented. The screened electron-hole interaction is included through an analytical expression for the screening in a 2D material which along with the slow-rapid approximation allows for efficient calculations of the optical properties of intrinsic MoS₂. The slow-rapid approximation discards the exchange interaction and part of the Coulomb interaction, the viability of this approximation has been investigated showing a 10% deviation. In order to adapt this framework to handle doping an additional analytical term was added to the screening and the effect of doping on quasiparticle energies was investigated. It was found that doping both renormalizes the fundamental band gap and dramatically decreases the effective electron mass near the \mathbf{K} special point. The effect of doping on the optical properties is to decrease the exciton binding energy and decrease the optical conductivity showing good agreement with the tunability found in experiments. The main qualitative disagreement with experimental results is the position of the excitonic transition not being constant. An improvement of the screening model was attempted by combining the analytical model with a plasmon-pole model, however this does not improve the results.

The reflectance of intrinsic MoS₂ have been measured through reflectance spectroscopy and Kramers-Kronig analysis in combination with a transfer matrix model has been used to obtain the optical properties, from which it was possible to identify the position of the excitonic transitions. A MoS₂ sample was prepared that could be electrically gated, however the measurements did not show the tunability of the optical properties. Although it is expected that additional measurements would show the predicted behaviour.

Appendix A

Computational Details for Ab-initio Calculations

The parameters used for the majority of the results of the ab-initio calculations are presented here.

For all calculations, convergence criteria of the self-consistent DFT cycle were set to the default GPAW ones, which at the time of the calculations were:

- Energy difference per valence electron for three last iteration below 0.5 meV.
- Change in integrated absolute density below 0.0001 electron per valence electrons.
- Integrated residuals of KS equations below $4 \cdot 10^{-8}$ eV² per valence electron.

For the calculations in Chap. 2, corresponding to datasets MoS₂-1 and C₂-1 in table A.1, the lattice constants were found by BFGS optimization until the forces were below $5 \cdot 10^{-3}$ eV/Å. In all DFT calculations occupation numbers were set according to the Fermi distribution with a thermal energy of 0.025 eV. Convergence was checked for datasets MoS₂-1 and C₂-1 in relation to number of k-points, energy cutoff and vacuum. All DFT calculations were performed using the Perdew-Wang LDA functional [50]. The remaining parameters can be found in table A.1. The headers in the table refer to the following

- Dataset: Self-explanatory.
- Setup: The PAW setup used for the calculation. The numbers refer to the amount of valence electrons for that atom
- Lattice constants: In-plane lattice constant and distance between sulfur atoms for MoS₂.
- Cutoff: Energy cutoff for plane waves in DFT basis.
- Vacuum: The height of the supercell
- SCF k: k-grid used for self-consistent calculation, always Monkhorst-Pack grids.
- NSCF k: k-grid used for non self-consistent calculation. M and T refer to Monkhorst-Pack and triangular grids respectively.
- Bands: Number of conduction bands

Dataset	Setup	Lattice constants	Cutoff	Vacuum	SCF k	NSCF k	Bands
MoS ₂ -1	Mo:14, S:6	3.11 Å, 3.10 Å	800 eV	15 Å	M:12x12x1	T:55x55x1	+12
C ₂ -1	C:4	2.44 Å	800 eV	15 Å	M:12x12x1	T:55x55x1	+12
MoS ₂ -2	Mo:14, S:6	3.18 Å, 3.13 Å	750 eV	20 Å	M:20x20x1	M:50x50x1	+4
MoS ₂ -GW	Mo:14, S:6	3.18 Å, 3.13 Å	750 eV	20 Å	M:36x36x1	NA	NA

Table A.1: Settings and parameters used for DFT calculations.

Lattice constants for datasets MoS₂-2/MoS₂-GW are taken from [38]. G0W0 calculations were performed based on the SCF calculation of the MoS₂-GW dataset, using a truncated Coulomb interaction with 200 bands used for construction of relevant quantities and a plane wave cutoff of 50 eV, which [51] notes converges the calculation. For BSE calculations, where QP energies are taken from G0W0 and not scissor-shifted DFT, QP energies are retrieved from MoS₂-GW and wave function information from MoS₂-2. Table A.2 shows which figures are made with each dataset.

Dataset	Figures
MoS ₂ -1	2.4, 2.5, 3.13, 3.14
C ₂ -1	2.1, 2.2, 2.3, 3.8, 3.9, 3.10, 3.11, 3.12
MoS ₂ -2	4.1, 4.6, 4.8, 4.9, 4.10, 4.11, 4.12, 4.13, 5.3, 5.7, 5.8, 5.9, 5.10, 5.11, 5.12, 5.13
MoS ₂ -GW	4.1, 4.13, 5.3, 5.4, 5.5, 5.6, 5.8, 5.9, 5.10, 5.11, 5.12, 5.13

Table A.2: Dataset to figure relations.

Appendix B

Projector Augmented Wave method

One of the numerical problems with calculating the electronic structure of matter, is the high kinetic energy of the electrons in the atomic region, near the atom cores, which results in rapid oscillations of the true wave function near the atom cores that are difficult to handle numerically. One way to solve this problem is to create some region around the atom cores, where the coulomb potential is replaced with a so-called pseudo potential that retains some property of the wave function in the atomic region, but creates a smooth wave function as well. However, when using pseudo potentials the information of the true wave function is lost in the atomic region. [52]

Another method is the projector augmented wave (PAW) method. Here, a single particle pseudo wave function $|\tilde{\Psi}\rangle$ is created that is related to the single particle true wave function $|\Psi\rangle$ (e.g. KS orbital) through a linear transformation

$$\mathcal{T} = 1 + \sum_R \mathcal{T}_R, \quad (\text{B.1})$$

where the \mathcal{T}_R is a local term, which only acts close to the R atom, in the so-called augmentation sphere region. This also means that outside the augmentation spheres the true wave function is identical to the pseudo wave function. Within each augmentation sphere Ω_R the wave functions are split up in a basis of partial waves, so that the pseudo wave function is

$$|\tilde{\Psi}\rangle = \sum_i c_i |\tilde{\phi}_i\rangle, \in \Omega_R, \quad (\text{B.2})$$

with $\tilde{\phi}_i$ being the i 'th pseudo partial wave of that augmentation region, c_i being the expansion coefficients, and the true wave function is

$$|\Psi\rangle = \mathcal{T} |\tilde{\Psi}\rangle = \sum_i c_i |\phi_i\rangle, \in \Omega_R, \quad (\text{B.3})$$

with ϕ_i being the i 'th true partial wave of that augmentation region. As $|\phi_i\rangle = \mathcal{T} |\tilde{\phi}_i\rangle$, the coefficients are the same.

As the true wave function is identical to the pseudo wave function except within the augmentation sphere, the true wave function can be found by subtracting the pseudo partial waves from the pseudo wave function and adding the true partial waves as

$$|\Psi\rangle = |\tilde{\Psi}\rangle - \sum_i c_i |\tilde{\phi}_i\rangle + \sum_i c_i |\phi_i\rangle, \in \Omega_R. \quad (\text{B.4})$$

In order to make sure the partial waves only act within their augmentation region they must be identical outside the augmentation region. [52] Since the transformation operator is linear the coefficients must be linear functionals of the pseudo wave function, and can be found as

$$c_i = \langle \tilde{p}_i | \tilde{\Psi} \rangle, \in \Omega_R, \quad (\text{B.5})$$

where $|\tilde{p}_i\rangle$ is some fixed function, called the projector function. By the definition of the pseudo wave function the projector function has to obey

$$\langle \tilde{\phi}_i | \tilde{p}_j \rangle = \delta_{ij}, \in \Omega_R, \quad (\text{B.6})$$

so that the pseudo wave function is still determined by

$$|\tilde{\Psi}\rangle = \sum_i c_i |\tilde{\phi}_i\rangle = \sum_i |\tilde{\phi}_i\rangle \langle \tilde{p}_i | \tilde{\Psi} \rangle, \in \Omega_R. \quad (\text{B.7})$$

Thus, the true wave function is found by

$$|\Psi\rangle = |\tilde{\Psi}\rangle + \sum_i \left(|\phi_i\rangle - |\tilde{\phi}_i\rangle \right) \langle \tilde{p}_i | \tilde{\Psi} \rangle, \in \Omega_R. \quad (\text{B.8})$$

The benefit of this method is that instead of calculating the true wave function, with its highly oscillating part near the atom cores, one can instead calculate the smooth pseudo wave function and determine the partial waves of each atom core and the projector functions. The true partial waves could be the radial solutions of the Schrödinger equation for an isolated atom, making the partial waves orthogonal to the core states, and for each true partial wave there is a pseudo partial wave and a projector function. [53]

Using the PAW method one needs to consider that it is not the true wave function that is being calculated and so all expectation values derived from the pseudo wave function need to be corrected in order to obtain the true expectation values. The true expectation value for some operator A is

$$\langle A \rangle = \sum_n f_n \langle \Psi_n | A | \Psi_n \rangle, \quad (\text{B.9})$$

with f_n being the occupation of the n 'th band. However, it can also be found through the pseudo wave function as

$$\langle A \rangle = \sum_n f_n \langle \tilde{\Psi}_n | \tilde{A} | \tilde{\Psi}_n \rangle, \quad (\text{B.10})$$

where the new operator $\tilde{A} = \mathcal{T}^\dagger A \mathcal{T}$. It can be shown by expanding the transformation operators and neglect terms related to non-local operators the expectation value becomes [52]

$$\langle A \rangle = \sum_n f_n \langle \tilde{\Psi}_n | A | \tilde{\Psi}_n \rangle + \sum_{a,ij,n} f_n \langle \tilde{\Psi}_n | \tilde{p}_i^a \rangle^* \langle \tilde{\Psi}_n | \tilde{p}_j^a \rangle \left[\langle \phi_i^a | A | \phi_j^a \rangle - \langle \tilde{\phi}_i^a | A | \tilde{\phi}_j^a \rangle \right]. \quad (\text{B.11})$$

Appendix C

Transfer Matrix Method & Constrained Kramers Kronig Analysis

Experimentally, the reflectance of the MoS₂ device described in Chap. 6 is measured. In order to obtain the dielectric function from this measurement a relation between the reflectance and the dielectric function is required, which can be obtained through the transfer matrix method.

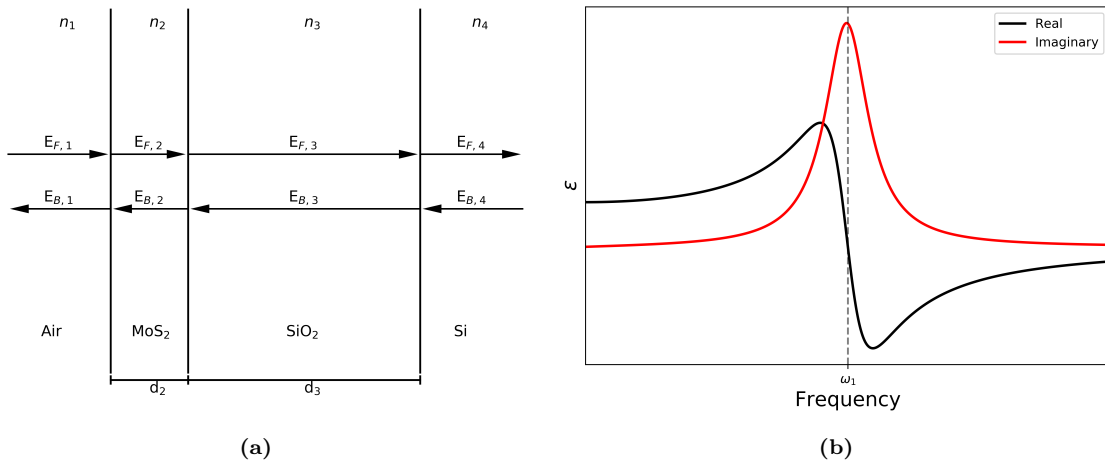


Figure C.1: (a) Four medium stack, corresponding to the case of MoS₂ on SiO₂ over Si in air. (b) Single Lorentzian oscillator with center position ω_1 .

In the transfer matrix method the total field is described by forward (E_F) and backward (E_B) propagating waves, which at any position in the system of interest are the sum of all waves propagating in that direction. For an arbitrary multilayer structure the forward and backward propagating waves on either side of the multilayer structure can be related through the system matrix \mathbf{M}

$$\begin{bmatrix} E_{F,1} \\ E_{B,1} \end{bmatrix} = \mathbf{M} \begin{bmatrix} E_{F,N} \\ E_{B,N} \end{bmatrix}, \quad (\text{C.1})$$

where the superscripts denotes the medium. An illustration for a four layer stack is shown in Fig. C.1(a) [54]. The system matrix can be found through multiplication of transmission matrices and propagation matrices, that describe reflection/transmission at interfaces and propagation through a bulk region respectively.

Light propagating through an interface will be partly reflected and partly transmitted, which in linear, isotropic, homogeneous media can be described by the Fresnel reflection and transmission coefficients, which when assuming normal incidence and TE-polarization are

$$r_{ij} = \frac{n_i - n_j}{n_i + n_j}, \quad (\text{C.2})$$

$$t_{ij} = \frac{2n_i}{n_i + n_j}, \quad (\text{C.3})$$

where n_i denotes the refractive index on the reflection side, and n_j is the refractive index of the transmission side [55]. In terms of the Fresnel coefficients the transmission matrix from medium i to medium j is

$$T_{ij} = \frac{1}{t_{ij}} \begin{bmatrix} 1 & r_{ij} \\ r_{ij} & 1 \end{bmatrix}. \quad (\text{C.4})$$

The matrix on the right-hand side is the transmission matrix of the interface between materials i and j . After light has propagated a length d through a medium the phase will have advanced by e^{-ikd} where k is the component of the wave-vector in direction of propagation, thus a propagation matrix can be defined that relates the fields just after an interface to the fields just before the next interface

$$P_i = \begin{bmatrix} e^{i\delta_i} & 0 \\ 0 & e^{-i\delta_i} \end{bmatrix}, \quad (\text{C.5})$$

where $\delta_i = k_0 n_i d_i$ and k_0 is the wave vector in vacuum. The system matrix can be calculated by multiplication of transmission and propagation matrices. [54]

$$\mathbf{M} = \mathbf{T}_{12}\mathbf{P}_2\mathbf{T}_{23}\mathbf{P}_3\cdots\mathbf{T}_{N-1,N}. \quad (\text{C.6})$$

Looking at the case where light only enters the system from one side, it is clear that the total reflection coefficient is

$$r = \frac{M_{21}}{M_{11}}, \quad (\text{C.7})$$

which can be converted to reflectance by taking the absolute square

$$R = |r|^2. \quad (\text{C.8})$$

For a 4 medium system consisting of air, MoS₂, SiO₂ and Si, as depicted in Fig. C.1(a), the reflectance can be found as

$$R = \frac{\left| \frac{1}{t_{12}t_{23}t_{34}} (r_{34} (r_{12}r_{23}e^{2id_2} + 1) + (r_{12}e^{2id_2} + r_{23}) e^{2id_3}) \right|^2}{\left| \frac{1}{t_{12}t_{23}t_{34}} (r_{34} (r_{12} + r_{23}e^{2id_2}) + (r_{12}r_{23} + e^{2id_2}) e^{2id_3}) \right|^2}. \quad (\text{C.9})$$

The same expression could have been found if TM polarization had been assumed, as the two are equivalent under normal incidence. The refractive index of air is set to 1, while the frequency dependent refractive indices for SiO₂ and Si are obtained from [56, 57]. The dielectric function of the MoS₂ layer is modelled by a sum of Lorentz oscillators

$$\varepsilon(w) = A + \sum_i \frac{f_i}{w_i^2 - w^2 - w\Gamma_i}, \quad (\text{C.10})$$

where A describes a bulk term and f_i , w_i , Γ_i is the strength, position and dampening of the i 'th oscillator, respectively, which is a common approach for this kind of analysis [10, 42]. This model is known as constrained Kramers-Kronig analysis. A benefit of this model is that each individual oscillator obeys the Kramers-Kronig relation between the real and imaginary part of the dielectric permittivity inherently.

Fig. C.1(b) shows a single oscillator [58]. One problem is that the Kramers-Kronig relations relate the entire real part of the spectrum to the entire imaginary part, which in principle means that oscillators outside the measured frequencies influence dielectric permittivity in the region of interest [42]. Using Eq. (C.10) the reflection obtained from (C.9) can be fitted to experimental measurements, where the fitting parameters are oscillator strengths, positions, and dampenings.

Appendix D

Implementation

While some of the numerical details have been covered in the main text, a brief description of the general implementation is in order. All calculations are based on the GPAW DFT code, which outputs '.gpw' files for all results. These files are generally quite large due to the large amount of plane wave coefficients and k-points, e.g. 6 GB for the 55x55 grids used for independent particle calculations. All code was developed in Python for easy implementation with GPAW. Native Python is quite slow and not very appropriate for numerical calculations, however with the Numpy library, which implements MATLAB-like array operations fairly fast code can be developed, if for-loops are replaced by vectorized operations. Python implements so-called object oriented programming that allows for creating classes that are data structures with built-in methods, which has been utilized extensively. Any object can be "pickled", which converts it to a byte-stream, including data and methods.

For the independent particle calculations the starting point is a GPAW calculation resulting in one of the above mentioned gpw files. In order to enable revisions and additions to the code the scheme shown in Fig. D.1 was used, with each step representing an instance of a Python class object. The idea is that the large GPW file can be converted to a much smaller 'pickle' file where plane-wave coefficients have been converted to momentum matrix elements. This makes the files much easier to work with and ensures that momentum matrix elements are only calculated once per DFT calculation. The pickled object can then be read by the main code, where the remaining calculations are performed, i.e calculating the DOS, Brillouin zone integrations, and so on. This object can then be saved and passed to other code for plotting and other analysis. In addition to the advantages presented thus far, this scheme has the advantage that the main code works for all types of initial data as long as it can be pickled correctly. This means that no changes need to be made to the main code if for example pseudo potentials are used instead of PAW which changes the calculation of momentum matrix elements, which is done in the pickler. Similarly ABINIT calculations can be used instead of GPAW with only changing the pickler-part of the code, or tight-binding based eigenvalues/momentum matrix elements can be used instead of DFT.

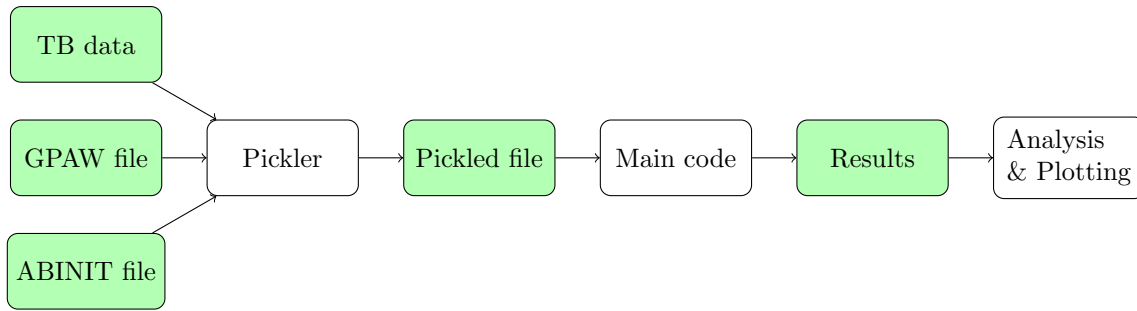


Figure D.1: Flowchart representing the structure of the code for independent particle calculations. The green boxes are files, while the white are code.

For the Bethe-Salpeter code a similar strategy was used, with a few differences due to the complications introduced by the BSE framework. As momentum matrix elements are no longer the only required piece of wave function information, and interpolation is done to arbitrary k-point grids, all the coefficients for the included bands are required. However, the BSE code is much more susceptible to memory-related problems due to the large size required of the BSE matrix and it is still beneficial to not include unnecessary data from the gpw-file. Furthermore the BSE calculation requires data, not only from a DFT calculation, but also a G0W0 calculation meaning multiple files are required. Thus creating a pickled intermediate file is nice for ensuring the correct data is passed along the code. The scheme for the BSE code is shown in Fig. D.2. First the set of G-vectors that are present for all \mathbf{k} points in the DFT calculation are found for the specific k-point grid and energy cutoff and lattice constants of the DFT calculation are found. This information is saved, as it takes a significant amount of time to calculate and does not change if e.g. the doping is changed. After this the coefficients of these G-vectors are compared among all k-points to find one that has a large coefficient for all k-points so that the interpolation scheme works properly. This information is passed onto a pickler that extracts the coefficients and DFT eigenvalues along with QP energies from an appropriate G0W0 output file. The pickler also triangulates the DFT k-point grid and calculates the barycentric linear interpolation functions. The pickled file/object can then be passed onto the main BSE code that interpolates to a k-point grid of arbitrary size, within the rectangular Brillouin zone and sets up the BSE matrix. As the BSE matrix is hermitian only the upper diagonal is calculated and all operations for creation of the Hamiltonian are vectorized over rows within Numpy, which greatly speeds up this part of the calculation and is a practical way of parallelizing the calculation over CPU cores. For diagonalization an algorithm that overwrites the input matrix with eigenvectors was used to save memory. This structure offers some of the versatility that the independent particle-code has, i.e. it is relatively simple to change from GPAW to ABINIT but as the main code heavily depends on a plane-wave basis, changing the basis of the DFT calculation is not possible without major changes.

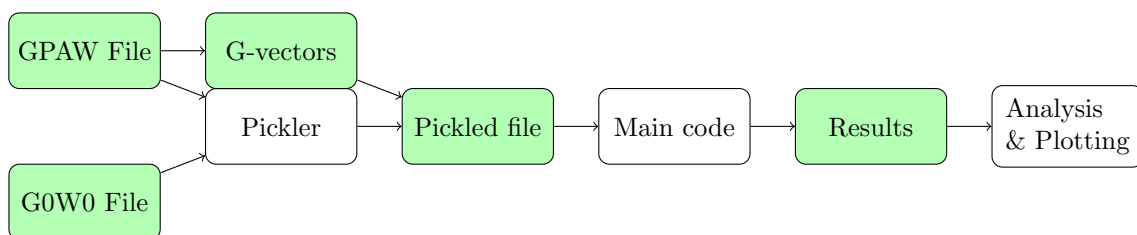


Figure D.2: Flowchart representing the structure of the code for Bethe-Salpeter calculations. The green boxes are files, while the white are code.

Bibliography

- [1] K. S. Novoselov, A. K. Geim, S. V. Morozov, D. Jiang, Y. Zhang, S. V. Dubonos, I. V. Grigorieva, and Firsov A. A. Electric Field Effect in Atomically Thin Carbon Films. *Science*, 306:666–669, 2004.
- [2] K. S. Novoselov, D. Jiang, F. Schedin, T. J. Booth, V. V. Khotketvich, S. V. Morozov, and A. K. Geim. Two-dimensional atomic crystals. *PNAS*, 102:10451–10453, 2005.
- [3] Y. Qiao, Y. Wei, Y. Pang, Y. Li, D. Wang, Y. Li, N. Deng, X. Wang, H. Zhang, Q. Wang, Z. Yang, L. Tao, H. Tian, Y. Yang, and T. Ren. Graphene devices based on laser scribing technology. *Jpn. J. Appl. Phys.*, 57.4S:04FA01, 2018.
- [4] Y. Cao, V. Fatemi, A. Demir, S. Fang, S. L. Tomarken, J. Y. Luo, Sanchez-Yamagashi. J. D., K. Watanabe, T. Tanuguchi, E. Kaxiras, R. C. Ashoori, and P. Jarillo-Herrero. Correlated insulator behaviour at half-filling in magic-angle graphene superlattices. *Nature*, 556.7699:80, 2018.
- [5] F. Schwierz. Graphene transistors. *Nat. Nanotechnol.*, 5:487–496, 2010.
- [6] Jorge Kohanoff. *Electronic Structure Calculations for Solids and Molecules: Theory and Computational Methods*. Cambridge University Press, 2006.
- [7] B. Radisavljevic, A. Radeonovic, J. Brivio, V. Gioacometti, and A. Kis. Single-layer MoS₂ transistors. *Nat. Nanotechnol.*, 6:147–150, 2011.
- [8] P. Dhakras, Agnihotri. P., and Lee J U. Three fundamental devices in one: a reconfigurable multi-functional device in two-dimensional WSe₂. *Nanotechnology*, 28:1–7, 2017.
- [9] Sutar. S., P. Agnihotri, E. Comfort, T. Taniguchi, K. Watanabe, and Lee J. U. Reconfigurable p-n junction diodes and the photovoltaic effect in exfoliated MoS₂ films. *App. Phys. Lett.*, 104:1–5, 2014.
- [10] Y. Yu, Y. Yu, L. Huang, H. Peng, L. Xiong, and Cao L. Giant Gating Tunability of Optical Refractive Index in Transition Metal Dichalcogenide Monolayers. *Nano Lett.*, 6:3613–3618, 2017.
- [11] G. Scuri, Y. Zhou, A. A. High, D. S. Wild, C. Shu, K. De Greve, L. A. Jauregui, T. Taniguchi, K. Watanabe, P. Kim, M. D. Lukin, and Park H. Large Excitonic Reflectivity of Monolayer MoSe₂ Encapsulated in Hexagonal Boron Nitride. *Phys. Rev. Lett.*, 120:037402–1–037402–6, 2018.
- [12] P. Back, S. Zeytinoglu, A. Ijaz, M. Kroner, and A. Imamoğlu. Realization of an Electrically Tunable Narrow-Bandwidth Atomically Thin Mirror Using Monolayer MoSe₂. *Phys. Rev. Lett.*, 120:037401–1–037401–5, 2018.
- [13] M. Palummo, G. Onida, and R. Del Sole. Ab initio optical properties of Si(100). *Phys. Rev. B*, 60:2522–2527, 1999.
- [14] R. M. Martin. *Electronic Structure Basic Theory and Practical Methods*. Cambridge University Press, 2004.

-
- [15] G. Onida, L. Reining, and A. Rubio. Electronic excitations: density-functional versus many-body Green's-function approaches. *Rev. Mod. Phys.*, 74:601–659, 2002.
- [16] M. A. Green. Improved value for the silicon free exciton binding energy. *AIP Adv.*, 3(112104):1–15, 2013.
- [17] A. R. Klots, A. K. M Newaz, B. Wang, D. Prasai, H. Kryzhanowska, J. Lin, D. Caudel, N. J. Ghimire, J. Yan, B. L. Ivanov, K. A. Velizhanin, A. Burger, D. G. Mandrus, N. H. Talk, S. T. Pantelides, and K. T. Bolotin. Probing excitonic states in suspended two-dimensional semiconductors by photocurrent spectroscopy. *Sci. Rep.*, 4:1–7, 2014.
- [18] J. J. Mortensen, L. B. Hansen, and K. W. Jacobsen. Real-space grid implementation of the projector augmented wave method. *Phys. Rev. B*, 71:035109, 2005.
- [19] J. Enkovaara, C. Rostgaard, J. J. Mortensen, J. Chen, M. Dulak, L. Ferrighi, J. Gavnholt, C. Glinsvad, V. Haikola, and H. A. Hansen. Electronic structure calculations with GPAW: a real-space implementation of the projector augmented-wave method. *J. Phys. Condens. Matter*, 22:253202, 2010.
- [20] M.V. Klein and T.E. Furtak. *Optics*. John Wiley and sons, 1986.
- [21] L. Novotny and B. Hecht. *Principles of Nano-Optics*. Cambridge University Press, 2013.
- [22] T. G. Pedersen. *Electric, Optical & Magnetic Properties of Nanostructures*. 2017.
- [23] Jenő Sólyom. *Fundamentals of the Physics Solids*, volume 2. Springer, 2009.
- [24] T. G. Pedersen. Analytic calculation of the optical properties of graphite. *Phys. Rev. B*, 67:1–4, 2003.
- [25] T. G. Pedersen, C. Flindt, J. Pedersen, A.P. Jauho, N. A. Mortensen, and Pedersen K. Optical properties of graphene antidot lattices. *Physical Review B*, 77(245431):1–6, 2008.
- [26] K. Nomura and A.H. MacDonald. Quantum Transport of Massless Dirac Fermions. *Phys. Rev. Lett.*, 98:076602, 2007.
- [27] D. A. Neamen. *Semiconductor physics and devices*. McGraw-Hill, 2012.
- [28] J. Suh, T. Park, D. Lin, D. Fu, J. Park, H. J. Jung, Y. Chen, C. Ko, C. Jang, Y. Sun, R. Sinclair, J. Chang, S. Tongay, and J. Wu. Doping against the Native Propensity of MoS₂: Degenerate hole doping by cation substitution. *Nano Lett.*, 14.12:6976–6982, 2014.
- [29] Q. Yue, S. Chang, S. Qin, and J. Li. Functionalization of monolayer MoS₂ by substitutional doping: a first-principles study. *Phys. Lett. A*, 377.19-20:1362–1367, 2013.
- [30] A. Ramasubramaniam and D. Naveh. Mn-doped monolayer MoS₂: an atomically thin dilute magnetic semiconductor. *Phys. Rev. B*, 87.19:195201, 2013.
- [31] P. Rastogi, S. Kumar, S. Bhowmick, A. Agarwal, and Y. S. Chauhan. Doping strategies for monolayer MoS₂ via surface absorption: A systematic study. *J. Phys. Chem. C*, 118:30309–30314, 2014.
- [32] H. Fang, M. Tosun, G. Seol, T. C. Chang, K. Takei, J. Gou, and A. Javey. Degenerate n-Doping of Few-layer Transition Metal dichalcogenides by potassium. *Nano Lett.*, 13:1991–1995, 2013.
- [33] R. F. W. Bader. *Atoms in Molecules: A Quantum Theory*. Oxford University Press, 1994.

- [34] G. Henkelman, A. Arnaldsson, and H. Jónsson. A fast and robust algorithm for Bader decomposition of charge density. *Comput. Mater. Sci.*, 36:354–360, 2006.
- [35] C. Hwang, D. A. Siegel, S. Mo, W. Regan, A. Ismach, Y. Zhang, A. Zetl, and A. Lanzara. Fermi velocity engineering in graphene by substrate modification. *Sci. Rep.*, 509:1–4, 2012.
- [36] J. P. Dahl. *Introduction to the Quantum World of Atoms and Molecules*. World Scientific, 2009.
- [37] F. Hüser, T. Olsen, and K. S. Thygesen. Quasiparticle GW calculations for solids, molecules, and two-dimensional materials. *Phys. Rev. B*, 87:23:235132, 2013.
- [38] F. A. Rasmussen and K. S. Thygesen. Computational 2D Materials Database: Electronic Structure of Transition-Metal Dichalcogenides and Oxides. *J. Phys. Chem. C*, 119:23:13169–13183, 2015.
- [39] R. Del Sole and R. Girlanda. Optical properties of semiconductors within the independent-quasiparticle approximation. *Phys. Rev. B*, 48:11789–11795, 1993.
- [40] H. Komsa and A. V. Krasheninnikov. Effects of confinement and environment on the electronic structure and exciton binding energy of mos2 from first principles. *Phys. Rev. B*, 86:241201, 2012.
- [41] A. Splendiani, L. Sun, Y. Zhang, T. Li, J. Kim, C.Y. Chim, and F. Wang Galli. Emerging Photoluminescence in Monolayer MoS₂. *Nano Lett.*, 10:1271–1275, 2010.
- [42] H. Li, A. Chernikov, X. Zhang, A. Rigosi, H. M. Hill, A. M. van der Zande, D. A. Chenet, E. Shih, J. Hone, and T. F. Heinz. Measurement of the optical dielectric function of monolayer transition-metal dichalcogenides: MoS₂, MoSe₂, WS₂, and WSe₂. *Phys. Rev. B*, 90:205422, 2014.
- [43] H. Haug and S. W. Koch. *Quantum Theory of the Optical and Electronic Properties of Semiconductors*. World Scientific, 2004.
- [44] S. Gao, Y. Liang, C. D. Spataru, and L. Yang. Dynamical Excitonic Effects in Doped Two-Dimensional Semiconductors. *Nano Lett.*, 16:5568–5573, 2016.
- [45] C. Robert, M. A. Semina, Cadiz. F., M. Manca, E. Courtade, T. Taniguchi, K. Watanabe, H. Cai, B. Tongay, S. and Lassagne, P. Renucci, T. Amand, X. Marie, M. M. Glazov, and B. Urbaszek. Optical spectroscopy of excited exciton states in MoS₂ monolayers in van der Waals heterostructures. *Phys. Rev. Mat.*, 2:1:011001, 2018.
- [46] M. M. Bennameaur, B. Radisavljevic, Héron J. S., S. Sahoo, and H. Berger. Visibility of dichalcogenide nanolayers. *Nanotechnology*, 22:12:125706, 2011.
- [47] H. Li, Q. Zhang, C. C. R. Yap, B. K. Tay, T. H. T. Edwin, A. Olivier, and D. Baillargeat. From bulk to monolayer MoS₂: evolution of raman scattering. *Adv. Funct. Mater.*, 22:7:1385–1390, 2012.
- [48] D. Xiao, G. Liu, W. Feng, X. Xu, and W. Yao. Coupled Spin and Valley Physics in Monolayers of MoS₂ and Other Group-VI Dichalcogenides. *Phys. Rev. Lett.*, 108:196802, 2012.
- [49] H. Zhang, Y. Ma, Y. Wan, X. Rong, Z. Xie, W. Wang, and Dai L. Measuring the Refractive Index of Highly Crystalline Monolayer MoS₂ with High Confidence. *Sci. Rep.*, 5:8440, 2015.
- [50] J. P. Perdew and Y. Wang. Accurate and simple analytic representation of the electron-gas correlation-energy. *Phys. Rev. B*, 45:13244–13249, 1992.
- [51] F. Hüser, T. Olsen, and K. S. Thygesen. How dielectric screening in two-dimensional crystals affects the convergence of excited-state calculations: Monolayer MoS₂. *Phys. Rev. B*, 88:24:245309, 2013.

- [52] P. E. Blochl, C. J. Forst, and J. Schimpl. Projector augmented wave method: ab initio molecular dynamics with full wave functions. *Bull. Mater. Sci.*, 26:33–41, 2003.
- [53] P. E. Blochl. Projector augmented-wave method. *Phys. Rev. B*, 50:17953–17979, 1994.
- [54] C. C. Katsidis and D. I. Siapkas. General transfer-matrix method for optical multilayer systems with coherent, partially coherent, and incoherent interference. *Appl. Opt.*, 41:3978–3987, 2002.
- [55] E. Hecht. *Optics*. Pearson, 4 edition, 2014.
- [56] L. Gao, F. Lemarchand, and M. Lequime. Refractive index determination of SiO₂ layer in the UV/Vis/NIR range: spectrophotometric reverse engineering on single and bi-layer designs. *Journal of the European Optical Society - Rapid publications*, 8, 2013.
- [57] G. E. Jr. Jellison. Optical functions of silicon determined by two-channel polarization modulation ellipsometry. *Opt. Mat.*, 1:41–47, 1992.
- [58] A. B. Kuzmenko. Kramers–Kronig constrained variational analysis of optical spectra. *Rev. Sci. Instrum.*, 76:083108, 2005.